

Structure-Function Correlation and Biophysical Analysis of a Novel 3D *In Vitro* Leukaemia Model

Jenna Rebekah James, MPhys

School of Medicine

University of Nottingham

A thesis submitted for the degree of

Doctor of Philosophy

2020 J.R. James

Declaration

I, Jenna Rebekah James, confirm that the work presented in this thesis is my own. Where information has been derived from other sources, I confirm that this has been indicated in the thesis.



SIGNATURE

Acknowledgements

I cannot express enough thanks to my supervisors, Dr Alex Thompson, Dr Amanda Wright, Prof Cathy Merry, and Dr Kenton Arkill for their continued support and encouragement. I am truly grateful for the experiences and learning opportunities provided by them and the CDT of Regenerative Medicine.

I would like to thank my amazing colleagues and friends at the University of Nottingham. It has been a privilege to be welcomed into such amazing groups, and I want to thank you all for your patience and guidance, both academically and personally.

Finally, to my wonderful family and friends. Without their continued love, support, and gaming nights through-out my PhD, I would not have made it here today. I am truly grateful for the many conversations and for knocking common sense into me when I needed it! Matt, Nick, and Becca, thank you for always being there and for keeping me (somewhat) sane.

I would like to express a special thank you to my wonderful Mum and my partner, Adam. Mum, there is no way to thank you for everything you have done for me. Adam, you are my rock and my best friend, and I can't wait to see what our future holds. Thank you both for giving me laughter, and the strength to get here. You are both everything to me and I will forever be grateful for having you both in my life.

Abstract

The prognosis for relapsed acute myeloid leukaemia (AML) is poor, with available treatments unable to fully eradicate the leukaemic stem cells (LSCs) from which the heterogeneous AML cell types are considered to arise. LSCs evade treatment by hiding within the bone marrow niche, a property current 2D *in vitro* models fail to recapitulate. As the field of cancer research continues to acknowledge the disparate response of leukaemia cells to treatments *in vitro* as compared to *in vivo*, research requires defined and adjustable synthetic models in which to improve our understanding of the impact of mechanical cues in AML treatment response.

By use of a synthetic self-assembling peptide hydrogel (FEFEFKFK) of modifiable viscosity and composition, this project developed and utilised a 3D model of the bone marrow niche to screen repurposed FDA-approved drugs. The unmodified peptide gels contained no inherent matrix proteins or growth factors, and as such offered the unique ability to observe the influence of 3-dimensions on cell behaviour independent of binding motifs. Using novel biophysical techniques based on optical tweezers, the microrheological properties of the peptide gels were quantified, and subsequently demonstrated the stiffness of the model to be comparable with that of the bone marrow. The resulting 3D models showed significantly higher leukaemic cell proliferation than in 2D liquid culture or in higher stiffness gels. Finally, the models were used to mimic 'early-stage' and 'established' AML and treated with FDA-approved drugs. These results identified a variation of drug efficacy between the models and 2D liquid culture, suggesting the unmodified 3D environment influences AML cell sensitivity to drug treatment.

Pathophysiologically relevant *in vitro* cancer models for drug discovery and development is one of the major challenges facing researchers in the desire to improve the low translation of therapies into clinic. Here we present a novel 3D AML model offering unique insight into the impact of mechanical characteristics on cell behaviour, proliferation, and drug sensitivity. Future work following from these results will continue to obtain an improved mechanistic understanding of 3D models in AML drug repurposing and resistance, with the aim to develop the 3D peptide gel for patient-derived tissue.

List of contents

DECLARATION I

ACKNOWLEDGEMENTS II

ABSTRACT III

LIST OF CONTENTS IV

LIST OF FIGURES VII

LIST OF TABLES XV

NOMENCLATURE XVI

CHAPTER 1: INTRODUCTION 1

1.1. HAEMATOPOIETIC STEM CELL NICHE 3

1.1.1. Haematopoietic stem cells 3

1.1.2. Haematopoietic bone marrow niche 7

1.2. ACUTE MYELOID LEUKAEMIA 10

1.2.1. Leukaemic stem cells 10

1.2.2. Leukaemic bone marrow niche 13

1.2.3. Current and proposed AML treatments 15

1.2.3.1. Repurposing drugs for AML 19

1.3. 3D MODELS OF THE HAEMATOPOIETIC AND LEUKAEMIC NICHE 22

1.4. HYDROGELS 25

1.4.1. FEFEFKFK octapeptide hydrogel 26

1.5. OPTICAL TRAPPING 28

1.5.1. Background 28

1.5.2. Mechanisms and forces 29

1.5.3. Microrheology 33

1.5.4. Biological applications of optical tweezers 34

1.6. OVERALL AIMS / HYPOTHESIS 37

CHAPTER 2: MATERIALS AND METHODS 38

2.1. OPTICAL TRAPPING 38

2.1.1. Sample preparation of beads for optical trapping 38

2.1.2. Sample preparation of cells for optical trapping 38

2.2. MICRORHEOLOGY 39

2.2.1. Water 39

2.2.2. Peptide hydrogel 39
2.2.3. Matrigel 40
2.3. CELL CULTURE 40
2.4. PEPTIDE HYDROGEL PREPARATION 43
2.5. CELL AND BEAD ENCAPSULATION INTO UNMODIFIED PEPTIDE HYDROGELS 43
2.5.1. Human leukaemic cell lines 43
2.5.2. Mouse primary leukaemic cells (mAF9) 44
2.5.3. iPSC-derived HPSCs 44
2.5.4. U937 cell and polystyrene bead co-culture 44
2.5.5. Functionalisation of 6 mg/mL peptide gel 45
2.5.6. Immunocytochemistry (ICC) in peptide gels 45
2.6. CELL QUANTIFICATION USING LUMINESCENCE 46
2.7. DRUG SCREENING 47
2.7.1. Liquid culture 48
2.7.1.1. CellTox™ Green 48
2.7.2. Peptide gel 48
2.7.2.1. 'Early stage' AML model 48
2.7.2.2. 'Established' AML model 49

CHAPTER 3: ESTABLISHING OPTICAL MANIPULATION TECHNIQUES IN 3D PEPTIDE GEL MODELS FOR QUANTITATIVE CELL AND MATRIX ANALYSIS 50

3.1. INTRODUCTION AND AIMS 50
3.2. SET-UP AND CALIBRATION OF THE OPTICAL TRAPPING SYSTEM 50
3.3. CALIBRATION OF OPTICAL TRAPPING POWER 53
3.4. QUANTIFICATION OF OPTICAL TRAPPING STRENGTH USING EQUIPARTITION THEOREM 56
3.5. DEVELOPMENT OF BROWNIAN MOTION BASED MICRORHEOLOGY 61
3.5.1. Theoretical background 61
3.5.2. Water 67
3.5.3. Peptide gel and Matrigel™ 69
3.6. OPTICAL MANIPULATION OF VIABLE CELLS IN PEPTIDE GEL 75
3.6.1. Manipulation 75
3.6.2. Viability analysis of U937 cells 77
3.6.3. Complexities of quantifying cell manipulation 79
3.7. DISCUSSION 81

CHAPTER 4: OPTIMISATION OF PEPTIDE GEL MODELS FOR APPLICATION TO LEUKAEMIC AND HAEMATOPOIETIC STUDY 89

4.1. INTRODUCTION AND AIMS 89
4.2. CULTURE OF HUMAN CELL LINES IN PEPTIDE HYDROGELS 89
4.3. QUANTIFICATION OF CELL NUMBER WITHIN 2D AND 3D CULTURES 92
4.4. EFFECT OF PEPTIDE GEL CONCENTRATION ON U937 PROLIFERATION 94
4.5. CULTURE OF PRIMARY MOUSE LEUKAEMIC MLL-AF9 CELLS IN PEPTIDE GELS... 97
4.6. IPSC DERIVED HSPCS IN PEPTIDE GELS.....100
4.7. DISCUSSION.....102

CHAPTER 5: ASSESSING THE VIABILITY OF LEUKAEMIC CELLS IN RESPONSE TO FDA-APPROVED DRUG TREATMENTS IN 2D AND 3D PEPTIDE GEL MODELS ..109

5.1. INTRODUCTION AND BACKGROUND.....109
5.2. EC50 OF REPURPOSED DRUG TREATED CELLS WITHIN LIQUID CULTURE 110
5.2.1. Preliminary screens 110
5.2.1.1. Salinomycin..... 111
5.2.1.2. Vidofludimus..... 112
5.2.1.3. NB598 113
5.2.1.4. Atorvastatin 114
5.2.2. Extended drug screens 115
5.2.2.1. Selection criteria for extended EC50 analysis..... 115
5.2.2.2. THP-1 cells 116
5.2.2.3. mAF9 cells..... 118
5.2.2.4. U937 cells 120
5.3. COMPARISON OF EC50 VALUES IN 2D AND 3D MODELS.....121
5.3.1. 'Early-stage' AML model..... 122
5.3.2. 'Established' AML model 125
5.4. DISCUSSION 127

CHAPTER 6: FUTURE WORK.....132

6.1. EXTRACTION AND APPLICATION OF MHSPCS 133
6.2. CELL DEFORMATION WITH OPTICAL TWEEZERS.....134

CHAPTER 7: CONCLUSIONS 139

REFERENCES.....140

CHAPTER 8: APPENDIX.....167

8.1. ICC OF U937 CELLS IN PEPTIDE GELS.....167

List of figures

Figure 1.1: A simplified schematic of the cell populations in the bone marrow niche, highlighting how the haematopoietic stem cells (HCSs) reside closer to the endothelial niche than the progenitor or mature cells. Figure made with BioRender. 9

Figure 1.2: Figure illustrating the cancer stem cell hypothesis of how leukaemia may arise from a mutation of a stem cell or a progenitor. Figure created with BioRender.com. 14

Figure 1.3: Schematic illustrating the two-stage process of peptide gel fabrication, highlighting the processes to achieve tuneable stiffness and chemical functionalisation. 27

Figure 1.4: Schematic illustrating the refraction of light travelling from one medium, $n1$, into a particle of higher refractive index, $n2$, then returning into to surrounding medium, $n1$. 31

Figure 1.5: Ray optics explanation of optical trapping for a particle of higher refractive index than the surrounding medium. a. In an unfocused laser when the particle is located at the centre of the laser beam, the resulting lateral force is zero. When the bead is displaced from the centre of the beam, the momentum change causes a net force to be applied back to the centre of the beam. **b.** Particle is in a focused beam. Gradient forces due to intensity gradient constrains the particle in the x and y directions as in **a.**, however the focusing of the beam also constrains the particle in the z direction (where z is the direction of beam propagation). The momentum change of the focused laser rays cause a reactive force towards the laser focus (beam waist), both when the particle lies in front of (left) and behind (right) the focus. At equilibrium, the particle will therefore reside slightly in front of the focus, due to contribution from the scattering force. 32

Figure 2.1: Timeline of differentiation and seeding of haematopoietic stem and progenitor cells in peptide gels. 44

Figure 3.1: **Optical tweezers set-up. a.** Schematic diagram of the optical trapping system including the spatial light modulator (SLM) and indicating the

focal points of the laser, where the distance between L1-L2 and L3-L4 is equal to the sum of their focal lengths. L stands for lens and the dimensions are not to scale. Created with BioRender.com. **b.** Photographs of the optical trapping system showing the laser path. 52

Figure 3.2: Schematic showing the light paths through the inverted microscope. Schematics show the direction of light from the source to the sample when imaging with **a.** white light or **b.** fluorescence. Created with BioRender.com. 53

Figure 3.3: Comparative power measurements from within the laser path to the back of the objective lens. Results shown are an average of 5 repeats with ± standard deviation for each data point. A mean of 58.2 (± 1.5) % power loss was seen between the laser after lens L2 and at the back of the objective lens. 54

Figure 3.4: Transmittance graphs for Nikon CFI Plan Apochromat Lambda 100x oil objective lens[249]. 55

Figure 3.5: Percentage current (%) against laser power (mW) for Ventus IR 1064 nm laser. Laser powers recorded with power meter secured just after lens L2. Error bars calculated on each data point as standard deviation of 3 repeats. Due to losses in the system and through the objective lens the power exposed to the sample will be ≈ 30 % of the values shown here. 56

Figure 3.6: Quantification of bead displacement and laser trapping strength in water with a single optical trap. Laser powers stated were measured in the laser path after lens, L2. For all graphs, the red and blue lines show data in the x and y axes respectively and the error bars were calculated as standard deviation of 3 repeats. **a.** Optical trapping strength calibration (pN/nm) with power (mW) of an optically trapped 2 µm polystyrene bead (N=3). **b.** Mean displacement of an optically trapped 2 µm polystyrene bead from equilibrium with a single focal spot of increasing power. (N=3). **c.** Scatterplots demonstrating the decrease of displacement from equilibrium and corresponding histograms with increasing laser power. 60

Figure 3.7: **Optical trapping strength of a 2 µm bead in water and associated error with number of frames.** The graph shows the displacement of the bead from its equilibrium position along with optical trapping strength at

varying number of frames. The value of the optical trapping strength began to stabilise following 50,000 frames. The standard error of the optical trapping strengths was calculated using $\kappa 2n$, where n is the number of frames[316]. 65

Figure 3.8: Logarithmic plots highlighting the changing corner frequency with increasing laser power for active microrheology. The gradiented areas of the graphs represent the regions over which rheological data can be collected as the beads' movement is freely diffusing within the surrounding material. The regions over which the MSD is unvarying show that the bead is constrained by the trap. The increasing laser power does not alter the gradient of the slope but decreases the region over which rheological data can be collected. The corner frequencies (the lowest frequency that the bead acts as if it is freely diffusing) are circled. .. 66

Figure 3.9: Quantification of the Brownian motion of a 2 µm bead in water. a. Image of a bead within an optical trap taken during recording of Brownian motion. Scale bar = 1 µm. **b.** x-axis versus y-axis displacement scatterplot of active microrheology of water using a 2 µm optically trapped bead (<5 mW at sample). **c,d.** Displacement as a function of time, showing the lack of drift within the system in the x-axis and y-axis respectively. **e.** The mean squared displacement (MSD) plotted against lag time..... 68

Figure 3.10: Complex viscosity, η* (Pa.s) of water against frequency (rad/s) as determined by active microrheology. Results collected using a 2 µm bead within an optical trap (<5 mW). 500,000 data points shown. N=1. 69

Figure 3.11: Scatterplots of 2 µm bead displacement in 6 mg/mL peptide gel optically trapped with ≈ 130 mW at the sample. 6 sets of results from 6 different beads suspended within varying positions and depths within the gel displaying varying scatterplot shape and size. For each bead, a total of 20,000 frames were collected with an interval time of 0.02 ms. 70

Figure 3.12: Complex viscosity of 6 mg/mL peptide gel as measured by optical tweezer-based microrheology and oscillatory plate bulk rheology (performed by Dr Jennifer Ashworth). Microrheology results shown as an average of 5 data sets with 95 % confidence intervals shown in red. 72

Figure 3.13: Microrheological data of 100 % Matrigel™. a. Complex viscosity and **b.** Storage modulus as measured by passive microrheology and bulk

rheology (the latter completed by Dr Jennifer Ashworth) showing a difference of an order of magnitude between the techniques. Microrheology data shows trendline for averaged data across N=3, n=3 with 95 % confidence intervals shown in red..... 74

Figure 3.14: Rheological properties of 10 mg/mL peptide gel as measured by passive microrheology. **a.** Complex viscosity and **b.** storage modulus of 10 mg/mL peptide gel showing 95 % confidence intervals. 75

Figure 3.15: Optical manipulation of live U937 cells in 6 mg/mL peptide gel. Laser focus is shown by a red dot. **a.** U937 cells stained with Calcein AM to indicate viability, optically manipulated within the gel (≈ 60 mW at sample), **b.** U937 cells in 6 mg/mL peptide gels manipulated with up to ≈ 400 mW at sample, showing cell-cell interaction forces limiting manipulation, **c.** 2 µm polystrene beads co-cultured with U937 cells in 6 mg/mL peptide gels, images from left to right demonstrate the process of manipulating the bead to contact a U937 cell then using the bead as an optical handle to move the attached cell (≈250 mW at sample). Scale bars = 10 µm. 77

Figure 3.16: Viability analysis of U937 cells during optical trapping. White light and fluorescence images of the same cell trapped with single focal spot laser in liquid culture (≈450 mW at sample). Culture was stained with Ethidium Homodimer-1 which would fluorescence upon cell death. Scale bars = 10 µm... 78

Figure 3.17: Thresholding of beads compared to non-homogeneous cells. Images of a 2 µm polystyrene bead and U937 cell before and after thresholding performed by MicroManager software in order to determine the particles centre of mass for tracking analysis. 79

Figure 3.18: Optical trapping of polystyrene beads and U937 cells with triple-spot optical traps as formed by an SLM. a. Schematic of how multiple focal spots are formed by the SLM, highlighting the three focal spots used for triple focal spot optical trapping. **b.** Images of single and triple-spot traps with corresponding hologram for the SLM. **c.** Series of white-light images of 3 beads demonstrating trapping and individual manipulation of three optical traps. **d.** Single and triple-spot optical traps placed inside a U937 cell. Scale bars = 10 µm..... 81

Figure 3.19: Example experiment for observing peptide gel response to bead manipulation. Figure shows where scatterplots would be recorded with example corresponding plots should the movement of a bead through the peptide gel form a 'path'. 86

Figure 4.1: Phase-contrast images of human leukaemic cell lines seeded at 5 x 10^4/mL or 1 x 10^5/mL in unmodified 6 mg/mL peptide gels. All cell lines proliferated within the peptide gels showing variation in colony size and density. Scale bars = 100 µm..... 91

Figure 4.2: Quantification of U937 cell number in liquid culture and 6 mg/mL peptide gels. Increasing number of cells quantified using luminescence assays read by plate reader demonstrates a linear relationship between cell number and luminescence in both liquid culture and peptide gel. Results are shown as an average of N=3, n=3, with ± standard deviation. Data collected 1 h following initial seeding..... 94

Figure 4.3: Comparative analysis of U937 proliferation in liquid culture and increasing concentration of peptide gels. a. Phase contrast images taken 7 days after initial seeding, **b.** proliferation percentage measured by RealTime-Glo™ MT viability assay as compared to luminescence read 1 h after initial seeding (1×105/mL) g. **c.** Statistical significance (determined by two-way ANOVA in GraphPad Prism) of data shown in b. *P < 0.05 ,**P < 0.01, ***P < 0.001, ****P < 0.0001. N=3, n=3. 96

Figure 4.4: Phase contrast and confocal images of mAF9 cells in defined conditions of modified peptide hydrogels. Confocal images were taken 6 days following initial seeding and stained with Calcein AM and Ethidium Homodimer-1 to indicate viability. N=2. Scale bars = 100 µm. 99

Figure 4.5: iPSC-derived hHSPCs in unmodified peptide gel. iPSCs were differentiated to a haematopoietic lineage prior to seeding into peptide gels. **a**. Images were taken up to 7 days after initial seeding of the cells showing an approcimate doubling time of 24 h. **b**. Following 7 days of culture in the peptide gels the cells had proliferated in various colony types. Scale bars = 50 µm. N=1. 101

Figure 4.6: Optical manipulation of a cluster of iPSC-derived HPCSs in 6 mg/mL peptide gel a. before and **b.** after movement with up to 250 mW laser power at sample. Scale bars = 100 µm 102

Figure 4.7: Schematic of direct and in-direct cell co-culture of leukaemic and stromal cells in peptide gel using transwells. Figure created with BioRender.com. 107

Figure 5.1: Schematic showing the process of drug screening from 2D liquid culture to 3D peptide gel models. The decision of which drugs and cell types to continue into the next stage of experimentation was determined by the results collected in the previous experiment. 110

Figure 5.2: Salinomycin - Preliminary screens in liquid culture. **a.** Line graphs showing viability of AML cells over time following treatment with salinomycin at the indicated dosage as compared to 0.2 % DMSO vehicle control. Mean values ± standard deviation of biological replicates (N=3, n=3) are plotted throughout. **b.** Confocal images of U937 cells 72 h treatment with salinomycin. CellTox™ Green was used to highlight dead cells. Scale bars = 50 µm. 112

Figure 5.3: Vidofludimus - Preliminary screens in liquid culture. **a.** Line graphs showing viability of AML cells over time following treatment with vidofludimus at the indicated dosage as compared to 0.2 % DMSO vehicle control. Mean values ± standard deviation of biological replicates (N=3, n=3) are plotted throughout. 113

Figure 5.4: NB598 - Preliminary screens in liquid culture. **a.** Line graphs showing viability of AML cells over time following treatment with NB598 at the indicated dosage as compared to 0.2 % DMSO vehicle control. Mean values ± standard deviation of biological replicates (N=3, n=3) are plotted throughout. 114

Figure 5.5: Atorvastatin – Preliminary screens in liquid culture. **a.** Line graphs showing viability of AML cells over time following treatment with atorvastatin at the indicated dosage as compared to 0.2 % DMSO vehicle control. Mean values ± standard deviation of biological replicates (N=3, n=3) are plotted throughout. 115

Figure 5.6: Extended screens in liquid culture with THP-1 cells. **a.** Graphs showing viability of AML cells over time following drug treatment at the indicated

dosage as compared to 0.2 % DMSO vehicle control. Mean values ± standard deviation of biological replicates (N=4, n=3) are plotted throughout. **b.** EC50 values and uncertainty determined using GraphPad Prism nonlin fit agonist vs. response – variable slope (four parameters). 118

Figure 5.7: Extended screens in liquid culture with mAF9 cells. **a.** Graphs showing viability of mAF9 cells over time following drug treatment at the indicated dosage as compared to 0.2 % DMSO vehicle control. Mean values ± standard deviation of biological replicates (N=4, n=3) are plotted throughout. **b.** EC50 values and uncertainty determined using GraphPad Prism nonlin fit agonist vs. response – variable slope (four parameters). 120

Figure 5.8: Extended screen of vidofludimus in liquid culture with U937 cells. **a.** Graph showing viability in mAF9 cells over time following treatment with vidofludimus at the indicated dosage as compared to 0.2 % DMSO vehicle control. Mean values of biological replicates (N=1, n=3) are plotted. 121

Figure 5.9: Schematic showing methods and timings of drug treatments and analysis in 'early-stage' and 'established' AML 3D peptide gel models. Created with BioRender.com. 122

Figure 5.10: THP-1 cells treated with salinomycin, vidofludimus, and atorvastatin in 3D 'early-stage' 6 mg/mL peptide gel models. a-c. EC50 values as determined by the extended screens in liquid culture compared to efficacy of the same dosage with 3D ‘early-stage’ peptide gel models. **d.** Bar graphs displaying time dependency of treated THP-1 cells over 72 h after drug addition to 'early-stage' peptide gel models. For all results, mean values ± standard deviation of biological replicates (N=3, n=3) are plotted with values and uncertainty determined using GraphPad Prism nonlin fit agonist vs. response – variable slope (four parameters). All results presented as percentages compared to vehicle (DMSO) control of 0.02 %. 124

Figure 5.11: THP-1 cells treated with salinomycin, vidofludimus, and atorvastatin in 3D 'established' 6 mg/mL peptide gel models. a-c. EC50 values as determined by the extended screens in liquid culture compared to efficacy of the same dosage with 3D ‘established’ peptide gel models. **d.** Bar graphs displaying time dependency of treated THP-1 cells over 72 h after drug addition to

'established' peptide gel models. For all results, mean values ± standard deviation of biological replicates (N=3, n=3) are plotted with values and uncertainty determined using GraphPad Prism nonlin fit agonist vs. response – variable slope (four parameters). All results presented as percentages compared to vehicle (DMSO) control of 0.02 %. 126

Figure 6.1: Schematic summarising the extraction of HSPCs from murine bone marrow and how they enable direct comparative analysis to the mAF9 cells used in this thesis. Figure created with BioRender.com. 134

Figure 6.2: Schematic showing how optical tweezers can be used to deform cells. Blue arrow indicates the direction of movement of the cell with respect to the fluid flow of the surrounding medium. Created with BioRender.com. 135

Figure 6.3: Figures displaying how the automated analysis software identifies and quantifies cell deformation. a. Example image of an optically trapped mAF9 cell with fitted overlay by the MATLAB program. The overlay (shown in pink) is fitted to each frame of the recording and the software automatically calculates the deformation parameters, highlighting the frames of maximum and minimum deformation. Data collected with the help of William Hardiman. **b.** Schematic of optically deformed cell showing the major and minor axes of deformation, x and y respectively, as measured for calculation of the Taylor deformation parameter. Blue arrow indicates the movement of the cell with respect to the surrounding material. 136

Figure 6.4: Deformation of AML cell lines using optical tweezers (performed and analysed by Aishah Mustapha). N=20. **P < 0.01..... 138

Figure 8.1: Fluorescence images of U937 cells in 6 mg/mL peptide gels. Cells were cultured for 72 h prior to staining for matrix proteins. Scale bars = 20 μm..... 167

List of tables

Table 1.1: Cells within the haematopoietic system 5

Table 1.2: Constituents of the bone marrow niche. 8

Table 1.3: Drugs approved for the treatment of AML since the start of this project. FDA approval date in the US. 18

Table 1.4: Key information of candidate drugs investigated in this thesis. 22

Table 1.5: Comparison of features of 2D cell culture, murine models, and the octapeptide gel used in this study[162,163,231,313–315]. 28

Table 2.1: Media components for primary mouse leukaemia cell (mAF9) culture, where 0.5x and 1x relates to the growth factor concentrations. 41

Table 2.2: Summary of cell types used in this study. 42

Table 4.1: Conditions and modifications added to 6 mg/mL peptide gel for optimisation of mAF9 proliferation. 98

Table 5.1: Efficacy of repurposed drugs on leukaemic cells based upon preliminary drug screens. Where one, two, or three ticks represents a loss of 50 % cell viability after 24 h, 48 h, and 72 h respectively. A cross represents no visible cell death occurred as compared to DMSO control. 116

Nomenclature

2D	two – dimensional
3D	three – dimensional
ALDH	aldehyde-dehydrogenase
AML	acute myeloid leukaemia
ATP	adenosine triphosphate
Atrova	atorvastatin
CLP	common lymphoid progenitors
CMP	common myeloid progenitors
CSC	cancer stem cell
CTG	CellTiter-Glo® Luminescent Cell Viability Assay
D(Asp)	aspartic acid
DHODH	dihydroorotate dehydrogenase
DMSO	dimethyl sulfoxide
E(Glu)	glutamic acid
ECM	extracellular matrix
F(Phe)	phenylalanine
FBS	fetal bovine serum
FDA	food and drug administration
fps	frames per second
G(Gly)	glycine
GGPP	geranylgeranyl pyrophosphate
GVHD	graft-versus-host-disease
HA	hyaluronan
hHSPC	human haematopoietic stem and progenitor cell
HMG-CoA	3-hydroxy-3-methyl-glutaryl-CoA reductase
HPC	haematopoietic progenitor cell
HSC	haematopoietic stem cell
HSPC	haematopoietic stem and progenitor cell
iPSC	induced pluripotent stem cell
IR	infrared
IT-HSC	intermediate-term haematopoietic stem cell
LIC	leukaemia initiating cell
LT-HSC	long-term haematopoietic stem cell

K(Lys)	lysine
mAF9	*MLL-AF9* primary mouse cell line
mHSPC	mouse haematopoietic stem and progenitor cell
MSD	mean squared displacement
NA	numerical aperture
NIR	near infrared
PBS	phosphate buffered saline
PEG	polyethylene glycol
R(Arg)	arginine
RCRC	refractory cancer repopulating cells
ROS	reactive oxygen species
RTG	RealTime-Glo™ MT Cell Viability Assay
Sal	salinomycin
SE	squalene epoxidase
SEM	scanning electron microscopy
SLM	spatial light modulator
ST-HSC	short-term haematopoietic stem cell
ST-HSC	short-term haematopoietic stem cell
TEM	transmission electron microscopy
UV	ultraviolet
Vido	vidofludimus
WD	working distance

Chapter 1: Introduction

Acute myeloid leukaemia (AML) is a cancer of the blood and is responsible for an estimated 2,600 deaths per year in the UK alone, with over 3,000 new cases diagnosed each year[1]. Despite substantial investment into the research and development of treatments, until recently, the identification and translation of successful therapies into the clinic has remained low. This high attrition rate occurs across all cancers and is caused by several factors, including the use of inadequate two-dimensional (2D) models for *in vitro* pre-clinical drug testing prior to clinical trials[2,3]. It is now widely accepted in cancer research that three-dimensional (3D) models critically alter cell behaviour, disease progression, and treatment response with an increased correlation of results to *in vivo* clinical trials as compared to 2D models[4]. This progressively apparent limitation of 2D models has seen a considerable increase in the development of *in vitro* 3D models encompassing physiological conditions relevant to the *in vivo* culture microenvironment.

In reference to AML, the *in vivo* culture microenvironment is known as the haematopoietic niche. The haematopoietic niche primarily exists within the bone marrow and consists of the cells, the extracellular matrix (ECM), and soluble factors such as proteins and growth factors[5]. The niche supports the mammalian blood system, a complex hierarchical structure of progenitor and mature cell types derived from haematopoietic stem cells (HSCs). HSCs are pluripotent with self-renewal capacity, meaning HSCs possess the ability to differentiate into all functional blood cells, and to divide whilst maintaining their undifferentiated state[6]. These properties enable HSCs to balance their proliferation and differentiation to continuously provide more differentiated progenitors to compensate for the short-lived nature of mature blood cells[7]. Of lower frequency in literature, the niche is also responsible for providing mechanical cues to guide haematopoietic cell behaviour. This complex mix of biochemical and biophysical components ensures the regulation between cell proliferation, differentiation, cycling and quiescence[7–9].

Stem cells have become of great clinical importance in recent years, however, recent findings suggest they are not limited to healthy organs or

tissues[10]. Research indicates the presence of a discreet population of cells within tumours, termed cancer stem cells (CSCs), that underpin tumour proliferation, invasion, and metastasis[11]. It is believed that this small population of cells, which have also been termed refractory cancer repopulating cells (RCRCs), or more specifically for leukaemia, leukaemia initiating cell (LICs) or leukaemic stem cells (LSCs), possess limitless self-renewal capacity, and hijack normal haematopoiesis[10]. By taking advantage of the supporting niche, these cells are able to evade chemotherapy, and consequently contribute to re-establishing malignant tumour production, therefore causing eventual disease relapse[12,13]. However, the precise mechanism by which these LSCs evade detection or destruction is so far unknown.

The mechanical properties of the niche and its impact of leukaemogenesis has been widely dismissed up until recent years whereby 3D *in vitro* models revealed the physical properties of the bone marrow niche, such as matrix stiffness to significantly affect leukaemic cell proliferation and treatment [14–16]. However, work continuing from this discovery has been limited by methods able to interrogate the bidirectional interactions of the cells and niche. One method of analysing biological and physical mechanisms that has had a significant impact particularly through-out the field of tissue and cell engineering is optical trapping[17–20]. Optical trapping can be achieved by a system commonly termed optical tweezers that is capable of non-invasively manipulating micro-scale objects[21]. These instruments have been used to apply and measure forces in the pico-Newton range[22], with previous work demonstrating the ability to trap dielectric spheres, viruses, bacteria, living cells, organelles, small metal particles, and even to stretch strands of DNA[21,23–26]. Of importance to exploring the mechanical properties of biological samples, optical tweezers have also been shown to be able to quantify the interaction forces between live cells, and more recently, perform microrheological analysis of viscoelastic materials[18,27–29].

By recognising that the improvement of treatment efficacy is dependent upon an increased understanding of the underlying mechanisms of the disease, this thesis explores the use of a 3D self-assembling peptide hydrogel for investigation into the importance of mechanical cues in leukaemic and

haematopoietic cell behaviour. The novel peptide gel model is free from matrix motifs and aims to address the unmet need of a flexible 3D platform that can be independently modified in biophysical and biochemical properties, such as material stiffness and matrix composition, to allow for the key factors influencing disease progression and treatment response to be separately evaluated *in vitro*. In combination with novel biophysical techniques performed by optical tweezers, these models provide an improved mechanistic understanding of how AML cells evade current therapeutic strategies, providing the first step towards establishing a defined platform with which to screen potential future therapies.

1.1. Haematopoietic stem cell niche

1.1.1. Haematopoietic stem cells

Haematopoiesis in its simplest form can be described as the formation and development of blood. Since the early 2000s, the haematopoietic system has been characterised as a hierarchical system stemming from the HSCs which have the ability to self-renew and differentiate into all blood cell lineages[27,28]. Formed during embryonic development, HSCs undergo asymmetrical cell division to balance the production and regulation of all mature blood cells during the entire life of an organism to ensure blood homoeostasis while limiting cellular damage[6].

HSCs are derived from the mesoderm in close approximation with intraembryonic and extraembryonic blood vessels, they then expand within the foetal liver prior to localising (colonising) to the bone marrow before birth[5,32]. Despite their efficient functionality *in vivo*, providing more than 1 million progenitor blood cells per second within adult humans, it is understood that in the steady state the majority of HSCs are dormant (approximately 90-95 % in adults), with only a limited few supplying the haematopoietic system at any one time[6,33,34].

The initially highly controversial concept of HSCs was first investigated experimentally by McCulloch and Till in 1961 whereby they macroscopically identified multiple haematopoietic lineages in spleen colony-forming units[35]. Although initially debated as definitive HSCs, they found specific progenitor cells with the ability to produce multiple lineages from within a single colony,

demonstrating multipotency. Additionally, the colonies appeared to produce daughter cells with identical characteristics to the parental cell, demonstrating the ability to self-renew. These two properties have since been recognised as defining characteristics for HSCs.

HSCs have been recognised for over 50 years, and have been used within the clinical setting since the 1960s[32]. Within bone marrow it has been estimated that only 1 in 10,000 cells are recognised as HSCs[36], greatly limiting their applications. The ultimate identification and characterisation of HSCs is therefore dependent upon techniques able to isolate this rare cell population. Initial studies to produce a population of increased purity were based upon phenotypic markers such as Hoechst 33342[37]. However, it was the application of flow cytometry with use of a variety of cell surface markers that enabled identification and isolation of HSC populations with the ability to produce multiple lineages upon transplantation, and capability of self-renewal[31,38].

Following the work presented by McCulloch and Till, the haematopoietic system is commonly subdivided into four categories (**Table 1.1**). The first is the HSCs, the most immature population defined by their pluripotency and ability to self-renew. The second is the haematopoietic progenitor cells (HPCs). Unlike HSCs, HPCs are limited in their self-renewal and are only able to generate cell types within a specific lineage (myeloid or lymphoid). The third category includes the precursor cells, common myeloid progenitors (CMPs) or common lymphoid progenitors (CLPs). These cells continue to differentiate into the fourth category of the mature blood cells.

Table 1.1: Cells within the haematopoietic system

Category	Cell types	Properties/function	References
Haematopoietic stem cells (HSCs)	Haematopoietic stem cells (HSCs)	Pluripotent cells capable of producing all blood cells. Possess unlimited self-renewal to replenish whole haematopoietic system.	31,35
Hematopoietic progenitor cells (HPCs)	Myeloid progenitor cells and lymphoid progenitor cells.	Limited self-renewal properties. Multipotent cells that act to replace dead or dying cells as part of ongoing tissue maintenance.	31,39
Precursor cells	Common myeloid progenitors (CMPs) (megakaryocytic-erythroid progenitor (MEP) or the granulocyte-macrophage progenitor (GMP)) and common lymphoid progenitors (CLPs).	Can undergo rapid proliferation before differentiating into mature blood cells.	40,41
Mature blood cells	Myeloid lineage: Red blood cells/erythrocytes, platelets, mast cells, osteoblasts, granulocytes, monocyte-macrophages, dendritic cells. Lymphoid lineage: T-cells/T-lymphocytes, B-cells/B-lymphocytes, natural killer cells, dendritic cells.	Red blood cells carry oxygen around the body, white blood cell help to fight infections and platelets aid in blood clotting.	42

However, the characterisation of stem and progenitor populations is in constant development, with new technologies challenging the rigid and compartmentalised differential structure and showing haematopoiesis to be a functionally and molecularly heterogeneous system that requires continual learning[43]. It is therefore important to recognise that the structure presented in

Table 1.1 is not absolute and the technology and data interpretation is constantly changing.

For example, in 1996, Chaddah et al. published a long-term bone marrow culture model which suggested that the HSC population may be more heterogeneous than first considered, showing HSCs to exist in the bone marrow in two subdivisions, long-term HSCs (LT-HSCs) and short-term HSCs (ST-HSCs)[44]. Here, they found the LT-HSCs to have significant self-renewal ability and demonstrated full reconstitution of mice recipients into all blood lineages. Whereas they suggested that ST-HSCs may be limited to the lymphoid lineage. Succeeding this, in 2014, a review published by Ema et al. discussed that HSCs could be subdivided into 3 separate compartments, ST-HSCs, intermediate-HSCs (IT-HSCs) and LT-HSC, defined by constitution time periods (< 6 months, > 6 months, and > 12 months, respectively)[40]. As suggested nearly 20 years previously by Chaddah et el, this review clarifies nomenclature-based confusion to establish that myeloid-biased HSCs overlap with LT-HSCs, and lymphoid-biased HSCs overlap with ST-HSCs.

In contrast to other stem cell types, HSC use is well-established in clinical applications, and their use as a transplant is a frequented life-saving therapy to treat haematological disorders, such as leukaemia. However, the application of HSCs to treat patients is currently limited by the availability of matching HSC donors[45]. For this reason, much research has been focussed on achieving a better understanding of the underlying mechanisms of the bone marrow niche for future potential production of HSCs *in vitro*. The successful production of a model to recapitulate efficient HSC proliferation *in vitro* would markedly assist our understanding of how haematological diseases, such as leukaemia, originate and interact with the bone marrow niche. Although much research has been conducted into the nature and regulation of the haematopoietic system, the significant immunological barriers *in vivo* in addition to the overwhelming complexity of the bone marrow niche and has meant that the intrinsic and extrinsic regulators that guide HSC fate have been difficult to recapitulate *in vitro*[46].

1.1.2. Haematopoietic bone marrow niche

HSCs and their associated progenitor cells are supported by highly specialised microenvironments (niches), and have been the subject of much research for over 50 years[30,32,47]. A niche is defined by anatomy and function and was first proposed by R. Schofield in 1978 for the HSCs and the bone marrow, stating "the cellular environment which retains the stem cell I shall call a stem cell 'niche.' As long as the stem cell remains fixed its further maturation is prevented and it continues indefinitely to replicate as a stem cell, i.e., it exhibits immortality"[48]. The identification and characterisation of such niches enables the opportunity to discover the key parameters that regulate cellular behaviour, however, despite the ability to extract mouse HSCs for nearly 30 years, research has only recently begun to characterize the niches in which they reside[49].

In addition to supporting the broad range of haematopoietic cells introduced above, the haematopoietic niche is also responsible for regulating multiple non-haematopoietic cellular constituents, the ECM, and soluble factors, together with providing and regulating the physio-chemical and mechanical factors (**Table 1.2**)[50–52]. This complex and highly specialised niche is responsible for balancing these factors for the maintenance of quiescence, mobilization, homing, and apoptosis, including regulating the balance between the self-renewal of HSCs and regulation of differentiation to maintain homeostasis[5,44,53]. Within adult mammalian blood systems the primary niche for haematopoiesis is the red bone marrow of trabecular bones, however, extramedullary tissues such as the spleen and liver can also support HSCs in times of haematopoiesis stress[54].

Table 1.2: Constituents of the bone marrow niche.

Niche Constituents	Components	References
Cellular components	Haematopoietic stem and progenitor cells (HSCs), mesenchymal stem/stromal cells, endothelial cells, perivascular cells, macrophages, osteoblasts, osteoclasts, osteocytes, chimeric antigen receptor (CAR) cells, non-myelinating Schwann cells, sympathic nerves.	7,47,54
Extracellular matrix (ECM) (*most abundant)*	Collagens type I, II, III, IV, V, VI, X, XI, laminin, fibronectin, vitronectin, hyaluronic acid, fibulin, tenascin-C, thrombospondin, chondroitin sulphate, heparin sulphate, keratan sulphate, heparin.	55,56
Soluble Factors (Growth factors, cytokines, hormones)	Stem cell factor (SCF), thrombopoietin, notch, TGFβ/BMP, IGF1, VEGF, N-cadherin, angiopoietin-1 (Ang-1), osteopontin (OPN), WNT.	7,57–60
Physio-chemical	Temperature, pH, normoxia/hypoxia.	47,61
Mechanical factors	Elasticity/stiffness, mechanical stimulation, 3D architecture, shear forces, topography.	52,62

In the bone marrow, HSCs localise near the endosteum, a thin layer of cell-rich connective tissue at the interface of the bone and the bone marrow[63]. More specifically, previous studies using time-lapse confocal microscopy have demonstrated that transplanted HSCs preferentially localise close to the endosteal bone surface, while committed progenitors localize further away (**Figure 1.1**)[54]. This agrees with the previously widely accepted theory that the endosteal bone surfaces act as a quiescent HSC niche, and the vascular niche serves as a self-renewing HSC niche.

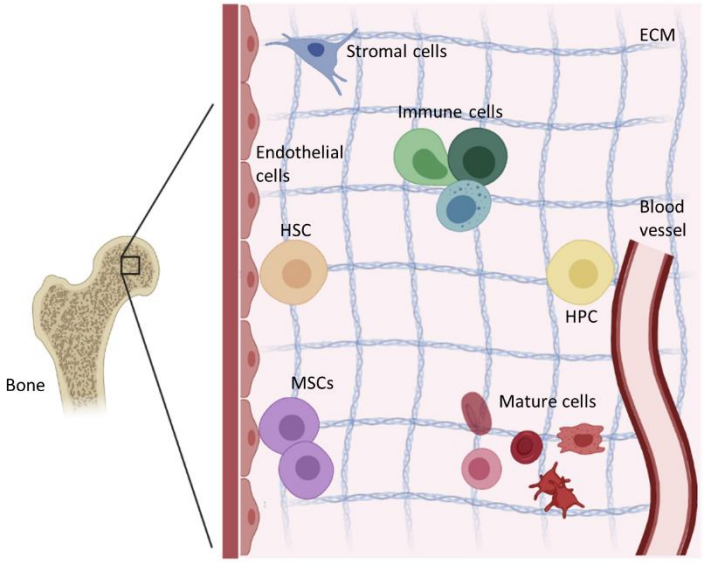


Figure 1.1: A simplified schematic of the cell populations in the bone marrow niche, highlighting how the haematopoietic stem cells (HCSs) reside closer to the endothelial niche than the progenitor or mature cells. *Figure made with BioRender.*

Critical to this thesis is the understanding of the mechanical properties of the bone marrow niche. This includes the mechanical support from the 3D architecture the niche provides, the elasticity of the microenvironment, and the local pore size[57]. This complex assembly of niche components affects not only the HSCs but also the other cellular components which play a supportive role within the microenvironment[46]. As such, the knowledge of the mechanical properties of the niche is critical for modelling the bone marrow in health and disease (see **chapter 1.3**).

The mechanical properties of the bone marrow niche can be characterised using several parameters, such as hydrostatic pressure, induced shear stress, and viscosity[64]. Of these, viscosity is the most commonly quoted value as it can be measured using a wide variety of accessible techniques and therefore allows for direct comparison to a wide range of materials. The viscosity value of the bone marrow has been reported over a large range, dependant on bone marrow temperature and anatomical location[64]. However, a comprehensive study conducted by Metzger et al. in 2014 demonstrated the viscosity of fresh bone marrow to be 100 Pa.s at a shear rate of 1 s^{-1}, decreasing with shear rate according to the power law[65]. Metzger et al. also stated that the previous inconsistencies of

bone marrow viscosity may be due to different storage and handling prior to testing.

1.2. Acute myeloid leukaemia

Leukaemia is a cancer of the blood and can affect all haematopoietic lineages[66]. AML is the most common type of acute leukaemia in adults, and arises from a genetic mutation in haematopoietic stem or progenitor cells (HSPCs) which results in an uncontrollable proliferation of immature leukaemic white blood cells and a blockage of differentiation[67,68]. This increase of white blood cells causes a decrease of healthy red blood cells and platelets which act to carry oxygen around the body and help the blood to clot[69].

AML is an aggressive, heterogeneous, and complex disease with a poor prognosis that accounts for 2 % of all cancer deaths in the UK[70]. AML can present in all age groups, however, there is a strong correlation of incidence with increasing age, with the highest rates being in people over 75[71,72]. AML unfortunately presents with a cure rate of only 5 % - 15 % in patients greater than 60 years old[73].

The symptoms of AML become increasingly evident as the immature white blood cells proliferate. This includes swollen neck glands, easily bruised skin, frequent infections, weight loss, fever, and fatigue[71]. If AML is suspected a blood test is conducted followed by confirmation of diagnosis by a bone marrow biopsy[69]. Following this, the patient may undergo scans to assess the potential spread of cancer to other organs. If AML is confirmed the patient will enter a treatment pathway, some of which are discussed in **chapter 1.2.3**.

The trigger of the genetic mutation that causes AML is currently unknown, however, several factors could increase the risk. These include, smoking, radiation exposure, aging, blood or genetic disorders, or previous treatment with radiotherapy or chemotherapy[74].

1.2.1. Leukaemic stem cells

There have been numerous proposed theories to explain the cell of origin and heterogeneity of cancerous cell populations. Two major theories are the

clonal evolution theory and the cancer stem cell model[75,76]. Although these two approaches are not mutually exclusive, they are fundamentally different, and awareness of which model LSCs follow will help improve our understanding of leukaemia initiation, prevention, and treatment.

The clonal evolution theory suggests a 'back to Darwin' model of cancer propagation, proposing malignant phenotypes develop from normal cells that have acquired mutations to allow for proliferative advantages, enhancing their survival under selective pressure[77]. Although both theories support the involvement of the bone marrow niche, clonal evolution theory contrasts to the CSC theory as the latter does not address whether cancer arise from normal stem cells[75]. Rather it proposes that irrespective of cell of origin, cancer cell populations are a heterogeneous population of cells with a hierarchical organization similar to that of normal haematopoiesis; in which there is a smaller sub-population of cells, such as the quiescent HSCs, with unlimited self-renewal potential[78]. Leukaemia has been considered to arise from a combination of these theories, with the highly differentiated haematopoietic cells suggesting hierarchical organization[79,80], and the increasing resistance to therapies suggesting mutations by clonal evolution. It is important to note that this is an ongoing discussion, however, due to compelling data such as Lapidot et al., and Bonnet and Dick, leukaemia is commonly regarded as produced by the cancer stem cell model[81,82].

The existence of CSCs was first theorised by pathologist Rudolf Virchow in 1855, proposing their existence stemmed from the activation of dormant embryonic-like cells from mature tissue[78]. Despite this early hypothesis in 1855, it was over a century later in 1994 that Lapidot et al. provided experimental evidence to support the CSC hypothesis, whereby they analysed cell-surface protein markers ($CD34^+$ $CD38^-$) to identify a relatively rare population of stem-like cells that exist within AML[81]. It was discovered that within the peripheral blood of a person with leukaemia, approximately 1 in 250,000 cells could initiate AML when transplanted into an immunosuppressed mouse. This was the first successful isolation of LSCs and owing to this discovery the existence of CSCs has since been extended to a broad spectrum of solid tumors[83–85].

Since their discovery, a consensus panel assembled by the American Association of Cancer Research has defined CSCs as a cell that exists within a tumour with the ability of self-renewal to cause the heterogeneous lineages of cancer cells that comprise the tumor[86]. It is important to note that this definition does not address the source of these cells, meaning we are still yet to recognize whether leukaemia originates from stem, progenitor, or maturely differentiated cells (**Figure 1.2**). For this reason, CSCs are often called RCRCs, or tumour-initiating cells to avoid confusion.

With reference to their potential origin, previous studies suggest aberrant HSC development can cause production of these malignant subtypes, therefore highlighting the importance of the balance of haematopoiesis[66]. For example, if HSC differentiation into mature blood cells is not accompanied by the regular loss of self-renewal capacity, or HSCs do not fully differentiate to committed progenitors, they may enter a pre-leukemic state[6,87,88]. Leukaemia has also been theorised to occur most commonly in the elderly due to the accumulation of damage in the haematopoietic system, resulting in dysfunctional haematopoiesis[89].

Since the start of this project, Blume et al. published a paper in which they studied aldehyde-dehydrogenase (ALDH) activity to show that leukaemia derives from HSPCs (as opposed to more mature cell types)[90]. From previous knowledge of the correlation between the stem cell marker ALDH and poor prognosis of AML; this study showed that AML with increased ALDH expression favoured leukaemic engraftment, and in addition to comparative gene-expression analysis of $CD34^+$ cells they concluded that an increased expression of LSC signatures in ALDH-rich AML suggested more aggressive AML to derive from a stem cell-like origin.

A further challenge regarding the recognition of LSCs is distinguishing them from the HSC population, as the $CD34^+$, $CD38^-$ phenotype is shared between these populations of cells[12]. Previous research has explored the use of other cell surface markers, such as CD96 with limited success[91,92]. Recently, CD123 has emerged as a promising target. CD123 is a membrane biomarker with limited/absent expression on normal haematopoietic stem cells, in contrast to AML which has shown expression both on the bulk leukaemic blast cells and enrichment in LSCs[93].

For this reason, several CD123-targeted therapies are currently in clinical development using $CD34^+$, $CD123^+$, $CD38^-$ as the leukaemic phenotype[91,94–96]. Despite this, as of today, there is no universal marker to conclusively distinguish AML blasts from normal haematopoietic cells[97]. This therefore limits the ability to identify LSCs, and consequently, the ability to produce leukaemic-specific targeted therapies.

1.2.2. Leukaemic bone marrow niche

As discussed **above**, the bone marrow niche provides biochemical and mechanical support to the haematopoietic system, however, upon initiation of AML, the niche is drastically remodelled to support pathological functions. AML progressively occupies the bone marrow niche which transforms it into a "leukaemia growth-permissive" and "normal haematopoiesis-suppressive" environment[98,99]. In recent years, this remodelling has emerged as a critical factor in leukaemia development and chemoresistance, affecting the complex bi-directional interactions between the cells and the niche that control disease development[100,101]. However, the process by which the leukaemia hijacks the healthy bone marrow and evades treatment is still largely unknown. Furthermore, with reference to **Table 1.1** which characterises the constituents of the healthy bone marrow niche, the leukaemic microenvironment is not known to differ in many characteristics. For example, as mentioned above, the phenotypic biomarkers for HSCs and LSCs are very similar, and most applicably to this study, unlike solid cancers, the mechanical properties such as the stiffness/viscoelastic properties of the niche have not been reported to change in leukaemic malignancy[102].

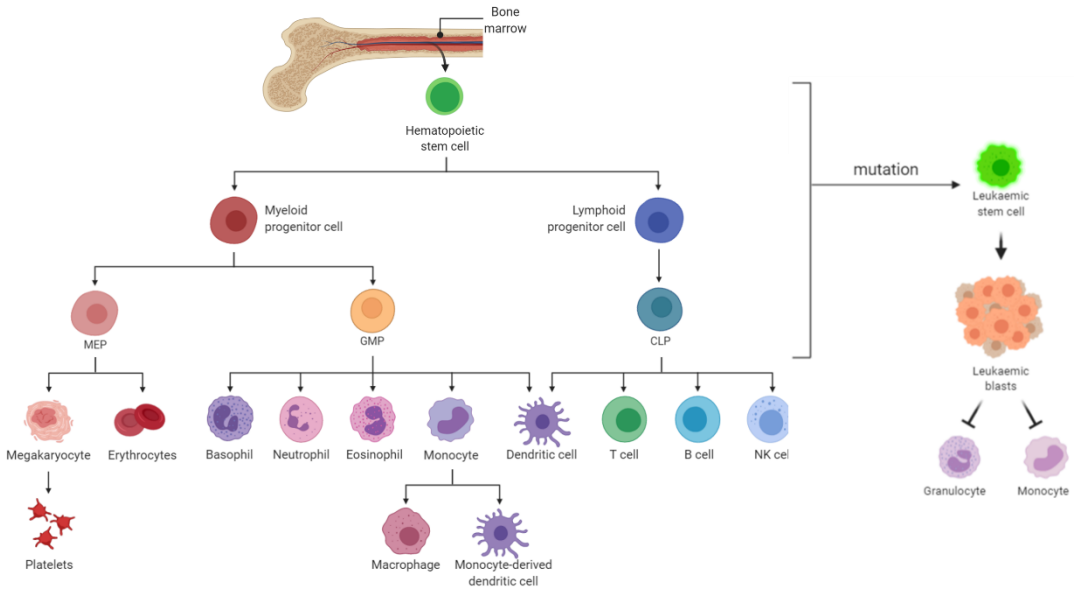


Figure 1.2: Figure illustrating the cancer stem cell hypothesis of how leukaemia may arise from a mutation of a stem cell or a progenitor. *Figure created with BioRender.com.*

Among the first to notice the connection between the bone marrow niche and leukaemia progression was Walkley et al. in 2007[103,104]. In these papers, the teams showed that selective targeting of the retinoblastoma protein within the bone marrow niche leads to a myeloproliferative disorder similar to that seen *in vivo*, in addition to a decrease in HSC numbers. This conclusively showed the bidirectional dependence between the leukaemic cells and the microenvironment, and importantly, that alterations or perturbations in niche signalling can mimic diseases.

Since this discovery, the field has recognised that the unlimited proliferation and abnormal differentiation of the leukaemic blast cells leads to suppression and loss of function of the normal haematopoietic system and creates a self-strengthening leukaemic niche[105–108]. As mentioned above, little is known about how this alteration occurs, however, in 2018 Kumar et al. explained the transformation of the niche occurs at least partially through exosome secretion[98]. They showed that engrafted AML cells and AML-derived exosomes caused variation in bone marrow response in line with leukaemic development (induction of DKK1, a suppressor of normal haematopoiesis), and that disruption of exosome release significantly delayed leukaemia progression.

Although of significantly lower frequency in literature, the mechanical influence of the niche has also been investigated. In 2020, Zanetti and Krause reviewed the ECM in normal haematopoiesis and leukaemia, highlighting the frequently overlooked role of the ECM to regulate the structural scaffolding by means of stiffness and deformation[15]. The importance of including physiologically representative mechanical cues in AML models was highlighted in recent findings demonstrating 3D culture to more closely predict *in vivo* efficacy of anti-cancer drugs as compared to conventional 2D culture[109–111]. Although the viscosity of the bone marrow is not known to alter from health to AML, the mechanical properties of the bone marrow have been shown to hold great influence over AML behaviours and drug response. Most notably this was addressed in 2016 by Shin and Mooney. This study showed that pathologically relevant matrix softening accelerated leukaemic cell proliferation and causes resistance to standard chemotherapy[111].

The advancement of a mechanical understanding of the niche's role in AML development has mirrored the development of microscopy able to visualise *in vivo* cell and tissue dynamics. Of note is a paper by Duarte et al. in 2018[99]. With the aim of investigating the elusive process by which the leukaemic cells hijack the niche, Duarte et al. used intravital microscopy to visualise the bone marrow niche in mice. Using immunocytochemistry, this paper showed that as AML progresses in mice the number of HSCs and osteoblasts decrease. Fluorescence intravital microscopy shows expansion of AML results in a significant remodelling of the central and endosteal bone marrow niches. The expansion of AML cells within the endosteal regions outcompete the healthy bone marrow cells over time, decreasing the haematopoietic cell and osteoblastic cell capacity.

1.2.3. Current and proposed AML treatments

The standard therapeutic treatment for AML has been largely unvaried over several decades. Depending upon the subtype of AML, 4 types of treatment can be considered: chemotherapy, chemotherapy with a stem cell transplant, radiation therapy, or another drug therapy during or after US Food and Drug Administration (FDA) clinical trial.

The most common course of treatment upon diagnosis of AML is chemotherapy. Chemotherapy can be delivered to the patient orally, intravenously, intramuscularly, or into the spinal fluid (intrathecal)[112]. The latter is able to treat AML that has spread to the brain and spinal cord, however, most commonly it is administered intravenously. Chemotherapy is an aggressive treatment that acts to stop the growth of cancer cells, either by killing the cells or by preventing further proliferation. For AML, the most common chemotherapy drugs used are a combination of cytarabine and an anthracycline drug such as daurubicin[113].

One of the issues of chemotherapy is that it does not distinguish cell type, meaning the healthy haematopoietic cells are also killed by these treatments. For this reason, a stem cell transplant can be required to replenish the blood-forming cells within the bone marrow. Transplantation of HSCs from a healthy, compatible, donor is well-established in clinical applications to treat haematological disorders, including leukaemia. However, the application of HSCs to treat patients is currently limited by availability of matching donors[45].

Radiation therapy can be delivered internally by inserting a radioactive substance directly into or near the site of the cancer, or externally by using a high energy x-ray to radiate the cancer. Contrary to chemotherapy, radiation therapy is able to be localised to the cancer. Radiation can be used alone or combined with chemotherapy to try to ensure comprehensive treatment[71].

A high percentage of AML patients enter remission following initial treatment; where remission is determined by 3 factors: 1. the bone marrow cell population comprises less than 5 % of leukaemic blast cells, 2. the patients' blood count is back to normal, and 3. the patient is not experiencing any symptoms of AML[114]. However, in many cases, in both children and adults, AML can relapse over time due to the LSCs evading treatment by hiding within the bone marrow niche. AML relapse is most common within the first year following notice of remission and remains a leading cause of death for this disease[115]. Treatment for AML can therefore consist of 2 phases: remission induction therapy and post-remission therapy. Aggressive post-remission treatments, such as high-dose chemotherapy

can reduce the probability of relapse, but this option cannot be made available to AML patients too weak to tolerate the severe treatment.

Chemotherapy is, therefore, an inefficient treatment for cancer, in addition, it is a painful and expensive procedure. As a result, the proposed future treatments for AML and other cancers aim to improve the ability of the therapies to specifically target the malignant cells without affecting healthy, supportive cells. These targeted therapies can be categorised into 3 groups[116]: 1. Drugs that act by targeting cancer-specific gene mutations, 2. Drugs that inhibit key signalling pathways to affect cancer progression, 3. Drugs that deliver cytotoxic reagents to targeted cancer cells.

Despite the knowledge that cancer is the leading cause of death worldwide combined with heavy investment in research, anticancer drugs have the lowest likelihood of approval within drug development[2]. According to clinical data, there is a 3.4 % chance of an anticancer drug entering clinical development compared to other non-cancer drugs which present a 10 % success rate[117,118]. One of the challenges facing drug discovery and resulting in these high attrition rates for leukaemia is that AML is a highly heterogeneous disease. Previously, patients diagnosed with the same disease were considered to suffer from the same pathology, and therefore the same treatment. However, as not all AML present in the same manner from the same genetic mutation, patients often respond very differently to the same treatment[2]. Since the start of this project in 2017, 8 targeted therapies have been FDA approved for the treatment of AML with the aim of developing an efficient treatment with fewer or less severe side effects (**Table 1.3**).

Table 1.3: Drugs approved for the treatment of AML since the start of this project. *FDA approval date in the US.*

Drug name	Target	Mechanism of action	FDA status	References
Midostaurin (Rydapt)	Newly diagnosed FLT3 mutated AML (+chemo)	Protein kinase C inhibitor, however, benefit may arise from currently unknown off-target effects	Approved 2017	119–121
Gilteritinib (Xospata)	Relapsed/refractory FLT3 mutated AML	Oral protein kinase inhibitor which acts to block FLT3	Approved 2018	119,122,123
Enasidenib (Idhifa)	Relapsed/refractory IDH2 mutated AML	Isocitrate dehydrogenase 2 (IDH2) enzyme inhibitor	Approved 2017	119,124–126
Ivosidenib (Tibsovo)	Newly diagnosed and relapsed/refractory IDH1 mutated AML	Oral targeted small molecule inhibitor of mutant IDH1	Approved 2019	119,127,128
Venetoclax (Venclexta)	Newly diagnosed AML ≥ 75 years or comorbidities (+hypomethylating agent) or (+low dose cytarabine)	Selective BCL2 inhibitor	Approved 2018	119,129,130
CPX-351 (Vyxeos)	Newly diagnosed AML-MRC and t-AML	Delivers encapsulated chemotherapy to AML cells	Approved 2017	119,131,132
Glasdegib (Daurismo)	Newly diagnosed AML ≥ 75 years or comorbidities	Inhibitor of the hedgehog signalling pathway	Approved 2018	119,133,134
Gemtuzumab ozogamicin (Mylotarg)	Newly diagnosed and relapsed/refractory CD33-positive AML. (Alone or with standard chemotherapy)	CD33 monoclonal antibody linked to a cytotoxic agent	Approved 2017	119,135,136

1.2.3.1. **Repurposing drugs for AML**

An increasingly important challenge in cancer drug development is not only to prove a new therapy is capable of eliminating the disease safely, but also to do it in a rapid and cost-effective manner. As of 2020, developing a drug treatment from discovery to clinical application costs an average of 2.5 billion dollars, with the most expensive part of the process being clinical trials which consume approximately 50 % of the total investiment[2,117]. Additionally, according to Cancer Research UK it can take 10 to 15 years or more to complete clinical trials prior to drug licensing[137]. For these reasons, recent years have seen an increasing interest in drug repurposing.

Drug repurposing is a system for identifying new applications for drugs outside the disease of their initial approval[138–140]. This strategy holds various advantages against establishing a novel drug, including reducing the costs, time and risks associated with translating a treatment into clinical use. Repurposed drugs minimise risks of failure due to previous knowledge of long-term side effects and reduce the time and cost as most of the preclinical testing and safety verification has been completed. This means that only regulatory and phase III clinical testing is required, increasing the bench-to-bedside efficiency.

Several drugs initially targeted towards other diseases have found to be effective against AML. Although any repurposed drugs have yet to be approved by the FDA for AML, in 2020 Wojcicki et al. efficiently summarised the repurposed clinical candidates currently under investigation for their application to AML[117]. This includes, tranylcypromine, sertraline, ribavirin, HMG-CoA reductase inhibitors, valproic acid. Previous candidates such as tigecycline, thioridazine, and metformin have been dismissed due to lack of efficacy, toxicity, or slow accrual.

Within this thesis, four FDA-approved drugs have been explored for their repurposing efficacy in AML. These drugs were salinomycin, vidofludimus, atorvastatin, and NB598 (primary applications and rationales summarised in **Table 1.4**). The rationale for the selection of each these drugs is described below, however we previously used connectivity mapping to identify candidate drugs, including an antibiotic, for repurposing as anti-leukaemic agents[141,142].

Although initially targeted an antibacterial drug, salinomycin is a coccidiostat ionophore which has been shown to selectively eradicate CSCs. In a screen of over 16,000 compounds conducted by Gupta et al. salinomycin was found to be 100x more effective in the treatment of breast cancer in mice compared to paclitaxel, a commonly used chemotherapeutic drug[143]. Following this success, Roulston et al. applied this drug to AML and showed salinomycin to eradicate human leukaemia cell lines and mouse primary AML cells in 2D liquid culture without affecting the colony formation of healthy haematopoietic cells[142]. Additionally, a small pre-clinical trial for targeting human CSCs showed the ability of salinomycin to eliminate CSCs and to induce partial clinical regression of treatment-resistant cancers with minimal side effects at relevant dosages[144].

The mechanism of action of salinomycin remained elusive for several years. In 2017, Thi Mai et al. provided evidence that salinomycin operates by accumulating and sequestering iron in lysosomes, organelles located within the cytoplasm of cells[145]. In response to the depletion of iron in the lysosomes, the cells degrade ferritin, a cytosolic protein that stores excess iron which is utilised when cells become iron deficient[146]. This leads to the production of reactive oxygen species (ROS), lysosomal membrane permeabilization and cell death consistent with ferroptosis. As cancer cells are generally characterised by high intracellular iron content, salinomycin is able to selectively target CSCs[147].

Vidofludimus is a small molecule with a dual mode of action. *In vitro,* vidofludimus has been found to block the proliferation of metabolically activated T- and B- cells by inhibiting dihydroorotate dehydrogenase (DHODH), and inhibits the expression of pro-inflammatory cytokines including interleukin-17 and interferon-gamma by interference with the JAK/STAT and NFκB pathways (both involved in immune cell survival and cytokine production)[148]. Previous DHODH inhibitors, such as leflunomide and teriflunomide, have reported serious adverse effects, however, vidofludimus is a selective second-generation DHODH inhibitor which as of late 2019 demonstrated a positive safety profile[149].

DHODH inhibitors are a validated therapeutic target for other diseases, such as rheumatoid arthritis and multiple sclerosis, however, DHODH is an unlikely target for cancer treatments as it is not known to be mutated nor overexpressed

in cancer[150,151]. This has been reflected in the investigation of DHODH inhibitors in solid tumour malignancies, which have shown disappointing clinical translation. However, DHODH inhibitors have demonstrated a cytotoxic effect in AML, and enable the AML blasts to overcome the differentiation blockade[151,152]. Vidofludimus was selected for this study as DHODH inhibitors entered clinical trials in 2018 with the aim of providing further insight into their potential against haematological malignancies[151].

Atorvastatin is part of a group of medicines called statins which are commonly prescribed to lower blood cholesterol. Atorvastatin is currently being sold as an oral medication for the prevention of cardiovascular disease and strokes under the brand name Lipitor[153]. Statins have been shown to inhibit cancer cell proliferation *in vitro* and in animal models by inducing targeted apoptosis which is activated by suppression of mevalonate or geranylgeranyl pyrophosphate (GGPP)[154]. However, the molecular mechanisms behind these anti-cancer effects are still unknown.

In 2019, atorvastatin was shown by Zhang et al. to have an anti-leukaemic effect on K-562 and HL60 AML cells[155]. This paper showed the atorvastatin inhibited YAP nuclear localisation which could be reversed by the addition of mevalonate, farnesyl pyrophosphate, or GGPP. Together with their findings of changes in apoptosis-related proteins and cell cycle arrest upon treatment with atorvastatin which could be reversed in the same manner, they concluded that atorvastatin may act on AML through the mevalonate-YAP pathway. As of 2020, atorvastatin has been taken through 2 clinical trials with regards to AML, both investigating its ability to prevent graft-versus-host-disease (GVHD). Since the start of this project, atorvastatin has started within a pilot clinical trial for investigation into its ability to decrease the mutant tumour protein 53 (p53) in solid tumours and relapsed AML[156].

First reported in 1990, NB598 is also an anti-cholesterol and inhibits squalene epoxidase (SE) (an enzyme within the cholesterol biosynthetic pathway). Recently, SE was identified as a potential therapeutic target for certain neuroendocrine tumours but has yet to be recognised in relation to haematological cancers[157]. NB598 was selected for this study due to preliminary,

unpublished, data collected at the University of Nottingham which showed correlation between NB598 treatment of AML cell lines and cell membrane stiffness (discussed further in **chapter 6.2**).

Table 1.4: Key information of candidate drugs investigated in this thesis.

Candidate drug	Supplier	Primary application and mechanism of action	Rationale
Salinomycin (sal)	Sigma Aldrich, UK	Coccidiostat ionophore widely used in chicken feed. Sequesters iron from lysosomes leading to cell death consistent with ferroptosis.	Previously shown to be effective against AML in 2D liquid culture without affecting haematopoietic colony formation[142].
Vidofludimus (vido)	SelleckChem, Germany	DHODH inhibitor. Inhibits proliferation of activated T- and B-cells. Currently used as an oral treatment for inflammatory diseases.	Previous work suggests vidofludimus causes AML cell death, and enabled AML blasts to overcome the differentiation blockade[151,152].
Atorvastatin (atorva)	SelleckChem, Germany	Statin commonly used to lower blood cholesterol. Inhibitor of HMG-CoA reductase.	Various statins have been shown to inhibit CSC properties, induce apoptosis, and stop the cell cycle[158]
NB598	MedChem-Express, USA	Small molecule inhibitor of squalene epoxidase (SE) which affects the cholesterol biosynthetic pathway.	As above. Preliminary data (unpublished) shows NB598 to decrease leukaemic cell stiffness.

1.3. 3D models of the haematopoietic and leukaemic niche

The current clinical process for taking a drug from discovery to market can be broadly separated into 4 sections; early discovery, preclinical studies, clinical development, and FDA approval. Typically, the early discovery is identified and validated in 2D culture, before moving into *in-vitro* and animal models in preclinical studies, followed by human studies in clinical development.

The requirement of 3D *in vitro* models and animal models before human trials stems from the widely accepted limitation of 2D models to accurate recapitulate *in vivo* cell behaviours within the field of disease modelling[46,159–161]. The conditions experienced by cells in 2D culture are greatly simplified compared to those *in vivo* with cells demonstrating inferior cell morphology, phenotype, and cell-matrix interactions as compared to 3D models[162,163].

As with many cell types, haematopoietic and leukaemic cells are commonly cultured within 2D flasks. Within this environment, it has been shown that the self-renewing potential of HSPCs is impeded and lost in favour of differentiation, demonstrating its insufficiency to mimic the *in vivo* behaviour of HSCs[164–166]. This therefore means that standard liquid cell culture is limited for targeted proliferation, differentiation and for effective drug screening[52]. Despite this, 2D culture remains in frequent use for laboratory research due to its ease and low cost.

For preclinical leukaemia research, mice are the current gold standard[167,168]. These *in vivo* models emulate the full complexity of the bone marrow niche, and, aside from the phenotypic differences from size, the heterogeneity of the bone marrow from both species is reportedly very similar[169,170]. Importantly for the study of leukaemia, the currently genetic definition for leukaemia (CD34+, CD38-) is observed in both species[81,171,172]. However, within these models it can be difficult to interpret the key parameters that guide the behaviours of the cells[46,173]. Furthermore, many drugs that are deemed successful within preclinical animal trials do not succeed within humans[174]. This has led to a dissociation between animal clinical trials and human efficacy, which in turn results in unnecessary wastage of time, expense, and animal lives. This deficiency shows the inability of current preclinical testing to accurately mimic the AML microenvironment and highlights the need for the development of a defined, customisable model. For this reason, recent years have seen great interest in *in vitro* models to allow for selectively addressing niche parameters for investigation into cell behaviours and drug treatment response[46,174–176].

One of these parameters that has yet to be fully understood in its role in regulating these behaviours is the mechanical support. The addition of a 3D

support impacts the spatial organisation of cells, cell-cell interactions, the delivery and transport of nutrients and signalling molecules, and the production and localisation of matrix produced by the cells, in addition to adding physiologically relevant factors such as elasticity/stiffness and mechanical stimulation[161,177]. Due to the structure-function relationship, this is followed by biological changes of cell cytoskeleton organisation, morphology and focal adhesions[16,178]. This behaviour within 3D models has been shown to be a much closer representation of *in vivo* models as compared to 2D[161,162]. However, the underlying mechanisms by which the 3D architecture affects the cells behaviours has yet to be exploited for their application to cancer research.

As suggested by El-Sherbiny et al., the key processes followed to produce an idealised, functional 3D model can be distilled into 4 primary components[179]: 1) selected cells are isolated, 2) the cells can be encapsulated in a natural or synthetic scaffold, providing a platform for cell proliferation and differentiation, whilst supporting cell adhesion and permitting adequate transport of nutrients and gases, 3) the scaffold can be functionalised with signalling molecules such as ECM proteins and growth factors relevant for stimulating cellular functions of interest, 4) the scaffold structure and function can be individually controlled to best mimic the natural *in vivo* niche.

Typically, 3D models are considered for solid tissues and malignancies, however, non-solid tumours such as haematological malignancies also require 3D models to recapitulate the complexity of the bone marrow niche[177]. As of 2020, numerous biomaterial-based models have been investigated to elucidate the bidirectional interactions between the AML cells and the niche that regulate disease initiation and development[180–183]. Of note, Harada et al. published a 3D model not only capable of maintaining a population of HSPCs over 4 weeks of culture but also used this model to show that the number of K-562 cells in the G0/G1 phase was significantly higher than in 2D culture[184,185]. This study stems from work showing how bone marrow-based matrix cues affect various important cell behaviours such as morphology, proliferation, and lineage bias of HSCs[186].

Furthermore, the mechanical support of a 3D model is a significant factor in the drug resistance observed in AML[105,183,187,188]. 3D models are therefore

imperative to study how therapeutics are received by the cells to address the poor correlation observed between preclinical *in vitro* and *in vivo* data[187,189]. Of specific interest to this project, Mooney et al. recently demonstrated a 3D platform based on mechanically tuneable alginate hydrogels[111]. These hydrogels were able to be mechanically tailored to mimic a range of tissue-relevant stiffnesses, showing an increase of matrix stiffness up to 300 Pa increases the proliferation of myeloid leukaemia's followed by a decrease in proliferation at 3000 Pa. They also demonstrated matrix stiffness to affect AML sensitivity to chemotherapeutic agents, showing K-562 and MOLM-14 cells to significantly increase their efficacy to numerous drugs within a matrix of higher stiffness. This study demonstrates the importance of including 3D mechanical cues within AML models.

1.4. Hydrogels

Due to their ability to be modified and adapted to provide a range of tissue-specific mechanical and biochemical properties, hydrogel-based models have provided a tissue-realistic platform for investigating ECM environments. Hydrogels can be created using natural or synthetic components, and can be prepared by various methods depending on the desired functionality and application[179]. This flexibility has led to a significant body of research utilising hydrogels as drug delivery systems, carriers for cell transplantation, and scaffolds for *in vitro* models to mimic a wide range of tissues such as neural tissue, breast tissue, or bone[179,190–194].

Of common use as a 3D *in vitro* model is Matrigel™. Matrigel™ is a basement membrane extract derived from Engelbreth-Holm-Swarm mouse sarcoma and has successfully supported the proliferation of many cell types, producing an accessible, relatively easy to use platform for 3D tissue culture[195–197]. However, as a tumour extract, Matrigel™ is compositionally undefined and is highly susceptible to batch-to-batch variation. Although to a lesser degree, this is also the case for other hydrogels that incorporate a biological component as its basis (e.g., collagen or hyaluronan hydrogels).

Despite their successes, their biological origin means there are two major limiting factors for these hydrogels: 1. Their ability to detect and differentiate between endogenous matrix produced by the encapsulated cells and the matrix within the biomaterial which has been remodelled by the encapsulated cells, and 2. The ability to independently assess the mechanical and biochemical influences of the hydrogel on the cell's behaviours. These factors limit the hydrogels' ability to recapitulate the characteristics of the tissue of interest and does not allow for individually examining the impact of matrix stiffness or the addition of matrix components.

1.4.1. FEFEFKFK octapeptide hydrogel

This project therefore utilised a synthetic self-assembling peptide hydrogel. The FEFEFKFK (Phe-Glu-Phe-Glu-Phe-Lys-Phe-Lys) octapeptide hydrogel used in this study forms through self-assembly of nanofibers to create a physically cross-linked β-sheet structure[198]. Individually modifiable in their chemical and mechanical properties, the stiffness of these hydrogels can be independently tailored to reflect the tissue of interest, and can be functionalised by addition of relevant ECM molecules, proteins, and growth factors[199,200]. Without biochemical modification, the FEFEFKFK peptide gel is a biologically inert model as it does not contain any binding motifs. This property allows for defined addition of desired matrix components and enables alteration of stiffness independent to any matrix motifs. Furthermore, their synthetic structure means that unlike biological-based hydrogels, the peptide gel is not disposed to batch-to-batch variation and as such is ideally suited as a reproducible platform.

The fabrication of the peptide gel can be subdivided into two main sections, the first section leading to the production of a precursor gel which regulates the mechanical (stiffness) properties of the gel by control of the volume of peptide powder, and the second section where the biophysical properties can be modified by addition of cells and matrix components (**Figure 1.3**).

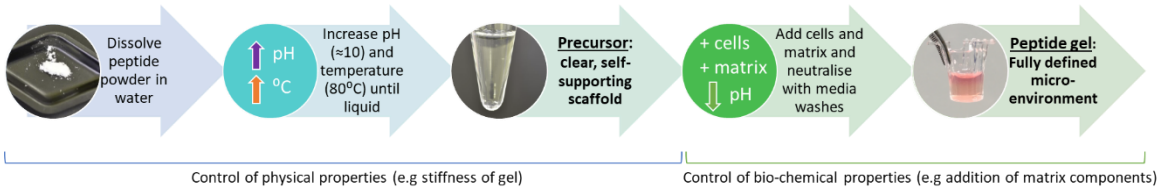


Figure 1.3: Schematic illustrating the two-stage process of peptide gel fabrication, highlighting the processes to achieve tuneable stiffness and chemical functionalisation.

In addition to addressing both limiting factors of biological-based hydrogels as discussed **above**, a further property of this gel beneficial to the application as a 3D *in vitro* model is that it can undergo liquid-gel-liquid transitions for homogenous cell suspension. Also, the peptide gel does not auto-fluoresce and is optically clear upon gelation, meaning the 3D models can be imaged using white-light and fluorescence microscopy during proliferation. For direct comparison, the main features of currently used models (2D culture, and murine models) are shown with the peptide gel models in **Table 1.5**.

Table 1.5: Comparison of features of 2D cell culture, murine models, and the octapeptide gel used in this study[162,163,231,313–315]**.**

Feature	Model type		
	2D culture	Murine models	Octapeptide gel
Ease of use (imaging/passaging)	Yes	No	Yes
Physiologically relevant spreading and migration	No	Yes	Yes
Physiologically relevant cell-cell interaction	No	Yes	Yes
Soluble gradients	No	Yes	Yes
Physiologically relevant complexity	Limited	Yes	Can be adjusted in complexity
Physiologically relevant cell morphology	No	Yes	Yes
Relative cost	Low	High	Medium/high
Reproducibility	High	Limited	High
Data Provider	High	Low	High

1.5. Optical trapping

1.5.1. Background

The study of complex cellular microenvironments has been greatly limited by the availability of techniques to analyse cellular behaviour at the single-cell scale. The ability to non-destructively interact with multicellular microenvironments will enable a deeper understanding of cellular behaviour and biological function; a challenge that will assist many research fields, such as regenerative medicine and tissue engineering, in addition to drug and pharmacology development. One such technique capable of micromanipulation with resolution able to study the precise architectural relationship of cells and their niche is optical trapping.

Optical tweezers were invented 50 years ago by Arthur Ashkin and are based on the observation that light radiation can exert a force on

micrometre-sized particles[201,202]. This phenomenon was initially recognised by Johannes Kepler who observed that the solar pressure causing the tail of a comet to always point away from the sun[203]. The application of optical tweezers to the biological field earned Arthur Ashkin, Donna Strickland, and Gérard Mourou the physics Nobel prize in 2018, and the applications have included but are not limited to cell sorting[204,205], investigation of RNA and DNA mechanics[206], mechanical forces of protein folding and unfolding[207], DNA-protein interactions[208], microsurgery[24] and live *in vivo* cell manipulation[209]

An optical trap occurs when the optical forces are such that an object is held at the focus of a laser beam and can be moved by altering the position of the laser focus. Initially called single-beam gradient force trap, optical tweezers rely on a highly focused laser beam provided by an objective lens of high numerical aperture (NA) to produce an intensity profile forming an optical trap[21]. Most optical traps are produced using a Gaussian profile and rely on a refractive index mismatch between the object and surrounding media to provide an attractive or repulsive force. Optical tweezers can exert pico-Newton forces to physically hold and manipulate microscopic objects, such as single cells, in 3D at the focus of the laser beam. Using this technique researchers have been able to physically interact with biological matter at a single-cell scale[24,204].

1.5.2. Mechanisms and forces

The mechanisms underpinning optical tweezers can be categorised into two regimes; the first acting when the radius of the object of interest, a, is larger than the wavelength, λ, of the trapping laser ($a > \lambda$), and the second acting when the objects radius is smaller than the wavelength ($a < \lambda$). Under the first condition the optical trap can be described by the ray-optics regime, and the latter by the Rayleigh-scattering regime. However, as biological matter is usually of a greater radius than the wavelength of the trapping laser (where a cell is on average ≈ 10 nm - 20 μm in diameter and the wavelength of optical trapping lasers is commonly 800 nm - 1000 nm[21,210,211]), here we will be focusing on the ray-optics regime.

In order to achieve optical trapping, a microscope objective of high NA (typically >1) is used to focus the laser to a diffraction-limited focal spot. Within an optical trap a particle is commonly described to be affected by two main forces: the scattering force and the gradient force. The scattering force arises from the transfer of momentum from the photons hitting a particle propelling it in the direction of laser propagation. This scattering force is proportional to the intensity of the laser and within collimated laser systems, the scattering force is much greater than the gradient force so trapping cannot be achieved. However, upon tightly focussing the laser beam, an extremely high gradient in the electric field is generated near the beam waist. The gradient force is proportional to this intensity gradient of the laser and counteracts the scattering force, creating a focal spot with trapping forces capable of holding micron-sized particles in 3D[201,212].

For all regimes, the trapped object must have a refractive index different to that of the surrounding medium. If the ratio of the refractive index between the particle, n_1, and surrounding medium, n_2, is sufficiently large ($\frac{n_2}{n_1} > 1.01$)[213], diffraction effects can be neglected, and the main influence is the refraction of light through the particle. In a uniform medium with no change of refractive index, these rays propagate in a straight line, however upon interaction with a particle with a different refractive index to the surrounding medium, the rays are refracted in accordance with Snell's law:

$$n_1 sin\theta_1 = n_2 sin\theta_2 \qquad \text{Eq. 1}$$

where θ_1 is the incident angle of light propagation relative to the normal at the interface between the two materials of different refractive index, and θ_2 is the angle of refraction with respect to the normal (**Figure 1.4**).

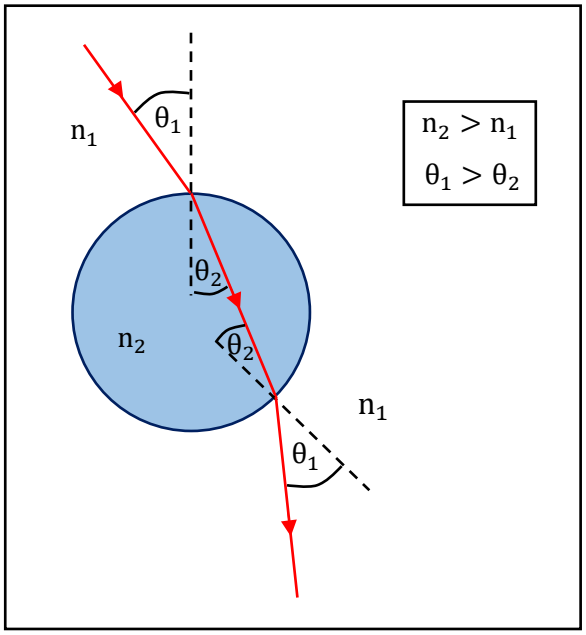


Figure 1.4: Schematic illustrating the refraction of light travelling from one medium, n_1, into a particle of higher refractive index, n_2, then returning into to surrounding medium, n_1.

As the laser radiation passes through the interfaces between the medium and the particle, the rays are refracted causing them to exit the particle with a different angle from which it entered. As momentum is defined as mass multiplied by velocity, which is a vector, this change in direction is therefore a change in velocity and is in turn a change in the momentum of the rays. Due to Newton's second and third laws the rate of change of momentum of the photons being refracted or scattered by the trapped particle results in a force on the particle that is equal in magnitude and opposite in sign to the change in momentum of the light (**Figure 1.5**). This force, F, can be given by the rate of change of momentum,

$$\vec{F} = -\frac{m\Delta\vec{v}}{\Delta t} \qquad \text{Eq. 2}$$

where m is mass of the particle, $\Delta\vec{v}$ is the change in velocity of light, and Δt is the change in time.

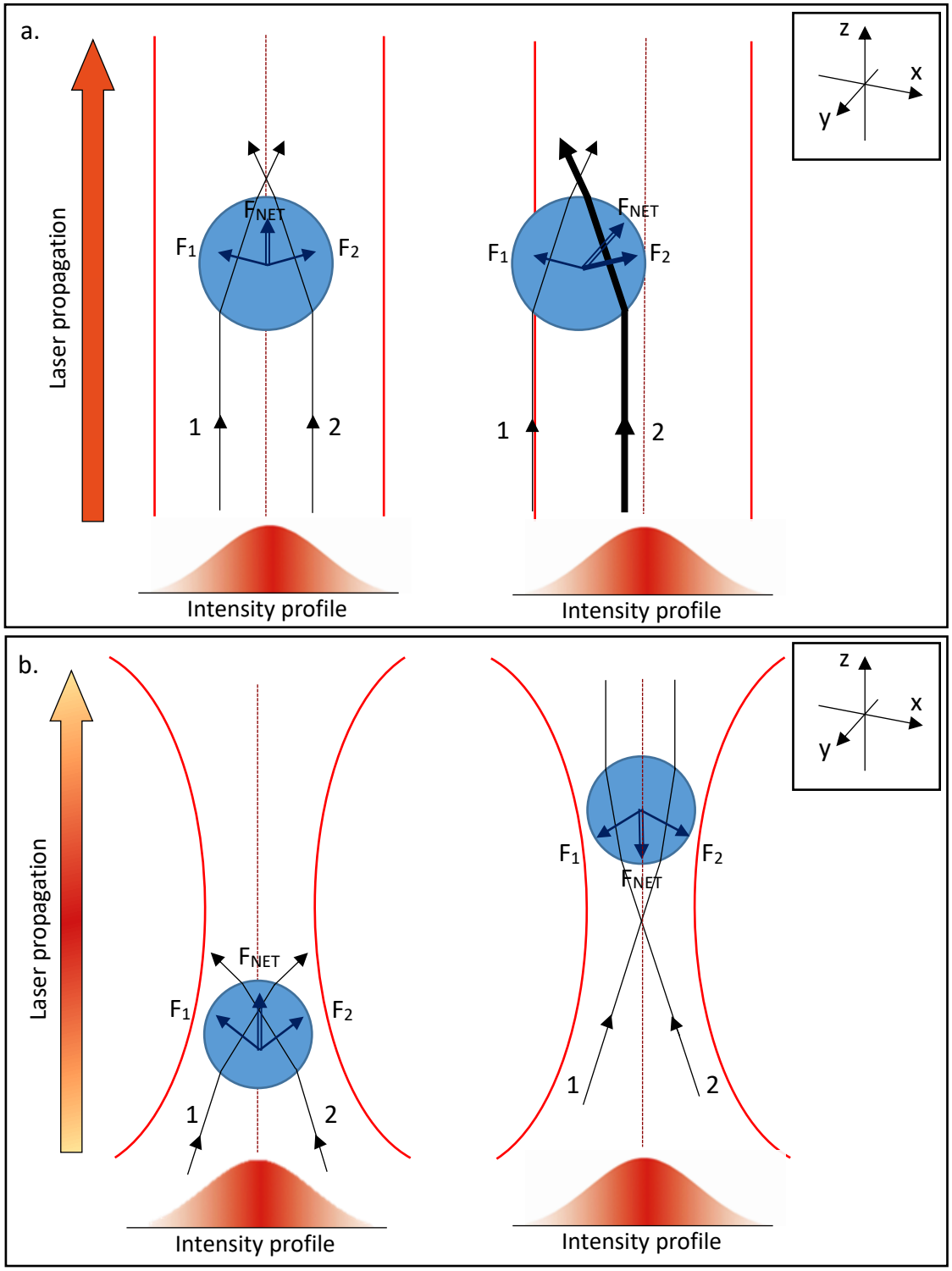


Figure 1.5: Ray optics explanation of optical trapping for a particle of higher refractive index than the surrounding medium. a. *In an unfocused laser when the particle is located at the centre of the laser beam, the resulting lateral force is zero. When the bead is displaced from the centre of the beam, the momentum change causes a net force to be applied back to the centre of the beam.* ***b.*** *Particle is in a focused beam. Gradient forces due to intensity gradient constrains the particle in the x and y directions as in* ***a.****, however the focusing of the beam also constrains the particle in the z direction (where z is the direction of beam propagation). The momentum change of the focused laser rays cause a reactive force towards the laser focus (beam waist), both when the particle lies in front of (left) and behind (right) the focus. At equilibrium, the particle will therefore reside slightly in front of the focus, due to contribution from the scattering force.*

1.5.3. Microrheology

Rheology encompasses the study of the viscous flow of liquids, the mechanical elastic response of solids, and the viscoelasticity of materials which encompass both viscous and elastic properties[214]. Traditionally, rheology is studied on a macroscopic or 'bulk' scale and has been used to quantify the mechanical properties of a wide range of materials used in everyday life (e.g. mattresses, hockey sticks), and biological materials such as hydrogels. The most common technique of performing bulk rheology is by using a rotational rheometer which quantify the mechanical properties of a material by relating the torque of rotation to the viscosity of the material of interest using a range of rotational frequencies. This method has successfully produced a library of comparable mechanical values of materials. However, bulk rheology does hold limitations. Primarily, this technique is limited by the scale it can analyse the materials which can lead to misleading interpretations when extrapolating to the micro-scale. Furthermore, within medical or biological research the amount of material required for bulk rheology (approximately 1 mL) which can be expensive or even impossible to obtain.

The technique of studying the mechanical properties of materials at the microscale, now termed microrheology, is predominately achieved by the tracking of tracer probes (typically beads) within the material of interest using optical tweezers. Microrheology operates on the same principles as used to bulk rheology, relating the frequency of motion (of the beads) to the viscoelastic properties. However, unlike bulk rheology which provides an average measurement for the whole sample, microrheology examines the mechanical properties at a scale relevant to the cell's microenvironment.

Aside from the obvious advantage of dealing with the scales of interest, a further advantage of microrheology over traditional bulk methods is that it only requires very small volumes of material (≈ 10 μL) which makes the application greatly more accessible to biological samples[214]. Additionally, unlike bulk methods, microrheology does not require contact and can be performed *in situ* providing the material of interest is within a suitable container. This means that

the measurement of viscosity does not need to be an end experiment and can be performed with viable cells and tissues.

With specific relevance to the work presented in this thesis, Manlio Tassieri from the University of Glasgow has made significant advancements to the field of microrheology; developing a technique that uses an optically trapped probe to measure the local mechanical properties and presenting novel experimental methods of collecting data and data analysis[214–218]. This project utilises this expertise and data analysis for investigation of the microrheological properties of the peptide gels and is discussed in **chapter 3.**

1.5.4. Biological applications of optical tweezers

For biological applications of optical tweezers, the additional complication arises of the potential damaging properties of laser radiation. For this reason, when biological matter is used, there is a biological window of laser wavelengths which can be considered to avoid unnecessary cellular damage. As the main component of mammalian cells is water (≈70 %) this biological window is based off the absorption spectra of water, which shows a dip between 800 nm to 1000 nm[17,219,220]. The choice of laser for this project was therefore chosen to be 1064 nm as this balanced the water absorption and allowed for the use of a reliable and inexpensive laser in comparison to lasers of lower wavelength. As cells have a relatively low absorption at 1064 nm, the potentially harmful properties of NIR radiation is limited to heat induction[17]. Using a 1064 nm laser, the localised heating has been shown to be negligible (0.8 K) at the focus of a 100 mW laser, scaling linearly with power over a range of 40 to 250 mW, increasing by 1.15 K for each further 100 mW[17,219,221].

Despite the complications involved, optical trapping techniques have developed to be widely applied as a tool for physically manipulating biological matter at a single cell scale[204]. Many of these applications rely on the use of optical tweezers in combination with other instruments. Most commonly optical tweezers are coupled with fluorescence or confocal microscopy to enable combined use of immunocytochemistry (ICC), real-time imaging, and single cell manipulation[222].

Due to their ability to physically confine living biological matter and measure the resultant pico-Newton forces at a cellular scale, optical tweezers have created the possibility of being able to manipulate and further characterise cell cultures in 3D. For this reason, much interest has been generated in the possibility of using optical tweezers to observe cellular behaviour in 3D culture systems, such as hydrogels. In light of this, a study in 2010 used optical tweezers to investigate the microstructural properties of hydrogels, investigating pore size and distribution in 3D hydrogels[223]. Using an optical tweezers based set up the team analysed the mean squared displacement (MSD) of 1, 2, and 4.7 μm diameter beads within a pore and observed the plateau as the time lag increases (frequency decreases). As hydrogels exhibit viscoelastic properties this plateau occurs due to the particle exhibiting a physical boundary (i.e. the edge of the pore). Complementary use of confocal imaging enabled tracking of the trajectories and mean-square displacements of beads suspended in the hydrogel, allowing for visualisation of the heterogeneous pore structure.

As optical tweezers can perform precise assembly of cellular microenvironments, studies have also demonstrated the ability to form complex architectures with sub-micron precision. In 2015, researchers used a polyethylene glycol (PEG) hydrogel system to ensure positional and pattern stability[17]. However, one of the issues the team faced was the instability of the cells once placed in the desired micro-architectures using holographic optical tweezers, resulting in the reorganisation of cellular orientations. They combated this loss of positional accuracy by using a rapid crosslinking method that force cell-cell adhesion for the first 24 h of culture, giving the cells time to stabilise within the designed patterns. Although this could be considered a large step towards optical trapping in hydrogels, they used optical trapping prior to crosslinking the gels, meaning they did not trap in viscous material; a challenge imperative to realising a technique to study or recapitulate *in vivo* cellular microenvironments.

Due to their suspended cell culture, blood cells are the most studied cell type for single-cell manipulation, however, there is surprisingly little research covering single cell-cell interactions of HSCs or LSCs. The most applicable study connecting optical manipulation and AML was published in 2015 which

characterised the initial interactions between leukaemic cell line Molm13, and stromal cell line M210B4[224]. Dong Sun et al. used optical traps to control the cell contact time between the two cell types and investigated the role of the stroma-secreted chemokine stromal-derived factor 1 (SDF-1) and its cognate receptor CXCR4 in leukaemia/bone marrow. The functions of the chemokine in cell-cell interactions were blocked by pre-treating the leukaemic cell with AMD3100, a widely used drug known to selectively block the signalling pathway involved in these processes[225]. Their results showed that the amount of adhesion molecules could affect cell contact within the first few minutes.

The same team also previously reported the use of optical tweezers combined with fluorescence microscopy to study cell-cell interaction via single adhesion manipulation[226]. Again, they used leukaemic and stromal cell lines and investigated the adhesion properties of the cells with and without added heparin. The team indicated that pre-treatment of K-562 cells with heparin reduces the adhesion ability of K-562 cells on the stromal cells, suggesting heparin inhibits some membrane proteins. However, these results were not statistically analysed for significance.

Since the start of this project, much research into biological or medical applications using optical tweezers has been conducted on red blood cells. Predominantly this has included using varying techniques of optical tweezer-based microrheology and exploring single-cell characteristics. However, it was recognised in 2020 by Zhu et al. that despite the great promise optical trapping techniques have shown for the study of blood cells, much is still left to be desired in order for this technique to support functional diagnosis and therapeutic development[227]. For example, current optical trapping techniques are restricted to 2D applications, limiting the ability to form a comprehensive understanding of 3D biological systems or materials[228]. Furthermore, although it has been greatly improved in recent years, the high-intensity lasers required for optical trapping can cause photodamage to biological samples, narrowing the applicability to optical trapping *in vivo* and to live cells *in vitro*[228–230].

1.6. Overall aims / hypothesis

The understanding of the bi-directional interactions of AML cells and the bone marrow niche, and identification of the underlying mechanisms of how the niche affects how AML responds to drug treatments, is imperative for improving therapeutic efficacy. To elucidate some of these underlying mechanisms of AML, this project uses a fully-defined peptide gel model for use as a 3D 'blank slate'. The peptide gel model contained no growth factors or matrix motifs, and enabled independent control over the physical stiffness and the chemical functionalisation of the model. The use of this model therefore provided a unique insight into the impact of 3D culture on leukaemic cell behaviours and response to drug treatment, with the long term aims of identifying potential therapeutic targets and developing the complexity of the models to replace the use of animal models in leukaemia research.

The overarching hypothesis of this thesis was therefore that the mechanical cues that establish 3D growth in peptide hydrogels influence drug sensitivity in leukaemic cells. This was divided into 3 sub-hypotheses explored in **chapters 3, 4, and 5,** respectively.

1) Optical tweezers can be used to investigate the peptide gel and leukaemic cells at the single-cell scale with minimal effect on the system.
2) The peptide gel supports the growth of leukaemic and haematopoietic cells.
3) The biomechanical properties of 3D growth in unmodified peptide hydrogel affects leukaemic cell response to drug treatment.

Each of these hypotheses aimed to address the unmet need of building an understanding of the importance of including mechanical cues in leukaemia models, developing from quantifying and assessing the physiological relevance of the mechanical cues the cells are exposed to in the peptide gel model, to an investigation of how the addition of a non-interacting 3D structure impacts drug efficacy. It is hoped that this information will inform the development of future 3D models for AML research, in addition to providing a novel platform for unravelling the complex interactions between the leukaemic cells and their niche for identification of potential druggable targets.

Chapter 2: Materials and methods

2.1. Optical trapping

Unless expressed otherwise, all optical trapping experiments were performed with a 1064 nm, 3 W, continuous wave laser (Ventus 1064, Laser Quantum Ltd., UK) operating at spatial Gaussian mode (TEM_{00}). Optical tweezer set-up and laser power calibration is presented in **chapter 3.**

2.1.1. Sample preparation of beads for optical trapping

A low concentration of 2 μm diameter polystyrene beads (≈1×10^5/ml) (19814 Polysciences) was produced by dilution in sterile water. For optical trapping the bead suspension seeded into either a chamber made from a single cavity microscope slide and coverslip (both provided by Thorlabs) sealed with clear nail varnish or within an Ibidi 8-well μ-slide (uncoated, 80821).

2.1.2. Sample preparation of cells for optical trapping

For optical trapping of cells within liquid culture, the cells were prepared to a low concentration (5×10^4/ml) within the relevant media and seeded into an Ibidi 8-well μ-slide. For cell viability analysis, Ethidium Homodimer-1 (Thermofisher Scientific, UK) was added at a 2 μL/mL concentration in PBS. The cell suspension was then protected from light and incubated at room temperature for 15 min as per manufacturers protocol before optical trapping.

For optical trapping of cells within peptide gels, the desired cells were seeded into an Ibidi 8-well μ-slide (uncoated, 80821) (see chapter sections **2.4** and **2.5** for peptide gel formation and seeding method). The cell-seeded peptide hydrogels were incubated at 37°C and 5 % CO_2 in a humidified atmosphere for at least 24 h prior to optical manipulation to ensure pH neutralisation by media perfusion. For observation of viability of the cells during optical manipulation Calcein AM (Thermofisher Scientific, UK) was prepared to a concentration of 0.5 μL/mL in PBS (Gibco, Life Technologies, USA). Excess media was aspirated from the peptide gels and the Calcein AM solution was added on top of the gel. The gels were protected from light and incubated at room temperature for 15 min before

imaging/manipulation, a timing chosen from in-house knowledge from the Stem Cell Glycobiology group at the University of Nottingham[231].

2.2. Microrheology

2.2.1. Water

The experimental set-up for microrheology was verified by taking control measurements of the viscosity of water. 500,000 frames were recorded at a frame rate of 600 fps using a laser power of <5 mW (at sample). LabVIEW programs provided and developed by Dr Manlio Tassieri (LabVIEW, 2013, National Instruments, USA) were used for (i) bead tracking, (ii) trajectory conversion to mean squared displacement, and (iii) for extracting the complex viscosity of the gel immediately surrounding the beads. The imaging and post-processing were completed in the same manner for all microrheology analysis.

2.2.2. Peptide hydrogel

The microrheological properties of both precursor and peptide gel were tested by measuring the Brownian motion of 2 μm diameter polystyrene beads (19814 Polysciences) embedded into the samples. For the precursor, beads were suspended at a final concentration of 2×10^5 beads/mL by incorporating them with the addition of 10× PBS. This relatively low bead concentration was chosen to avoid clustering and to ensure that only one bead was present in the field of view for the duration of the experiment. This was important for the centre of mass tracking to be reliable. After a standard overnight incubation at 80°C, precursor samples were equilibrated for 1 h at 37°C and 5 % CO_2 in a humidified atmosphere prior to transfer into an Ibidi 8-well μ-slide at 200 μL/well for testing. For the peptide gel (post-gelation), beads were added to the gel by suspension into the 250 μL of cell culture medium used for neutralisation, at a final concentration of 2×10^5 beads/mL. Peptide gels were seeded into an Ibidi 8-well μ-slide and incubated at 37°C and 5 % CO_2 in a humidified atmosphere overnight. The trajectories of 5 individual beads per condition were tracked using a centre of mass algorithm. For each bead at least 50,000 frames were recorded at a frame rate of 600 frames per second (exposure time 1500 μs). For some measurements, the

number of frames was limited by the bead diffusing out of the field of view. As the stiffness of the peptide gels is sensitive to temperature change for all optical measurements conducted with peptide gels the samples were kept incubated at 37°C and 5 % CO_2 in a humidified atmosphere for at least 24 h prior to performing experiments and the samples were left out of the incubator for the minimum time possible. The room where the optical trapping system was located was kept as warm as possible during measurements using an air conditioning unit kept at 30˚C. All samples were kept under sterile conditions during optical experiments by using a class II microbiological safety cabinet to prepare all samples and keeping the samples sealed within an optically supportive construct during experiments.

2.2.3. Matrigel

Corning Matrigel™ (354234 Fisher Scientific) was prepared to a polystyrene bead concentration of 2×10^5 beads/mL by incorporating 10 µL of beads suspended in RPMI-1640 (Gibco, Life Technologies, USA) to 200 µL of Matrigel™. Bead-seeded Matrigel™ was aliquoted into Ibidi 8-well µ-slide and incubated for 15 min at 37 °C and 5 % CO_2 in a humidified atmosphere. An equal volume of RPMI-1640 was added on top of the Matrigel™ to prevent dehydration and the samples were returned to the incubator overnight. Microrheological analysis was completed the following day by analysis of the trajectories of 3 individual beads in 3 separate wells (9 beads total). For each bead 200,000 frames were recorded at a frame rate of 600 fps (exposure time 1500 µs).

2.3. Cell culture

Culture of human and murine cells lines was conducted in a class II microbiology safety cabinet under aseptic conditions. All cells used were free of contamination with mycoplasma, and cell counts were determined using trypan blue dye exclusion (Roche Diagnostics, Switzerland) and a haemocytometer. Tissue culture grade plates and flasks (T25) (NUNC) were used for continuous culture.

Human leukaemic cell lines (THP-1, U937, MV411, HL60, and OCI-AML3) were maintained in suspension culture in RPMI-1640 supplemented with 10 %

fetal bovine serum (FBS), and 1 % L-Glutamine (All supplied by Gibco, Life Technologies, USA) and incubated at 37˚C and 5 % CO_2 in a humidified atmosphere. Cultures were passaged every 2-3 days to maintain a cell number of 1×10^5/mL to 1×10^6/mL.

For continuous culture of MLL-AF9 mouse primary leukaemic cells (mAF9) the cells were cultured in RPMI-1640 with additions of 10 % FBS (HyClone), 1 % L-Glutamine, 5 ng/mL mIL-3 (#130-099-508), 5 ng/mL mIL-6 (#130-096-682), 5 ng/mL mGM-CSF (#130-095-742), 50 ng/mL mSCF (130-101-693) (all growth factors purchased as premium grade from Miltenyl Biotec, UK). Phase contrast imaging was used to periodically observe cell growth (Eclipse TI-S (Nikon, Japan)).

Table 2.1: Media components for primary mouse leukaemia cell (mAF9) culture, where 0.5x and 1x relates to the growth factor concentrations.

Component	0.5x media	1x media
Basal media	RPMI-1640	RPMI-1640
FBS	10 %	10 %
L-Glutamine	2 mM	2 mM
mIL-3	5 ng/mL	10 ng/mL
mIL-6	5 ng/mL	10 ng/mL
mGM-CSF	5 ng/mL	10 ng/mL
SCF	50 ng/mL	100 ng/mL

Human Haematopoietic stem and progenitor cells (hHSPCs) (gifted by a PhD colleague, Emma Collins) were derived from induced pluripotent stem cells (iPSC, ReBL-PAT) using Stem Cell Technologies STEMdiff™ Hematopoietic Kit (Stem Cell Tech #05310, Canada) following the manufacturers protocol.

Table 2.2: Summary of cell types used in this study.

Cell type	Origin	Characteristics	References
THP-1	Peripheral blood of 1 year old infant with acute monocytic leukaemia (AML FAB M5)	Spontaneously immortalised monocytic-like cell line with a 9;11 translocation. Cultured in suspension with a large, round morphology capable of forming small loosely-packed cell clusters.	[232–236]
U937	Histiocytic lymphoma of a 37-year-old male	Pro-monocytic, human myeloid leukaemia cell line with a 10;11 translocation. Cultured in suspension with round, single-cell morphology.	[233,237,238]
MV411	10-year-old male with bi-phenotypic B myelomonocytic leukaemia	AML cell line with a 4;11 translocation. Cultured in suspension with rounded, single-cell morphology	[239,240]
HL60	Peripheral blood of a 36-year-old female with acute promyelocytic leukaemia	Among the first long-term populations of human myeloid leukaemic cells. HL60 cells are ovoid or round and cultured in suspension.	[237,241,242]
OCI-AML3	Peripheral blood of a 57-year-old male with acute myeloid leukaemia (AML FAB M4)	Single, mostly round cells culture in suspension.	[243]
mAF9	Primary murine cell line generated by retroviral transduction of MLL-AF9 into primary haematopoietic cells	AML primary mouse cells expressing MLL-AF9 fusion protein carrying a 9;11 chromosomal translocation. Cultured in suspension as an inhomogeneous population.	[141]
hHSPC	Human haematopoietic stem and progenitor cells derived by differentiation of iPSCs	Heterogenous population of HSPCs formed in suspension culture. Able to differentiate towards myelopoiesis or lymphopoiesis.	[244]

2.4. Peptide hydrogel preparation

Peptide (FEFEFKFK, Phe-Glu-Phe-Glu-Phe-Lys-Phe-Lys, Cambridge Research Biochemicals, UK/ Pepceuticals, UK)[245] at desired concentration was dissolved in sterile water (W3500, Sigma). Following incubation at 80˚C for 2 h, 0.5 M NaOH was used to elevate the hydrogel pH until an optically clear, self-supporting, viscous solution was formed. 10X phosphate buffered saline (PBS) (Gibco, Life Technologies, USA) was added to produce a final hydrogel of 1X PBS. Hydrogels were vortexed and centrifuged at 1000 rpm (Heraeus Megafuge 40R, Thermo Scientific, USA) after each addition to ensure a homogeneous composition. Following all additions, the hydrogels were incubated overnight at 80˚C then stored at 4˚C until required for cell encapsulation. For each experimental chapter in this thesis, a different batch of peptide gel was used (32597, 32896, and pepceuticals CMUN281019), for chapters 3, 4, and 5 respectively). All batches were analysed for similarity in rheological properties prior to use to ensure comparability of results.

2.5. Cell and bead encapsulation into unmodified peptide hydrogels

2.5.1. Human leukaemic cell lines

Hydrogels were incubated at 80˚C for at least 2 h prior to encapsulation to decrease viscosity then placed into a 37˚C water bath during cell preparation. Suspension cells were counted, re-suspended at required concentrations, and 250 µL was carefully mixed into 1 mL of hydrogel creating a media ratio of 1:5 and a final cell concentration of 1×10^4/mL – 1×10^5/mL. The cell-seeded peptide gels were then transferred into the required container (Ibidi 8-well µ-slide, transwells (Millicell Cell Culture Inserts, 24-well, PET 1 µm, Millipore), or 96-well plate (ViewPlate-96 Black, Perkin Elmer)) and incubated at 37˚C/5 % CO_2 in a humidified atmosphere for 10 minutes. Appropriate cell media was then added on top of the peptide gel and at least two media changes were performed in the following hour to allow the acidic nature of the media to reduce the pH of the hydrogel. Media changes were subsequently performed every 2-3 days.

2.5.2. Mouse primary leukaemic cells (mAF9)

Mouse mAF9 cells were seeded within unmodified peptide gels using the same method described **above** for human leukaemic cell lines. A range of final cell concentrations were used (5×10^4/mL – 5×10^5/mL) and media changes were performed with 0.5x media every 1-2 days.

2.5.3. iPSC-derived HPSCs

hHSPCs were differentiated and kindly donated by a PhD colleague, Emma Collins. Using a 12 day differentiation protocol from Stem Cell Technologies STEMdiff™ Hematopoietic Kit the ReBL-PAT iPSCs were cultured with STEMdiff™ Hematopoietic Supplement A during the first 3 days of culture to induce the RebL-PAT cell towards mesoderm, followed by a subsequent 9 days with STEMdiff™ Hematopoietic Supplement B to form haematopoietic progenitor cells. The differentiated cells were then seeded within peptide gels and their proliferation was observed using phase-contrast microscopy (**Figure 2.1**). The cells were seeded within the gel using a similar method as described in **chapter 2.5.1** to a final cell concentration of 5×10^4/mL. The cell-seeded hydrogels were maintained with Media B (provided with differentiation kit) and IMDM (Gibco, Life Technologies, USA) (supplemented with 10 % FBS and 1 % L-Glutamine) at a ratio of 1:1 and had a single media change on day 3 using the same media.

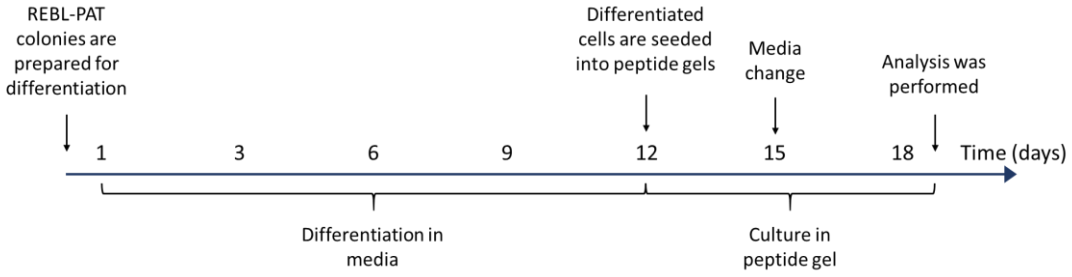


Figure 2.1: Timeline of differentiation and seeding of haematopoietic stem and progenitor cells in peptide gels.

2.5.4. U937 cell and polystyrene bead co-culture

For co-culture of live cells and 2 µm polystyrene beads (Polysciences. Inc, 19814, USA) hydrogels were prepared in the same manner as described in **chapter**

2.5.1. Prior to seeding, the beads were exposed to ultraviolet (UV) light for 1 h for sterilisation. U937 cells and beads were suspended in RPMI-1640 supplemented with 10 % (FBS), and 1 % L-Glutamine to produce a final concentration of 2.5×10^4/mL and 1×10^5/mL of U937 cells and beads, respectively. Subsequent media changes were performed every 2-3 days to ensure pH neutralisation of the peptide gel.

2.5.5. Functionalisation of 6 mg/mL peptide gel

For optimisation of mAF9 cell culture in peptide gels, modifications to the standard cell seeding protocol were explored. For conditions requiring changes of cell seeding number (conditions 1-3 **Table 4.1**), the appropriate cell number was determined using Trypan blue exclusion and incorporated using the method described in **chapter 2.5**. Condition 4 followed the same method as described above for production and seeding of the peptide gels, however the cell suspension and the subsequent media changes performed on the cell-seeded gels was performed with 1x mouse media (components described in **Table 2.1**). Modified peptide gels incorporating matrix additions of methylcellulose, (Methocult^{TM} GF M3434, Stemcell Technologies), laminin, (L2020, Sigma Aldrich); fibronectin, (07159, Stemcell Technologies); hyaluronan, (HA1M, Lifecore Biomedical)) were created by preparing a 250 µL volume of cell suspension containing each matrix component at 5x the desired final concentration (diluted with 0.5x leukaemic mouse media if required) and mixing with the 1 mL of precursor gel.

2.5.6. Immunocytochemistry (ICC) in peptide gels

Immunofluorescence staining of peptide gels was completed in Ibidi 8-well µ-slides. Media was removed from cell-seeded hydrogels and rinsed with PBS. The cells were then fixed in 4 % paraformeldrahyde/PBS for 1 h at ambient temperature. After 60 min block with PBST (0.1 % triton) containing 0.5 % BSA at ambient temperature, cell-seeded hydrogels were incubated overnight at 4˚C with primary antibody (vitronectin, 1:1000 (ABCAM, ab13413), fibronectin, 1:100 (ABCAM, ab2413), CD44, 1:400 (Cell Signalling Technology, 3570), Collagen I, 1:200, (ABCAM, ab34710), Collagen IV, 1:200, (ABCAM, ab6311), E-Cadherin, 1:100, (Cell Signalling Technology, 3195), Laminin, 1:100, (ABCAM, ab11575))

diluted in blocking buffer. Following this the cells were washed twice with blocking buffer, leaving the second wash on for 5 min. The hydrogels were then incubated for 2-3 h protected from light with secondary antibody (Goat anti-Mouse Alexa Fluor 488, 1:400, (Invitrogen, a11001), Goat anti-Rabbit Alexa Fluor 488, 1:400, (Invitrogen, a11008)) and phalloidin (1:1000, ThermoFisher Scientific, R415). Hydrogels were washed twice with blocking buffer, and DAPI (dilactate, ThermoFisher Scientific) was added for 30 min at ambient temperature to stain cell nuclei. Hydrogels were washed with PBS and imaged as required. For staining the hydrogel cultures in transwells the same method was followed, however, after fixation the hydrogels were carefully removed from the transwells using a scalpel and transferred to an Ibidi 8-well µ-slide for staining. Confocal images (SPEII, Leica, Germany) were post-processed with Fiji image analysis software[246].

2.6. Cell quantification using luminescence

Luminescence assays RealTime-Glo™ MT Cell Viability Assay (RTG) and CellTiter-Glo® Luminescent Cell Viability Assay (CTG) (both Promega, UK) were used quantify the number of cells within liquid culture and 3D peptide gel. For all assays that required analysis by plate reader Fluorestar Omega Plate Reader (BMG LabTech), samples were prepared within black 96-well plates with optically clear bottom to minimise background and bleed-through between wells. For all results collected using luminescence assays, 'no cell' controls were performed to record any background fluorescence which was averaged and reduced from the results.

For analysis within liquid culture with RTG, RTG components were added to U937 cell to produce a final suspension with 1x RTG substrate stock and 1x nanoluc enzyme stock as according to the manufacturers protocol. Using this method, a range of cell concentrations (3.125×10^5/mL $-$ 5×10^6/mL) was produced. Plates were protected from light and incubated at 37˚C and 5 % CO_2 in a humidified atmosphere for 30 min before luminescence plate read.

For analysis of cell-seeded peptide gels with RTG, the gels were prepared and seeded with U937 cells (see **chapters 2.4** and **2.5**). 100 µL of cell-seeded gel was transferred to wells of a black 96 well plate in triplicate of each condition.

Following the 2 required media changes after initial seeding of the plates, all media was removed and 100 µL of 2x RTG components diluted in media was added to produce a final concentration of 1x RTG (media and gel volume inclusive). The plates were protected from light and incubated at 37˚C and 5 % CO_2 in a humidified atmosphere for 1 h before luminescence plate read.

For analysis of liquid culture with CTG the assay was added directly to the cell suspensions in the 96 well plate at a 1:1 ratio to a total volume of 200 µL. The plate was protected from light and incubated at room temperature for 30 min prior to quantification by plate reader (as suggested by the manufacturer).

CTG assay within peptide gels was performed by preparing the cells in the same manner as described for RTG, and was directly added to the cell-seeded peptide gel at a 1:1 ratio to a total volume of 200 µL (gel and media inclusive per well). Plates were protected from light and incubated at 37˚C and 5 % CO_2 in a humidified atmosphere for 1 h before luminescence plate read.

All values were obtained in technical triplicates and were represented as a standard curve of known cell number against luminescence.

2.7. Drug screening

Drug screening of FDA-approved drugs used for other medical conditions was performed with the purpose of understanding their efficacy in leukaemia in 2D and 3D peptide gel models. This included salinomycin (sal) (Sigma Aldrich, UK), vidofludimus (vido) (SelleckChem, Germany), NB598 (MedChemExpress, USA), and atorvastatin (atorva) (SelleckChem, Germany). Human leukaemic cell lines and mAF9 cells were treated with a dose range of each candidate drug (diluted using serial dilutions), (sal, vido; final concentrations of 0.1 µM - 10 µM, NB598, atorva; final concentrations of 0.5 µM – 50 µM). All drug dilutions were made up from a high concentration stock (>10 mM) and kept for no longer than 24 h before use. Drug treatments were compared to the vehicle control (DMSO) at a concentration equal to the highest DMSO concentration within the drug dilutions. Graphing and analysis were performed using Prism 8.3.1 statistical software (Graphpad).

2.7.1. Liquid culture

For drug screening in liquid culture the cells were prepared in standard cell culture media with RTG to a final reagent concentration of 1x and a final cell concentration of 5×10^4/mL. The prepared drug concentrations (and DSMO vehicle control) at 2x desired final concentration were added to the cell suspension in a black 96 well plate at a ratio of 1:1 (in triplicate). Sterile water was added to all external wells of each plate to ensure minimisation of sample evaporation. The plates were protected from light and incubated at 37˚C and 5 % CO_2 in a humidified atmosphere. Luminescence plate reads were performed at 24 h, 48 h, and 72 h.

2.7.1.1. CellTox™ Green

CellTox™ Green Cytotoxicity Assay measures cell death by binding a fluorescent dye to the DNA of cells with damages membrane integrity. In accordance with the manufacturers protocol the CellTox™ Green dye provided in the assay was added to appropriate cell media to a final concentration of 1:1000. Following 72 h of incubation with relevant drug concentration within a 96 well plate, fluorescence and white-light images were taken using a confocal microscope. Images were post-processed using Fiji image analysis software.

2.7.2. Peptide gel

2.7.2.1. ‘Early stage’ AML model

6 mg/mL peptide gels were prepared as described in **chapter 2.4** and incubated at 80˚C for 2 h to decrease viscosity to aid homogeneous cell mixing, followed by 37˚C during cell suspension preparation. The cells were prepared to a concentration of 5×10^5/mL and added to the peptide gel at a ratio of 1:5, producing a final cell concentration of 1×10^5/mL. Following a 10 min incubation, 200 µL of cell line relevant media was added on top of the gel and media changes were performed by removing and adding 100 µL of media to reduce the risk of aspirating any cell-seeded gel. Following two media changes within the hour after seeding, 100 µL of media with RTG and the required drug/DMSO control (all added at 3x desired final concentration to be diluted within the 300 µL volume of gel and media) was added to the peptide gel. The plates were then protected from light

and incubated at 37˚C with 5 % CO_2 in a humidified atmosphere. Luminescence plate reads were performed at 24 h, 48 h, and 72 h.

2.7.2.2. **'Established' AML model**

Drug testing on 'established' peptide gel models was completed in a similar manner to the 'early-stage' AML models described above. Converse to the above protocol the 'established' models were cultured without addition of RTG or FDA-approved drugs for 72 h. During this culture period, the samples were kept at 37˚C with 5 % CO_2 in a humidified atmosphere and an additional media change with human leukaemic cell line media was performed at 24 h. At 72 h the RTG and required drug concentrations were added in the same way as described for the 'early-stage' model. The plates were protected from light and incubated for a further 72 h taking luminescence plate reads every 24 h.

Chapter 3: Establishing optical manipulation techniques in 3D peptide gel models for quantitative cell and matrix analysis

3.1. Introduction and aims

Optical tweezers as a non-invasive, 3D, manipulation tool have played an important role in promoting multidisciplinary technology for the advancement of medical research. This chapter explores the ability to use an optical trapping system to examine the microscale properties of the self-assembling peptide hydrogel used to develop 3D AML models, using water and Matrigel™ as controls.

This was completed with the aim of establishing a technique with which the rheological information of a material can be quantified at a cellular-relevant scale. This information in combination with the knowledge of the stiffness properties of *in vivo* bone marrow as determined by previous literature then informed the production of our peptide gel to produce a physiologically relevant 3D model. To achieve this, the optical trapping system was calibrated and quantification of Brownian motion was demonstrated to a nanoscale precision, producing novel, published results of the microrheological properties of the peptide gel[231].

Furthermore, cell manipulation was performed using optical tweezers with the aim of investigating potential differences in interactions forces. As mentioned above, there are limited differences between haematopoietic and leukaemic cell and niche behaviours, therefore there are minimal targets for producing leukaemia-specific therapies. The successful application of this technique in a physically relevant microenvironment would create a new method for identifying potential leukaemia-specific characteristics with the aim of informing future selective therapies.

3.2. Set-up and calibration of the optical trapping system

The optical trapping system used through-out this research comprised a near-infrared wavelength (λ = 1064 nm) continuous wave laser (Ventus 1064, 3 W,

Laser Quantum Ltd, UK) operating a spatial Gaussian mode (TEM_{00}). The system incorporated a Nikon Eclipse Ti-S inverted fluorescence microscope with a 100x oil immersion objective lens of high numerical aperture (Nikon, CFI Plan Apochromat λ, 100x oil, numerical aperture (NA) = 1.45, working distance (WD) = 0.13 mm), and a high precision, software-controlled sample stage (Applied Scientific Instruments, USA). Images and videos were captured using a QImaging optiMOS Scientific CMOS camera and Micro-Manager software or a Dalsa Genie Gig Vision™ camera and an in-house LabVIEW program. All optical trapping components, including the fluorescence microscope, were mounted and secured on a vibration isolated optical table (ThorLabs, PTR52504) and the laser beam path was kept horizontal at a height of approximately 10 cm from the surface of the table (with exception of the periscope to the back aperture of the microscope) (**Figure 3.1**).

To produce the optical tweezing system, the laser was fed through a beam expander, labelled in **Figure 3.1a** as lenses L1 and L2, where the focal distances (f1 and f2) are 60 mm and 250 mm, respectively. The distance separating this pair of lenses was equal to the sum of their focal distances (i.e. L1 to L2 = f1 + f2), therefore expanding the beam by a factor of $\frac{f2}{f1} \approx 4.17$, producing a laser diameter of ≈9.8 mm. The expanded beam was reflected by the SLM into lenses, L3 and L4 (focal lengths 750 mm and 1000 mm respectively). Lenses L3 and L4 were separated by a distance equal to f3+f4, where the spatial light modulator (SLM) is the distance f3 from lens, L3, and the distance L4 to the back of the microscope objective is equal to the focal length f4. The final size of the beam following expansion by lenses L3 and L4 was therefore ≈ 13.0 mm in diameter. This creates a 4f imaging system which are widely used within imaging systems as they enable accurate reconstruction of the optical field[247,248].

The liquid crystal based SLM consisted of 512x512 individually addressable pixels, each capable of modulating the phase and intensity of the light to produce multiple focal points, and therefore multiple optical traps. The SLM was used in **chapter 3.6.3** to explore the benefits of using multiple focal spots for live cells, however, for all single-focal spot optical trapping experiments discussed within

this thesis the SLM was switched off and acted as a mirror. This produced extra power loss compared to a standard mirror which is acknowledged in future calculations of laser power.

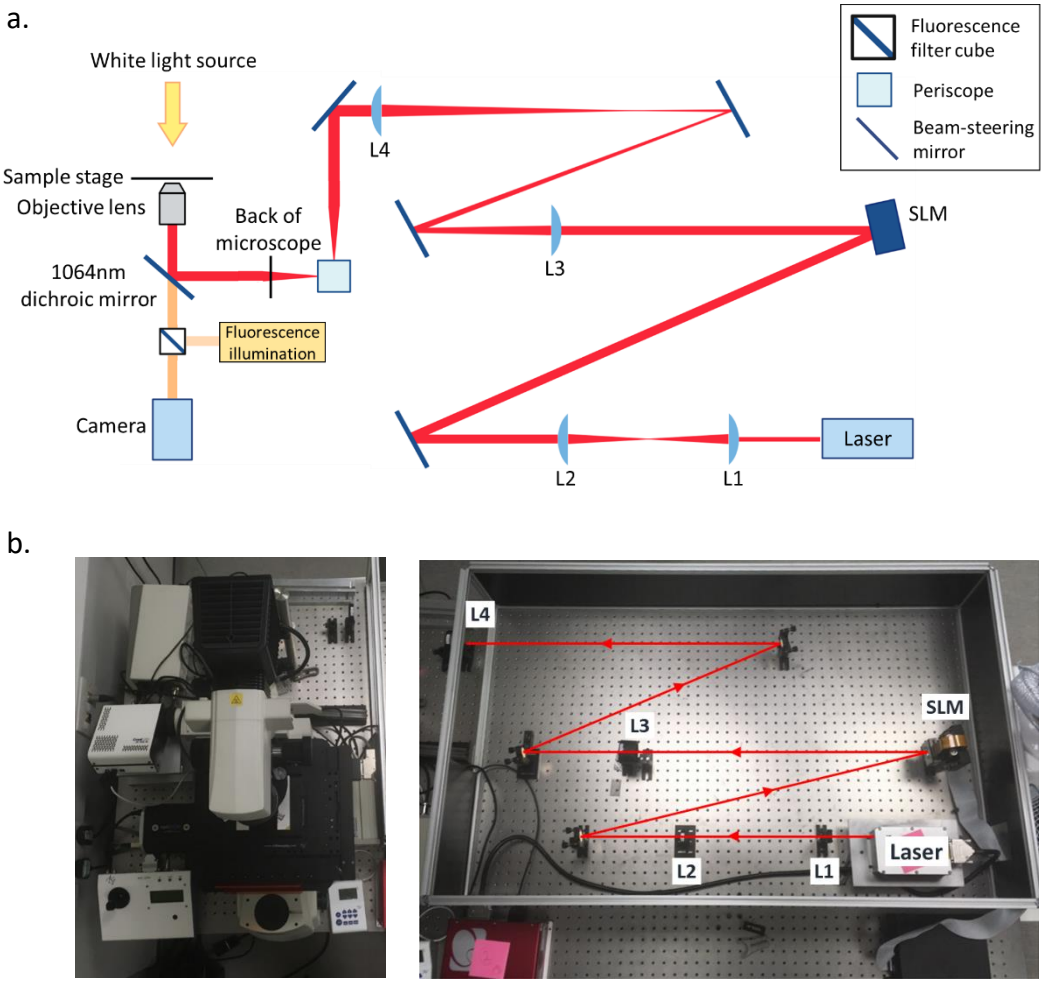


***Figure 3.1**: **Optical tweezers set-up. a.** Schematic diagram of the optical trapping system including the spatial light modulator (SLM) and indicating the focal points of the laser, where the distance between L1-L2 and L3-L4 is equal to the sum of their focal lengths. L stands for lens and the dimensions are not to scale. Created with BioRender.com. **b.** Photographs of the optical trapping system showing the laser path.*

The beam was then led through the periscope to bring the laser beam to the back of the microscope. Within the microscope, a dichroic mirror reflected wavelengths above approximately 700 nm, therefore reflecting the optical trapping laser (1064 nm) at a 45° angle into the objective lens (**Figure 3.2**). The expanded and collimated beam overfilled the back aperture of the objective lens

to ensure the high NA lens could perform optical trapping. The white light illumination (provided by a halogen lamp with a connected condenser) and fluorescence illumination (supplied by a controllable LED illumination unit (pE-300^{white}, CoolLED)) were transmitted by the dichroic mirror allowing for simultaneous optical trapping and fluorescence imaging. A quad band florescence filter cube (Semrock, DA/FI/TR/Cy5-A-000) comprised an exciter filter, an emission filter, and a dielectric mirror and was used to reflect required excitation wavelengths and transmit the emission wavelengths of the fluorescent dyes. A 1064 nm blocking filter was positioned after the filter cube to block any additional transmitted 1064 nm light from the camera.

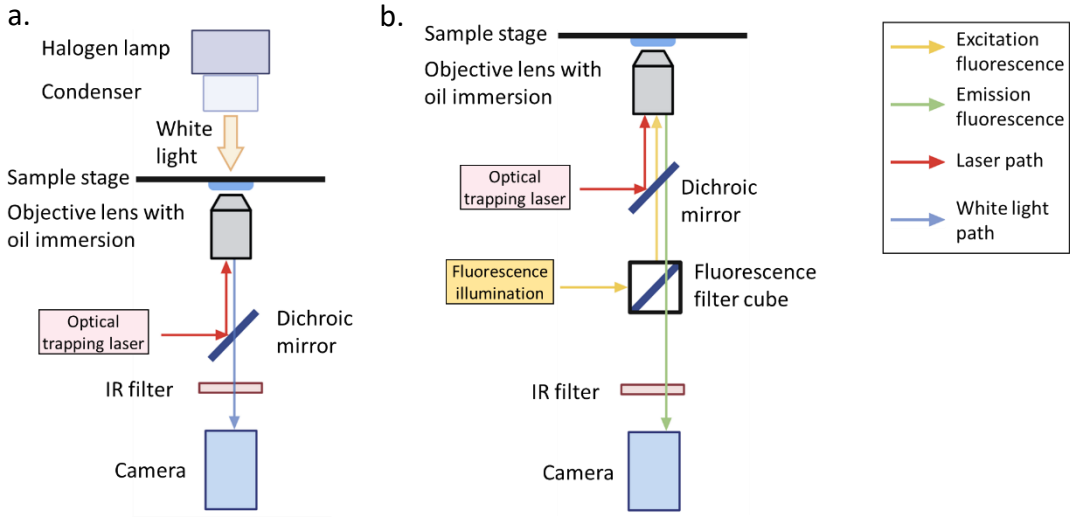


Figure 3.2: Schematic showing the light paths through the inverted microscope. *Schematics show the direction of light from the source to the sample when imaging with* ***a.*** *white light or* ***b.*** *fluorescence. Created with BioRender.com.*

3.3. Calibration of optical trapping power

The laser power supply (mpc6000, Laser Quantum Ltd, UK) enabled manual control over the intensity of the laser as a function of current percentage applied to the laser diodes. As the output from the laser may not vary linearly with diode current, a calibration was completed using a power meter fixed within the laser path. The power meter was placed immediately after the beam expander

produced with lenses L1 and L2. The future power values measured at this point will be defined as “in the laser path”.

A comparison of power readings taken after L2 to just before the objective lens was made to observe the power loss through the optical system. As can be seen from **Figure 3.3**, the power loss was constant within 3 % across the range of powers tested. The power loss was therefore averaged across 5 repeats to give a mean power loss of 58.2 (± 1.5) % through the optical system across the range of laser powers tested.

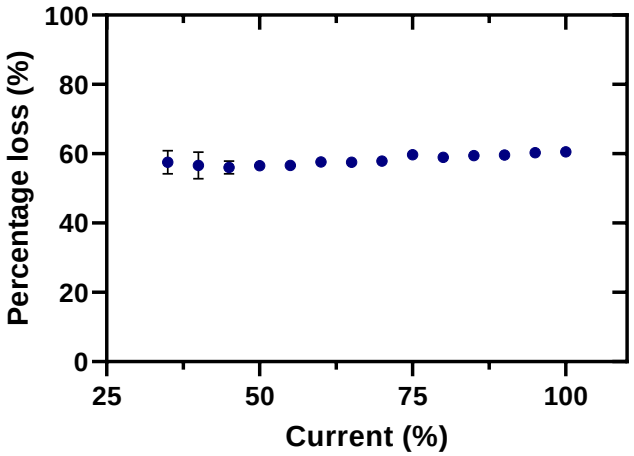


Figure 3.3: Comparative power measurements from within the laser path to the back of the objective lens. *Results shown are an average of 5 repeats with ± standard deviation for each data point. A mean of 58.2 (± 1.5) % power loss was seen between the laser after lens L2 and at the back of the objective lens.*

Based upon transmission graphs provided by the Nikon (**Figure 3.4**), the provider of the objective lens, an additional 28 % power loss occurs through the objective lens when using a laser of wavelength 1000 nm[249]. Therefore, accounting for the losses through the optical system and through the objective lens, the final laser power reaching the sample will be ≈ 30 % of the values measured in the laser path.

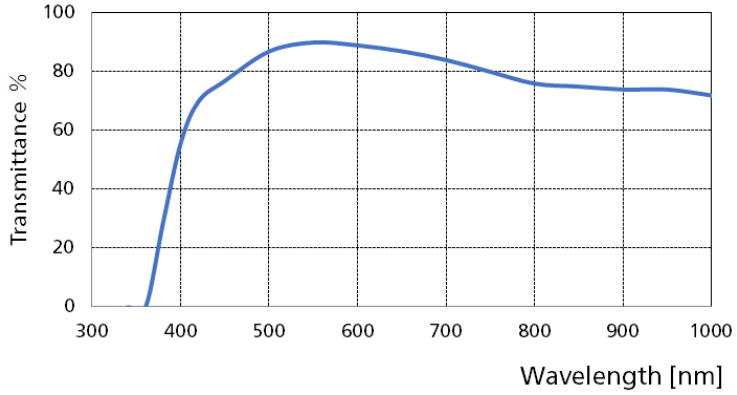


Figure 3.4: Transmittance graphs for Nikon CFI Plan Apochromat Lambda 100x oil objective lens[249].

Although a different laser was used for future trapping experiments due to malfunction, the laser was produced by the same manufacturer and was used within the same configuration with the same lenses and SLM so the losses can be assumed to be comparable.

To correlate the percentage of laser diode current to the power experienced at the sample, power measurements from within the laser path were taken in triplicate for increasing current values (**Figure 3.5**). For each repeat the laser was turned on for ≈ 5 min before collecting results to ensure it had reached equilibrium, and between each repeat the laser was turned off for the same time period to avoid the laser overheating. The results in **Figure 3.5** show a near proportional relationship at lower powers (up to ≈ 900 mW) then displaying a slight curve at higher powers. This could be due to thermal effects affecting photon generation.

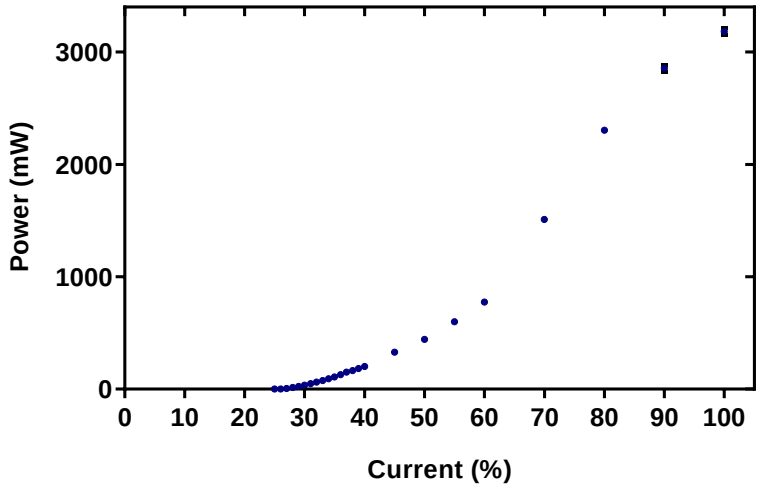


Figure 3.5: Percentage current (%) against laser power (mW) for Ventus IR 1064 nm laser. *Laser powers recorded with power meter secured just after lens L2. Error bars calculated on each data point as standard deviation of 3 repeats. Due to losses in the system and through the objective lens the power exposed to the sample will be ≈ 30 % of the values shown here.*

3.4. Quantification of optical trapping strength using equipartition theorem

The dynamics of an optically trapped bead can be modelled as a damped harmonic oscillator, where the restoring force is generated by the optical trap and the damping force is provided by the surrounding material. The force acting on the trapped bead is proportional to the displacement of the bead from its equilibrium position, and therefore the trapping force of the laser can be modelled as the restoring force in Hooke's law, i.e. the further the weight/bead is moved from equilibrium the stronger the restoring force pulling the weight/bead back to its equilibrium position. For both the optical trap and a weight on a spring this only applies for small displacements (≈ < $0.8a$ where a is the bead radius[217]). The optical trapping strength is related to the displacement of the bead from equilibrium by,

$$\vec{\vec{F}}(t) = -\kappa\vec{r}(t) \qquad \text{Eq. 3}$$

where F is the optical trapping force, κ is the optical trapping strength (or stiffness), and r is the displacement of the bead with respect to the trap centre.

The optical trapping stiffness (also known as optical trapping strength) can be calibrated using the equipartition theorem. This method quantifies the variance of bead displacement in the x and y axes as caused by random thermal fluctuations driven by the fluids molecules, known as Brownian motion[215]. The equipartition theory of energy states that the harmonic potential energy produced by the optical trap can be equated to the thermal energy in the system to give,

$$\frac{1}{2}k_B T = \frac{1}{2}\kappa\langle\vec{r}^2\rangle \qquad \text{Eq. 4}$$

where k_B is the Boltzmann constant, T is the temperature in Kelvin, and $\langle\vec{r}^2\rangle$ is the variance in the displacement of the bead from the equilibrium position of the trap (in the x or y axis). By rearranging this equation, the optical trap strength can be calculated using,

$$\kappa = \frac{k_B T}{\langle\vec{r}^2\rangle} \qquad \text{Eq. 5}$$

It is important to note that this method of quantifying the trap strength is independent of both the viscoelasticity of the surrounding medium and the particle size.

Using this technique, the optical trapping strength of a 2 µm polystyrene bead in water was collected for a wide range of laser powers in both the x and y axes. Plotting this data demonstrated the linear relationship between trap strength and power (**Figure 3.6a)**. It is worth noting that despite how clearly the data points fit the linear relationship as shown by the trendline, values particularly above ≈ 150 mW exhibit sizable error bars. This could be due to trying to track position of the bead when the displacement has become very small, resulting in a large uncertainty. It could also be in small part due depth of the bead into the surrounding material (water). Although minimal over the observation depth used, increased depth into the sample increases spherical aberration and could reduce the trapping strength. All efforts were made to keep the z-axis depth consistent at ≈ 30 µm and the same distance away from all edges of the coverslip to ensure no edge effects as according to Faxen's law, nonetheless the slight difference in

depths between different beads could introduce some errors. Also, as these results came from different beads, although any differences between beads are minimal, there could be some variability of refractive index and bead size (varying between 1.80 µm and 2.20 µm according to the manufacturer), which would introduce variation into the results.

To visualise this increasing trapping strength, the mean displacement of the bead's movement in the x and y-axis was plotted against increasing laser power, highlighting the $\frac{1}{r^2}$ relationship between the average displacement of a trapped bead and trapping power as predicted by **Eq. 5** (**Figure 3.6b)**.

The reduction of the beads displacement from equilibrium with increasing laser power can also be seen visually in **Figure 3.6c** which shows scatterplots of x and y displacement. Within these scatterplots each point represents the location of the bead in the x and y axes for one frame. In order to quantify and analyse the positional information of the bead, a centre of mass algorithm was used. As concisely described by McAlinden et al.[20], calculating the centre of mass of an image along a single axis can be completed using,

$$C_x = \frac{\sum_{i=1}^{m}\sum_{j=1}^{n}(x_i I_{ij})}{\sum_{i=1}^{m}\sum_{j=1}^{n}(I_{ij})} \qquad \text{Eq. 6}$$

where I_{ij} is a matrix of image pixel density.

This process is optimised for homogeneous, uniform particle on a dark background. For this reason, a threshold is usually applied to the greyscale image or video to produce a white, bright bead against a black background. This is easily applied for uniform objects; however, it can introduce complications when applied to inhomogeneous object such as cells. This is discussed further in **chapter 3.6.3**.

The trapping strength in x and y axes should be approximately equal, however, this is dependent upon the shape of the focal spot and how symmetrical it is in x and y. Due to linear polarization of the laser beam along with circularly asymmetric aberrations like coma and astigmatism, the focal spot of the laser can take on an elongated, elliptical shape producing asymmetry in the resultant trapping strengths[250]. As can be seen in **Figure 3.6a**, there was a slightly stronger

trapping strength observed in the y-axis as compared to the x-axis, with an average y axis trapping strength ≈ 17 % greater than in the x-axis. This was also observed in **Figure 3.6c** (5 mW scatterplot in particular) whereby the scatterplot appears slightly oval with a narrower diameter in the y-axis.

The histograms accompanying the scatterplots in **Figure 3.6c** display the frequency of a specific bead displacement from equilibrium for both axes, showing the Gaussian distribution of laser power as expected from the single optical trap.

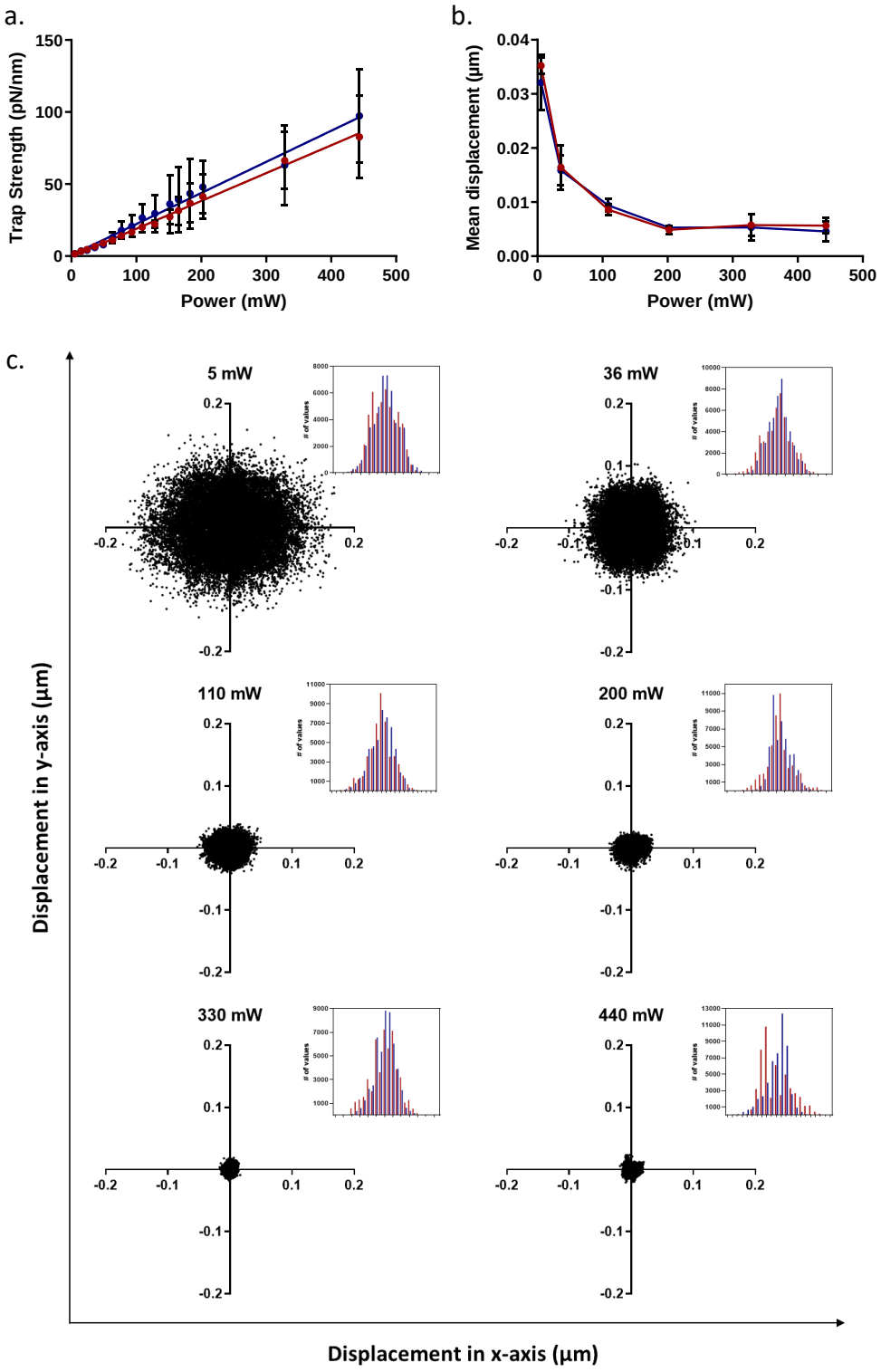


Figure 3.6: Quantification of bead displacement and laser trapping strength in water with a single optical trap. *Laser powers stated were measured in the laser path after lens, L2. For all graphs, the red and blue lines show data in the x and y axes respectively and the error bars were calculated as standard deviation of 3 repeats.* ***a.*** *Optical trapping strength calibration (pN/nm) with power (mW) of an optically trapped 2 µm polystyrene bead (N=3).* ***b.*** *Mean displacement of an optically trapped 2 µm polystyrene bead from equilibrium with a single focal spot of increasing power. (N=3).* ***c.*** *Scatterplots demonstrating the decrease of displacement from equilibrium and corresponding histograms with increasing laser power.*

3.5. Development of Brownian motion based microrheology

This section employs the technique of microrheology using the optical trapping system described above to confine and measure the Brownian motion of a bead or "probe". By precisely analysing the frequency components of this Brownian motion in combination with a LabVIEW program developed and kindly shared by Dr. Manlio Tassieri, viscoelastic properties of the material in which the beads are immersed can be quantified[216,251].

Microrheological techniques can be passive or active, based upon whether the object of focus (probe) is freely moving under Brownian motion or if it is subjected to an external force (e.g. optical tweezers)[214,252]. In this thesis, passive microrheology is defined as the movement of a bead or probe acting purely under thermal fluctuations (Brownian motion) and active microrheology as a probe experiencing an external force (i.e. optically trapped). Contrary to some techniques of active microrheology whereby the probe is optically trapped and moved with displacements significantly larger than the thermal fluctuations[215], here an optical trap is utilised primarily for holding the probe within the region of interest.

3.5.1. Theoretical background

The viscoelastic properties of a material can be described in terms of its complex modulus, $G^*(\omega)$[215,253],

$$|G^*(\omega)| = |G'(\omega) + iG''(\omega)| \\ = [(G'(\omega))^2 + (G''(\omega))^2]^{\frac{1}{2}} \quad \text{Eq. 7}$$

where ω is the angular frequency.

The complex modulus describes the overall resistance to deformation of a material and is made up of a real component, $G'(\omega)$, called the storage modulus which describes the elastic (solid-like) properties of the material, and an imaginary component, $G''(\omega)$, called the loss modulus which encompasses the viscous (liquid-like) properties.

The complex viscosity is defined as the complex modulus as a function of angular frequency and can be expressed in a similar manner,

$$\begin{aligned} |\eta^*(\omega)| &= |\eta'(\omega) + i\eta''(\omega)| \\ &= [(\eta'(\omega))^2 + (\eta''(\omega))^2]^{\frac{1}{2}} \\ &= \frac{|G^*(\omega)|}{\omega} \\ &= \frac{[(G'(\omega))^2 + (G''(\omega))^2]^{1/2}}{\omega} \end{aligned} \quad \text{Eq. 8}$$

where, similarly to the complex modulus, the complex viscosity encompasses the viscous properties through a real component, $\eta'(\omega)$, and elastic properties through an imaginary component, $i\eta''(\omega)$.

When a microscale bead is suspended within a medium at thermal equilibrium, it undergoes Brownian motion. As demonstrated by Mason and Weitz in 1995, analysis of the Brownian motion of the bead can determine the viscoelastic properties of the surrounding material[254]. Based on this pioneering work, in 2012 Tassieri et al. published an analytical model for extracting the viscoelastic properties of a complex fluid via analysis of the mean squared displacement (MSD) of a microscale probe[216], a technique used for this study. The time-dependant MSD is defined as,

$$\langle \Delta r^2(\tau) \rangle = \langle [\vec{r}(t+\tau) - \vec{r}(t)]^2 \rangle_t \quad \text{Eq. 9}$$

where t is the absolute time and τ is the lag time (i.e the time interval between frames).

For both passive and active microrheology, the relationship between the MSD of the bead and the viscoelastic properties of the surrounding medium can be determined by solving a generalised Langevian equation. For passive microrheology (i.e. no trapping laser) this is given by,

$$m\vec{a}(t) = \overrightarrow{f_R}(t) - \int_0^t \varepsilon\,(t-\tau)\vec{v}(\tau)\,d\tau \quad \text{Eq. 10}$$

where m is the mass of the bead, $\vec{a}(t)$ the acceleration of the bead, and $\vec{v}(\tau)$ the velocity of the bead. The $\overrightarrow{f_R}(t)$ term is Gaussian white noise (i.e. the thermal forces acting on the bead), and the integral includes the generalised time-dependent memory function, $\varepsilon(t)$, which represents the dampening caused by the viscoelastic properties of the surrounding material, i.e. the term of interest for microrheological research. Following Mason and Weitz et al[254], this term can be related to the complex modulus via its Fourier transform $\hat{\varepsilon}(\omega) = 6\pi a G^*(\omega)/i\omega$. Where $\hat{\varepsilon}(\omega)$ is the Fourier transform of $\varepsilon(t)$. The complex modulus can therefore be written in terms of the MSD of a bead,

$$|G^*(\omega)| = \frac{1}{6\pi a}\left[\frac{6k_B T}{i\omega\langle\Delta\vec{r}^2(\omega)\rangle} + m\omega^2\right] \qquad \text{Eq. 11}$$

For active microrheology (i.e. static optical trap). The relationship between the MSD and the complex modulus are derived in a similar manner, with an additional term added for trapping force. Therefore, for active microrheology the generalised Langevian equation becomes,

$$m\vec{a}(t) = \overrightarrow{f_R}(t) - \int_0^t \varepsilon\,(t-\tau)\vec{v}(\tau)\,d\tau - \kappa\vec{r}(t) \qquad \text{Eq. 12}$$

where $\kappa\vec{r}(t)$ is the additional term to **Eq. 10** accounting for the trapping force. The complex modulus for active microrheology can therefore be given in terms of the MSD as,

$$|G^*(\omega)| = \frac{\kappa}{6\pi a}\left[\frac{1}{i\omega\widehat{\Pi}(\omega)} - 1\right] \qquad \text{Eq. 13}$$

where $\widehat{\Pi}(\omega)$ is the Fourier transform of the normalised MSD defined as,

$$\Pi(\tau) = \frac{\langle\Delta r^2(\tau)\rangle}{2\langle r^2\rangle} \qquad \text{Eq. 14}$$

$\Pi(\tau)$ is a dimensionless term that is equal to 1 over long time intervals (low frequencies)[217]. For **Eq. 13** defining $G^*(\omega)$, the $m\omega^2$ term has been neglected as for micron-sized beads, $m\omega^2$ only becomes significant at frequencies of the order

of MHz[215]. Due to the limitations imposed by the camera and imaging system, we explored up to a maximum of 1 kHz deeming this term unnecessary.

Within the equations relating to the MSD and microrheological data (**Eq. 9** to **Eq. 14**), brackets 〈…〉 indicate a measurement is averaged over all time, meaning the values collected only become exact when the measurement time is infinity[255]. Experimentally this was explored by analysing the optical trapping strength measurements and associated uncertainty with the number of frames recorded. **Figure 3.7** shows that following 50,000 frames the trapping strength begins to stabilise, producing a value within 10 % of the trapping strength after 500,000 frames. Following 50,000 frames the error associated with the values decreases, however it is important to note the validity of the optical trapping strength value with 50,000 frames as this could reduce the time required to collect the data depending on the accuracy of the value required. As the recording and analysis of 500,000 frames requires ≈ 20 min, in comparison, to ≈ 5 min for 50,000 frames, if taking repeated measurements this could result in a large time difference. For microrheological data collection Tassieri et al. used a simulation to show that 10^6 frames gave a value within 10 % of the actual value[216]. It was therefore decided that for the active microrheological data 500,000 frames would be collected as this number would balance the ability to collect a value of reasonable accuracy without unnecessary time wasting. The data collected with passive microrheology was limited to approximately 100,000 frames due to the beads leaving the region of interest.

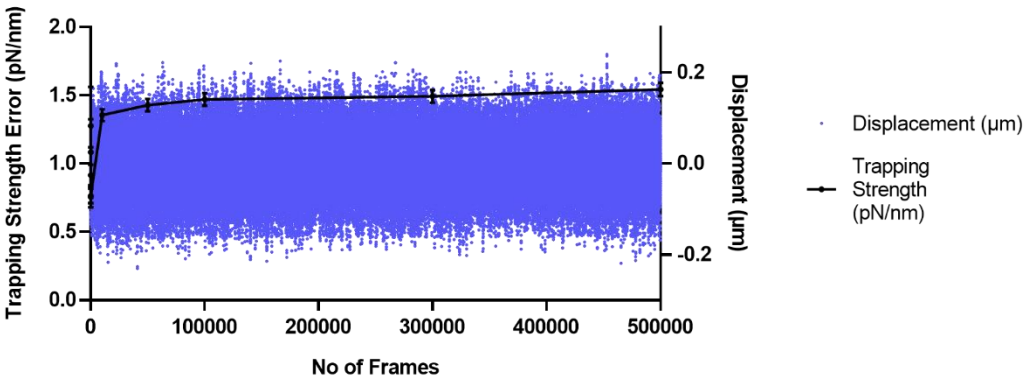


***Figure 3.7*: Optical trapping strength of a 2 µm bead in water and associated error with number of frames.** *The graph shows the displacement of the bead from its equilibrium position along with optical trapping strength at varying number of frames. The value of the optical trapping strength began to stabilise following 50,000 frames. The standard error of the optical trapping strengths was calculated using* $\frac{\kappa}{\sqrt{2n}}$, *where* n *is the number of frames*[316].

As defined above in **Eq. 9**, the microrheological data is collected by analysis of the MSD of a bead within the material of interest. If the material were purely viscous, the MSD of a bead acting with Brownian motion would produce a linearly increasing slope on a logarithmic plot against time lag (the time between frames defined as the inverse of frame frequency). In contrast, a purely elastic medium would produce an unvarying slope of 0. For a viscoelastic medium, a logarithmic plot of the MSD would display a slope between the extreme cases of a viscous plot of 1 and an elastic plot of 0[256].

Upon approaching active microrheology, it is important to be aware that the optical trap could restrict the Brownian motion of the bead, thus overshadowing the influence of the materials' mechanical properties, and rendering the MSD slope to a gradient of 0 with time. Therefore, for collection of the maximum amount of microrheological information, the lowest laser power capable of optically trapping the probe should be used and therefore the restriction on the bead minimised. This is because the bead is within a potential well, formed by the optical trap. The depth of the potential well is proportional to the trapping force, meaning that as the laser power is increased, the amplitude the bead can explore as a freely diffusing particle reduces (this was observed in **Figure 3.6c**). The point at which the MSD plateaus is therefore the lowest

frequency at which microrheological data can be collected, which is defined as the corner frequency and is proportional to the optical trapping strength[216,257,258]. **Figure 3.8** shows an example of a log-log plot of the MSD against a. lag time and b. frequency, showing the larger time intervals (lower frequencies) see the onset of a plateau region in the MSD, highlighting the requirement of collecting short time lag, high frequency data to avoid optical trapping restricting the movement.

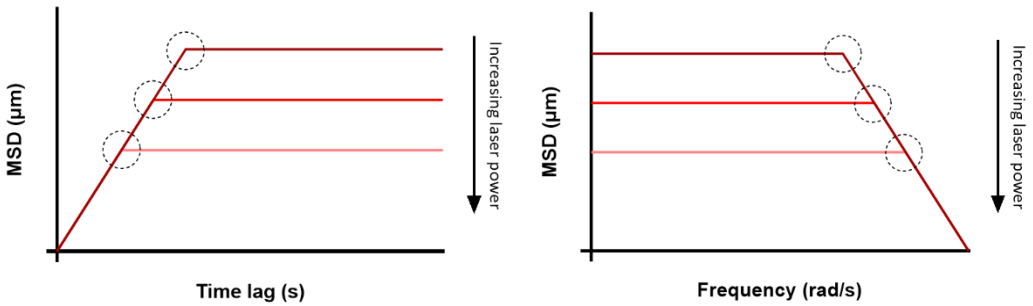


Figure 3.8: Logarithmic plots highlighting the changing corner frequency with increasing laser power for active microrheology. *The gradiented areas of the graphs represent the regions over which rheological data can be collected as the beads' movement is freely diffusing within the surrounding material. The regions over which the MSD is unvarying show that the bead is constrained by the trap. The increasing laser power does not alter the gradient of the slope but decreases the region over which rheological data can be collected. The corner frequencies (the lowest frequency that the bead acts as if it is freely diffusing) are circled.*

A further important factor for collecting microrheological data is the capability of the system to record the movement of the probe at a high frame rate. This is required as lower frame rates result in more diffusion between frames meaning information regarding the beads displacement would be lost, as seen in **Figure 3.8** where lower frequencies results in a plateau of the MSD meaning no microrheological data can be collected. High frame rates means the data is recorded with short time intervals and therefore over small displacements, resulting in a larger region over which the data can be analysed (**Figure 3.8**)[259,260]. Furthermore, a higher frame rate results in quicker collection of data. This is important when considering potential drift of the probe from the region of interest[261]. The frame rate is limited by the camera and computer technology. Within this project the frame rate was optimised by reducing the region of interest in the LabVIEW software to approximately 5 µm by 5 µm to purely capture of the

range of the beads movement. Therefore, unless stated otherwise, the microrheological data presented in this thesis was recorded at 600 fps, a value comparable to data using similar methods[20,217].

3.5.2. Water

In order to confirm the optical trapping system and post-processing analysis to be capable of determining microrheological properties, active microrheology was performed within sterile water. This was completed as the complex modulus and other rheological properties of water are greatly understood and quantified in literature[262,263]. For this experiment, 2 µm diameter beads were suspended in sterile water and optically trapped with the lower laser power achievable (< 5 mW at the sample) at a depth of ≈ 20 µm into the sample (**Figure 3.9**).

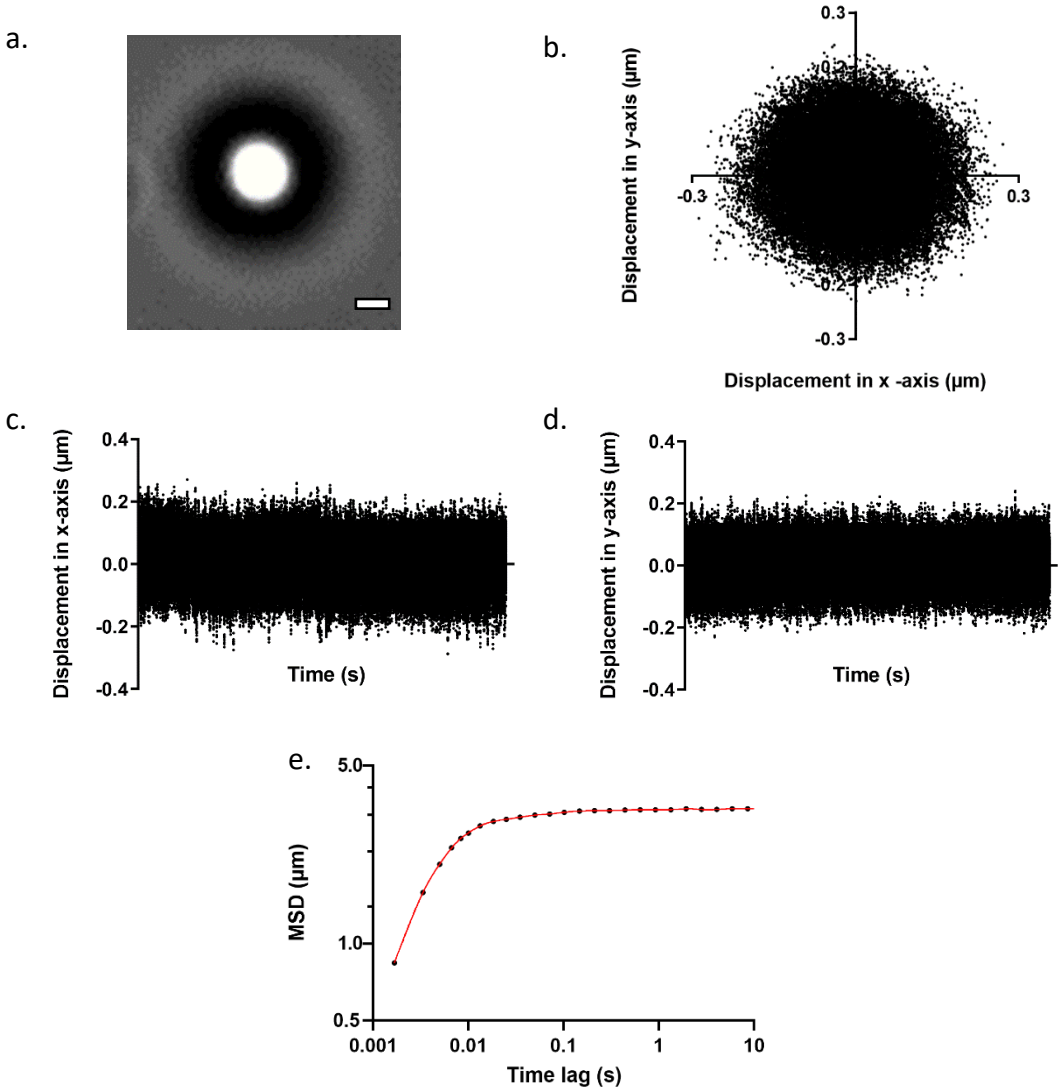


Figure 3.9: Quantification of the Brownian motion of a 2 µm bead in water. a. *Image of a bead within an optical trap taken during recording of Brownian motion. Scale bar = 1 µm.* ***b.*** *x-axis versus y-axis displacement scatterplot of active microrheology of water using a 2 µm optically trapped bead (<5 mW at sample).* ***c,d.*** *Displacement as a function of time, showing the lack of drift within the system in the x-axis and y-axis respectively.* ***e.*** *The mean squared displacement (MSD) plotted against lag time.*

Figure 3.9b, c, and d. are in agreement with what is expected from a spherical bead optically trapped in a homogeneous material with a single Gaussian laser beam, showing a uniform distribution of thermal fluctuations and no drift of the bead over the time taken to record the measurements. **Figure 3.9e** shows the MSD of the bead plotted against lag time, showing the trend introduced in **Figure 3.8**, demonstrating a positive gradient for short time intervals indicative of a freely

diffusing bead in water. Over larger time intervals the gradient becomes a plateau indicating the optical trap has become the dominant effect.

LabVIEW software translated the quantified Brownian motion into the complex viscosity of the surrounding material. As expected, the viscosity was stable across the range of frequencies studied (10 – 1000 rad/s), at a mean value of 1.073×10^{-3} Pa.s (**Figure 3.10**). From the literature, a value of 1.002×10^{-3} Pa.s is expected for the viscosity of water at 20°C[263,262]. This value is only 7.1 % above this idealised value, a difference most likely arisen from the low number of experimental repeats, allowing us to conclude the successful use of the optical trapping system to extract the material's viscosity.

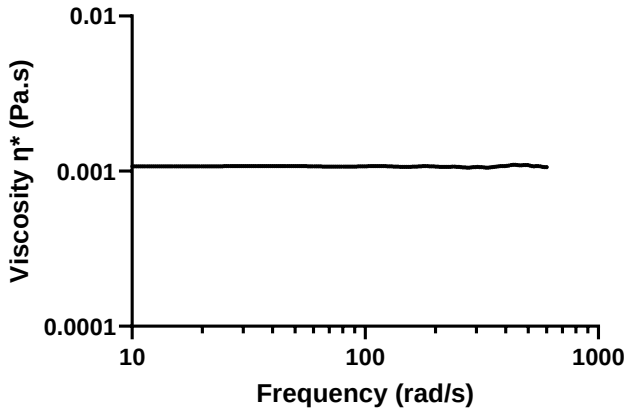


Figure 3.10: Complex viscosity, η* (Pa.s) of water against frequency (rad/s) as determined by active microrheology. *Results collected using a 2 µm bead within an optical trap (<5 mW). 500,000 data points shown. N=1.*

3.5.3. Peptide gel and Matrigel™

Experimentally, the first step to establish rheological methods in peptide gel was finding an appropriate well type in which cells could be cultured within the gels with reasonable media exchange, but also enabling optical trapping. I decided upon the use of Ibidi 8-well µ-slides. These slides enabled all preparation and imaging of the gels to be performed within one contained environment, therefore, minimising the risk of changing the mechanical properties of the gels through shear thinning. The lidded coverslips enabled optical trapping and manipulation of beads and cells without the risk of affecting the mechanical properties or

architecture of the hydrogel whilst maintaining sterile conditions, meaning optical trapping did not need to be the end point of experimental analysis. For all experimental procedures involving the use of optical trapping in peptide gel and Matrigel™, all samples were therefore seeded, cultured, and immunofluorescence stained (if required) within Ibidi 8-well µ-slides as described in methods.

Following the success of active microrheology in water, the same process of active microrheology was attempted to collect viscosity data from 6 mg/mL peptide gel. This produced the scatterplots seen in **Figure 3.11**. Multiple scatterplots were collected at varying x, y, and z locations up to a depth of ≈ 50 µm into the peptide gel. All graphs demonstrated varying plots forms, which suggest a heterogeneous structure of the gel.

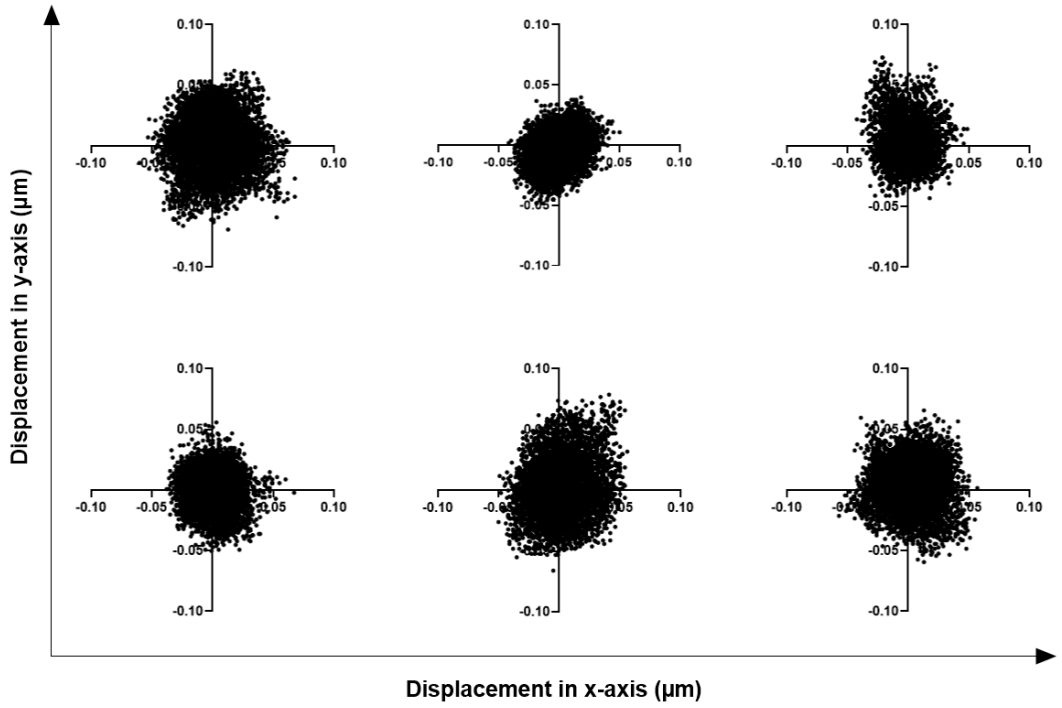


Figure 3.11: Scatterplots of 2 µm bead displacement in 6 mg/mL peptide gel optically trapped with ≈ 130 mW at the sample*. 6 sets of results from 6 different beads suspended within varying positions and depths within the gel displaying varying scatterplot shape and size. For each bead, a total of 20,000 frames were collected with an interval time of 0.02 ms.*

To optically trap the beads within the peptide gel, a laser power of ≈ 130 mW (at the sample) was required. Due to reasons stated in **chapter 3.5.1**

this use of laser power could reduce the rheological information that could be collected from the data. Furthermore, through this experiment, it was concluded that the use of active microrheology was unnecessary as the peptide gel supports the beads within a reasonable ROI (≈ 20 µm by 20 µm) for collection of ≈ 200,000 frames with a frame rate of 600 fps.

The quantification of the Brownian motion of the beads was therefore retaken using passive microrheology. For this experiment, the peptide gel was studied at two phases, i) 'pre-cursor' and ii) 'peptide gel'. These have been previously defined in **chapter 3.1.4**, and refers to the phase at which the gel is optically clear and self-supporting, prior to pH neutralisation, and the latter is the final gel formed after pH neutralisation by media washes. As can be seen from **Figure 1.3** describing the peptide gel fabrication, the pre-cursor is the phase at which the cells are usually added. The pre-cursor was therefore expected to be of a lower viscosity than the final peptide gel as a lower viscosity is required at this phase to ensure a homogeneous addition of cell suspension. By collecting data from both of these phases results could be compared against each other to confirm and quantify the increase in stiffness. This is important as there is no previous literature exploring the use of microrheology in peptide hydrogels. 5 repeats of each condition were completed and the beads were located at varying depths ((10 µm – 40 µm) into the sample) and at different x,y locations. Bulk rheology of the two phases of peptide gel (performed by Dr Jennifer Ashworth using parallel plate rheology) is also shown for comparison (**Figure 3.12**).

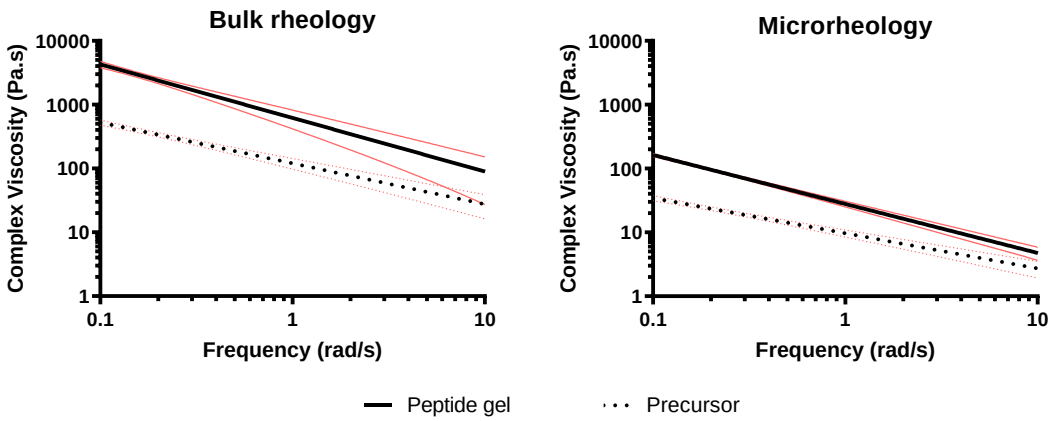


Figure 3.12: Complex viscosity of 6 mg/mL peptide gel as measured by optical tweezer-based microrheology and oscillatory plate bulk rheology (performed by Dr Jennifer Ashworth). *Microrheology results shown as an average of 5 data sets with 95 % confidence intervals shown in red.*

Figure 3.12 showed a marked increase in the viscosity in the peptide gel compared to the pre-cursor; with both techniques showing approximately an order of magnitude difference. As seen in J.C. Ashworth et al[231], the absolute values measured by microrheology are an order of magnitude lower than those measured by bulk rheology (**Figure 3.12**). However, although these absolute values are different, the increase of stiffness across the gel phases as examined by both techniques is the same.

Interestingly, although peptide gel structure heterogeneity was suggested previously in **Figure 3.11**, the results collected using passive microrheology were remarkably consistent, demonstrating small variability between repeats as shown by the 95 % confidence intervals. One potential reason behind this difference could be that due to the optical trap, passive and active microrheology could be examining different length scales and therefore observing different microenvironments. This was investigated by comparing the variance of the displacement of the bead with time for each condition. From the data collected, it was predicted that the active microrheology would have shown smaller variance of movements due to the constraining force of the optical trap. However, upon comparison, the data collected using active microrheology shows a higher

variance of ≈ 0.1 μm, compared to ≈ 0.02 μm for passive microrheology (data not shown).

I therefore believe the reason for seeing scatterplot size and shape variation in **Figure 3.11** was due to the location of the optical trap. It is possible that with active microrheology I could have been self-selecting weaker pockets of the gel where it is possible to trap in order to collect the data. Furthermore, it was difficult to determine whether the bead was directly in the focus of the trap. Therefore, it is possible that the trap was off-centre from the centre of mass of the bead, causing a pulling of the bead from its position within the peptide gel, resulting in the inhomogeneous scatterplots. This added unnecessary complication and supports our use of passive microrheology for subsequent experiments involving 3D materials, and suggests the material is homogeneous at this scale as the passive data implies.

A further influence on the microrheological data of the peptide gel is temperature. As the peptide gel is dependent upon temperature to achieve its final viscosity, all efforts were taken to keep samples as close to 37°C during analysis. For bulk rheology conducted by Dr. Jennifer Ashworth, the rheometer plates were able to be kept at 37°C, however, for microrheology, the optimal method to reduce temperature variation was to minimise the time that the sample is out of incubation, and keep the room warm (30°C as controlled by air conditioning unit). Despite all efforts, it was found that if the sample was out of 37°C incubation for over 20 min, it had a noticeable effect on the results (particularly for pre-cursor phase gels), showing an increased viscosity. For this reason, all collected results for pre-cursor gel microrheology were collected within 15 min of a sample leaving incubation (37°C and 5 % CO_2 in a humidified atmosphere). This resulted in minimal variation as supported by small 95 % confidence intervals.

To shed more light on the difference observed between rheological scales, as shown in **Figure 3.12**, passive microrheology and bulk rheology (the latter performed by Dr Jennifer Ashworth) was performed on Matrigel (**Figure 3.13**). Matrigel is an undefined, hydrogel-like model which has been well characterised

with bulk-rheology, including within the same paper where these results were first published[231]. Comparison of this data displays the same difference of an order of magnitude supporting our conclusion that although absolute values vary, the increase in viscosity is the same between methods. This data can also be compared to literature; the storage modulus of Matrigel as measured by bulk methods is 200 Pa[14], a value that was replicated by bulk rheology here (**Figure 3.13b)**. Microrheology demonstrated a value of just below 20 Pa – a difference of almost exactly 1 magnitude, agreeing within the difference seen in peptide gels between the two rheological techniques.

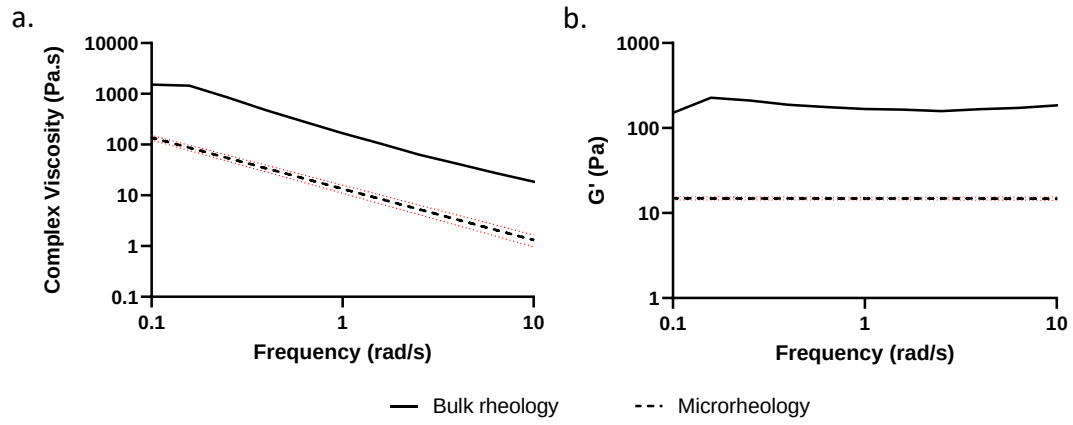


Figure 3.13: Microrheological data of 100 % Matrigel™. a. *Complex viscosity and* ***b.*** *Storage modulus as measured by passive microrheology and bulk rheology (the latter completed by Dr Jennifer Ashworth) showing a difference of an order of magnitude between the techniques. Microrheology data shows trendline for averaged data across N=3, n=3 with 95 % confidence intervals shown in red.*

Continuing this technique into stiffer hydrogels (10 mg/mL) introduced some complications. The data collected from 10 mg/mL peptide gels seems to imply that maximum viscosity measurable by this method has been reached. This is because despite the difference in stiffness observed between 6 mg/mL and 10 mg/mL gels using bulk oscillatory rheology[231], 10 mg/mL peptide gels as measured by microrheology have very similar values as the 6 mg/mL gel with larger uncertainty (**Figure 3.14**). This could be due to the resolution achievable by the optical trapping system. The average displacement of the beads from equilibrium in the 10 mg/mL gels was approximately 0.01 µm, and the smallest movement the optical system can reliably detect is a few nanometres. The results

collected are therefore very close to the minimum variance the system can measure and could have led to the larger confidence intervals seen in **Figure 3.14b.** The 10 mg/mL gel appears to be dampening the probe beyond amplitudes the optical system is capable of measuring.

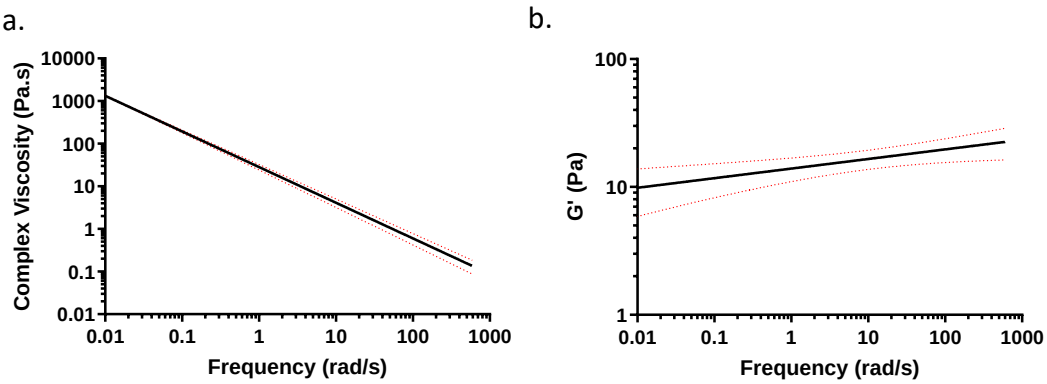


***Figure 3.14: Rheological properties of 10 mg/mL peptide gel as measured by passive microrheology**. **a.** Complex viscosity and **b.** storage modulus of 10 mg/mL peptide gel showing 95 % confidence intervals.*

3.6. Optical manipulation of viable cells in peptide gel

Optical manipulation of cells in peptide gels was attempted with the aim to explore cell-cell interaction forces within the 3D microenvironment. This included optical manipulation of U937 cells at varying stages of culture within peptide gel, in addition to analysis of the cell viability during and after optical manipulation.

3.6.1. Manipulation

U937 cells were used for establishing the technique and methods involved in optical manipulation as they are a relatively uniform cell line and are cultured in suspension as predominately single-cells with limited cell-cell interaction forces. This was desirable as it enabled movement of single cells without undesired adhesion to the coverslip surface.

Optical trapping and manipulation of U937 cells in 6 mg/mL gels was completed at varying depths, positions and laser powers and it was discovered that although it was possible to manipulate some cells in this situation this was

not consistent (**Figure 3.15**). Despite reliable fabrication and cell-seeding of the peptide gel, some cells were able to be optically trapped and manipulated in the gels (**Figure 3.15a**), and other cells (within the same well) could not be moved at all regardless of laser power. This effect did not appear to be related to location of the cell in relation to depth, nor distance from the edges of the wells. However, it could be related to cell cluster size, with cells within or near larger clusters being harder to optically trap, suggesting that the larger clusters have stronger interaction forces. This could suggest that although these cells are not known to expel high amounts of ECM (as supported by their inherent single-cell culture in liquid medium), they expel some ECM affecting the local microenvironment causing stronger interactions.

However, there were exceptions to this finding, such as the manipulation of cell-cell interaction forces seen in **Figure 3.15b**, whereby a single cell on the edge of a cluster of cells can be trapped and pulled away revealing visible interactions between the cells. A range of immunocytochemistry was completed on these cells in an attempt to elucidate what these interactions could be due to and results suggested from strong CD44 (cell-surface glycoprotein involved in cell-cell interactions) staining that it could be hyaluronan, however, further specific staining would be required to confirm this (see **Figure 8.1** in appendix). Despite attempts with high laser powers (>400 mW at sample) the U937 cell being manipulated in **Figure 3.15b** could not be removed from the cluster.

Figure 3.15c demonstrates optical manipulation within a co-culture of U937 cells and 2 μm beads. In this series of figures, a bead is optically manipulated to contact and adhere to a cell to act as an optical-handle. Movement of the bead then moves the cell.

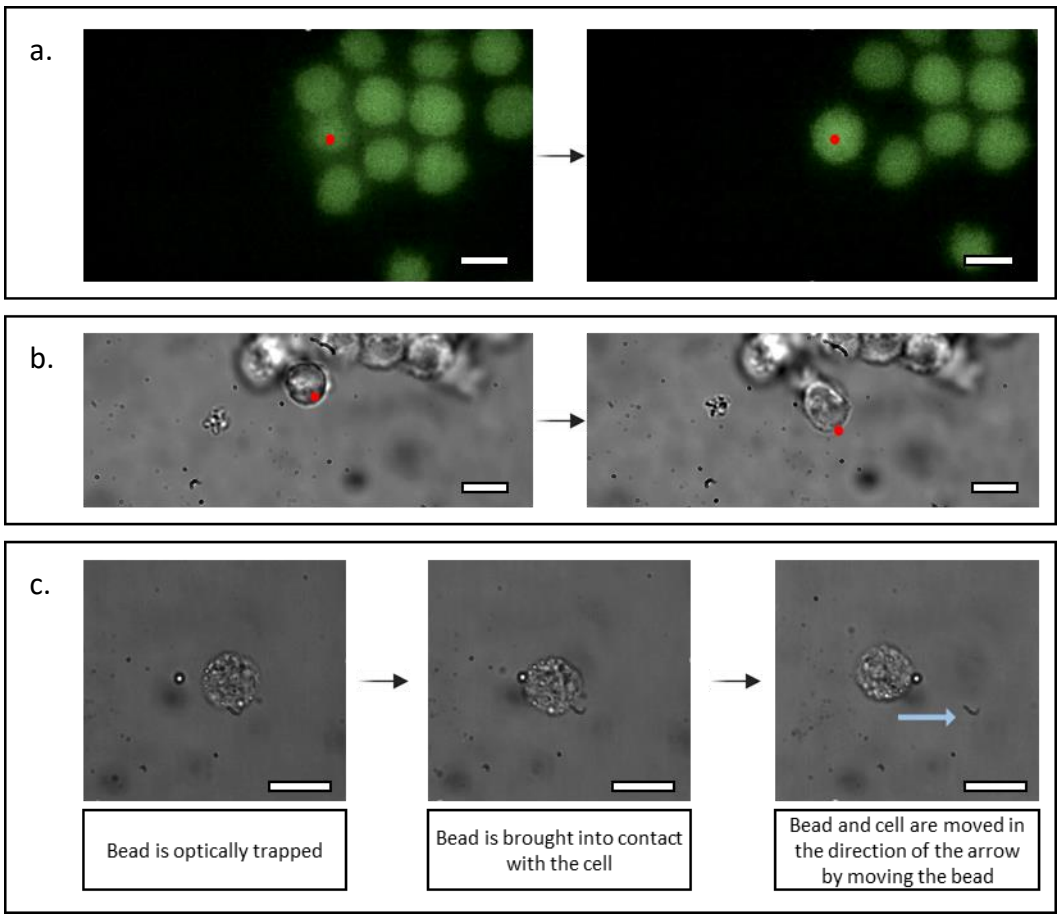


Figure 3.15: Optical manipulation of live U937 cells in 6 mg/mL peptide gel. *Laser focus is shown by a red dot.* ***a.*** *U937 cells stained with Calcein AM to indicate viability, optically manipulated within the gel (≈ 60 mW at sample),* ***b.*** *U937 cells in 6 mg/mL peptide gels manipulated with up to ≈ 400 mW at sample, showing cell-cell interaction forces limiting manipulation,* ***c.*** *2 µm polystrene beads co-cultured with U937 cells in 6 mg/mL peptide gels, images from left to right demonstrate the process of manipulating the bead to contact a U937 cell then using the bead as an optical handle to move the attached cell (≈250 mW at sample). Scale bars = 10 µm.*

3.6.2. Viability analysis of U937 cells

To analyse the viability of the cells during and after optical manipulation, U937 cells in liquid culture were stained with Ethidium-Homodimer-1, a nuclear stain that fluorescence's upon cell death (**Figure 3.16**). A low concentration of cells was used to ensure only one cell was within the trap at any one time for accurate use of the centre-of-mass algorithm. The expression of the stain upon cell death was confirmed first by using cells the day after thawing from cryopreservation which are more sensitive than cells in continuous culture. A cell from the cryopreservation was trapped with 180 mW at sample and after 30 min of optical

trapping, fluorescence was evident, showing this method of observing cell viability to be effective.

To investigate the cells grown in continuous culture, a cell was optically trapped with a high laser power (≈450 mW at sample) and held within the optical focus for up to 180 min. This laser power was chosen as although a laser power of this magnitude was not used for future experiments, I wished to expose the cell to the most potentially damaging situation. At appropriate time intervals, white-light and fluorescence images were taken to assess any changes in cell morphology or cell death by fluorescence, respectively. **Figure 3.16** shows that after 1 h of optical trapping no changes were observed. After 180 min morphological changes appeared in the white light image suggesting the cell was under distress, however, no fluorescence was observed to suggest cell death. This experiment was repeated multiple times with a lower (more commonly used) power of ≈ 250 mW at the sample for up to 30 min (N=5) with no indication of cell distress in white-light images nor fluorescence.

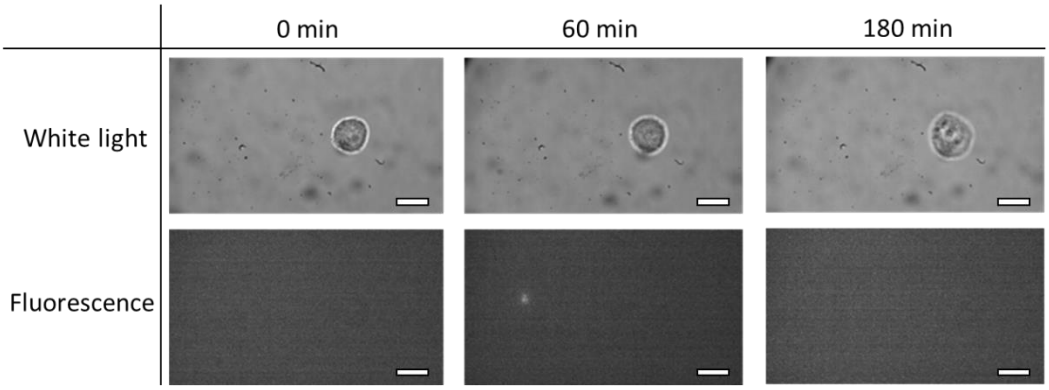


Figure 3.16: Viability analysis of U937 cells during optical trapping. *White light and fluorescence images of the same cell trapped with single focal spot laser in liquid culture (≈450 mW at sample). Culture was stained with Ethidium Homodimer-1 which would fluorescence upon cell death. Scale bars = 10 µm.*

As a result, we could be confident that the cells remained viable for the parameters used in the experiments of this thesis, whereby optical trapping did not occur for longer than 30 min with an average power of 5 -100 mW at the sample.

3.6.3. Complexities of quantifying cell manipulation

To quantify the trapping strength of cells, the same experimental process as demonstrated in **chapter 3.4** was attempted using leukaemic cell line U937. The cells were successfully trapped and manipulated at a range of laser powers (< 5 mW - 450 mW at sample) in media suspension, however the centre-of-mass tracking software was unable to reliably threshold the image in order to perform post processing analysis of trap strength. This is because, unlike beads which are homogeneous in shape and refractive index, cells can be inhomogeneous in size, shape, and refractive index (**Figure 3.17**).

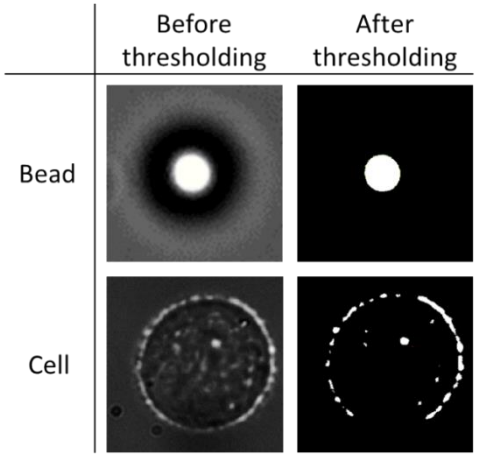


Figure 3.17: Thresholding of beads compared to non-homogeneous cells. *Images of a 2 µm polystyrene bead and U937 cell before and after thresholding performed by MicroManager software in order to determine the particles centre of mass for tracking analysis.*

This can also cause issues during optical trapping as often a trap will act upon a region of greatest refractive index change (e.g. the nucleus or the membrane of the cell). When optical tweezers trap a single feature of the cell with a high refractive index (e.g. the nucleus), this produces a trap about which the cell can rotate and re-orientate due to Brownian motion. This causes issues in thresholding and therefore quantifying the behaviour of the cells. Previous research conducted by Glass et al. demonstrated this rotation and showed by using an SLM to manipulate the beam profile, that three closely spaced traps can be formed and located within a single cell to minimise cell roll[20]. These three traps allowed the cell to be trapped as a whole, rather than a single feature, overcoming

the rotational instabilities and increasing the accuracy of tracking and control of cellular movement.

Figure 3.18a and b show how the SLM can form these optical traps. The SLM produces a diffraction pattern which can be controlled using LabVIEW software (originally developed by the Padgett Optics Group at the University of Glasgow and adapted by Amanda Wrights group at the University of Nottingham) to split the single laser beam (N=0) into multiple focal spots. As the beam continues to be split into additional diffraction patterns the power to the individual optical traps reduces, as the power is divided between the multiple optical traps. A triple optical trap was achieved using the 0^{th} order and two of the 1^{st} orders (highlighted in **Figure 3.18a**). The 1^{st} orders can be controlled independently of each other by changing the spacing and orientation of the diffraction patterns relative to each other. This allows the 3 traps to be manipulated as required as to fit within a cell (**Figure 3.18c** and **d**). This method was used by Glass et al. to measure relative interaction forces at the single-cell scale with precise control of contact time and location[28], and should be considered for future work continuing from the research presented in this thesis.

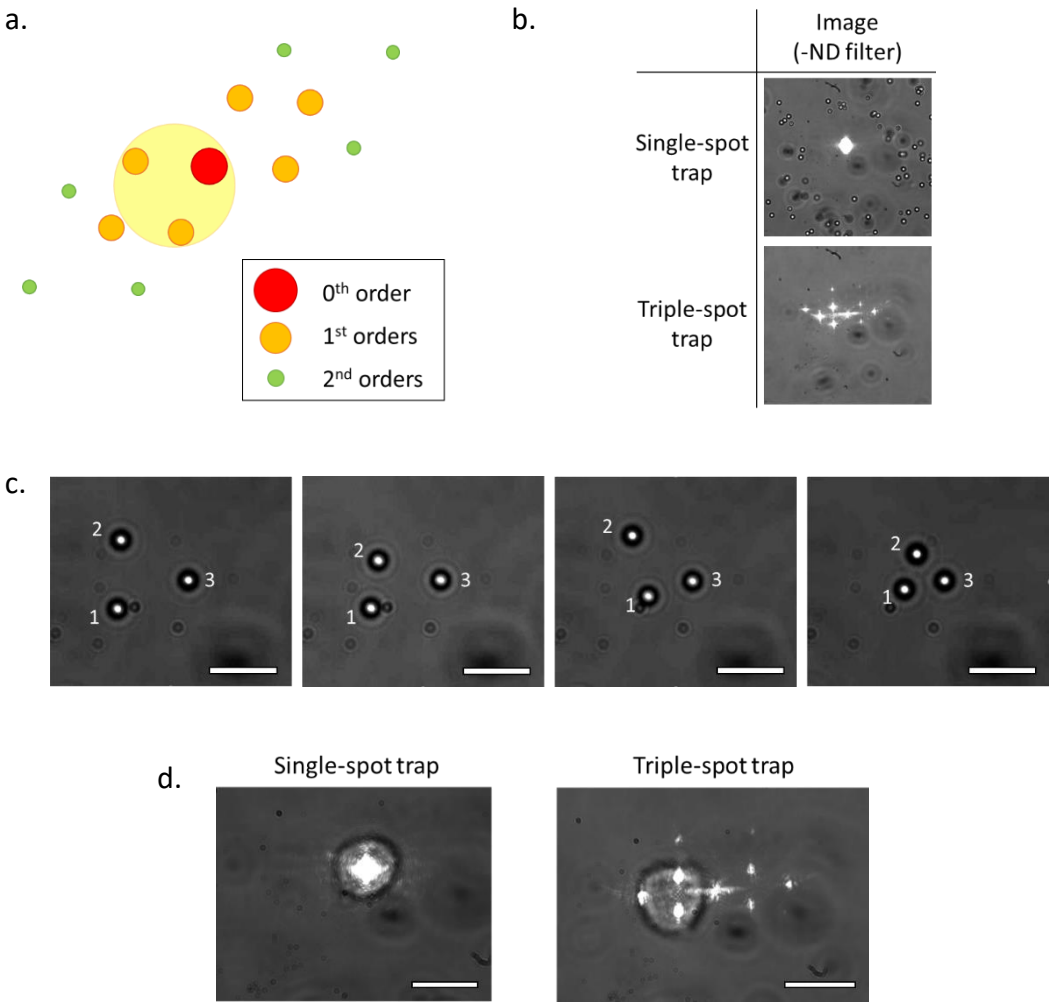


Figure 3.18: Optical trapping of polystyrene beads and U937 cells with triple-spot optical traps as formed by an SLM. a. *Schematic of how multiple focal spots are formed by the SLM, highlighting the three focal spots used for triple focal spot optical trapping.* ***b.*** *Images of single and triple-spot traps with corresponding hologram for the SLM.* ***c.*** *Series of white-light images of 3 beads demonstrating trapping and individual manipulation of three optical traps.* ***d.*** *Single and triple-spot optical traps placed inside a U937 cell. Scale bars = 10 µm.*

3.7. Discussion

The ability to perform optical trapping within peptide gels is an important development towards establishing single-cell scale analysis techniques within 3D models. This chapter demonstrated the ability to use optical tweezers to perform a variety of experimental methods to expand our knowledge of the novel, defined, self-assembling peptide gels with human leukaemic cell lines.

The quantification of optical trapping strength was performed by modelling the behaviour of a probe in water using the equipartition theorem. The

position variance of a trapped probe (bead) was recorded in real-time using an in-house developed LabView program and successfully showed the linearly increasing relationship between the laser power of the optical trapping beam and the trap stiffness (**Figure 3.6**), as previously observed in literature[28,264–266].

As the peptide gel does not contain any biological material or proteins that can be stained and imaged using fluorescence imaging techniques, the only possible method to view the microstructure of the gel is by high-resolution microscopy, such as transmission electron microscopy (TEM) or scanning electron microscopy (SEM). TEM on similar peptide hydrogel has been previously attempted by Alberto et al.[267], which showed a uniform network of thin, 3-5 nm, entangled fibres. However, this technique is very challenging in hydrogels due to the preparation steps for imaging requiring dehydration of the sample, thus previous studies have seen a dramatic change of the microstructure of the gel. This means that the resulting TEM image may not accurately represent the microstructure present to the cells during culture. For this reason, in recent years, alternative sample preparation procedures have been developed in attempt to recapitulate the native state of the material or tissue more closely. One such method is cryo-preservation[268–270]. This is a physical rather than chemical immobilisation and aims to maintain the microstructure of the material. However, this is a challenging process which requires extensive optimisation, not least to interpret the low contrast outputs, to ensure visualisation of native architecture.

Therefore, to explore the rheological properties of the peptide gel at a scale relevant to single-cell behaviours this study approached optical tweezer-based microrheological methods. This technique not only allowed for quantification of the viscosity and the storage modulus of the peptide gel but also enabled investigation of any potential heterogeneities that may exist at the microscale.

Microrheology of water was completed using active microrheology and was used to confirm our ability to collect accurate rheological measurements. Our data agrees with Einstein's prediction for a probe freely diffusing within a Newtonian fluid, demonstrating circular scatterplots of x and y displacement from

equilibrium, and does not show position drift in the x or y-axis with time (**Figure 3.9**). As previously mentioned, the slightly increased experimental value from the theoretical could be due to localised heating from the laser or by variance in the room temperature as the viscosity of water is only 1.002×10^3 Pa.s at 20°C[263]. However, as this difference is minimal (within 7.1 % of the theoretical value) and was recorded from one biological repeat, we can conclude this value to be sufficient to confirm our ability to measure rheological properties.

Upon attempting active microrheology within the 6 mg/mL peptide gels, the x-y displacement scatterplots (**Figure 3.11)** implied heterogeneity of the gel through varying plot shapes and sizes. However, this variation could be due in part to technical difficulties that occurred when trying to trap the beads within the hydrogel without moving the beads before collecting the data. Any movement may cause interruption of local pore size or hydrogel architecture, and therefore affect the results. All efforts were taken to reduce this, including turning the laser off until the focal spot lay directly over the bead of interest, however, this may impact individual results.

Microrheological data of peptide gel was therefore collected passively – without the use of optical trapping - as this ensured maximum data collection for quantification of the stiffness of the gel and negated any uncertainties that could occur using optical trapping. **Figure 3.12** showed an increase of viscosity of 6 mg/mL peptide gel during gelation of approximately an order of magnitude and confirmed the same increase of stiffness using bulk oscillatory rheology. Although the same difference between precursor and peptide gel stiffness was observed, the absolute measurement values obtained by the two techniques differed by approximately an order of magnitude. This difference was also evident in Matrigel™ (**Figure 3.13**). In Ashworth et al.[231] we discuss the difference observed in 6 mg/mL peptide gel is to be likely due to the different length scales explored by the two techniques. This could be true, however, since this publication, G. Ciccone et al.[218] have explored the issue that bulk rheology values may also be affected by the normal force applied during

oscillatory rheology. They suggest that conventional bulk rheology measurements commonly overestimate the mechanical properties of hydrogels.

With respect to the relevance of the viscosity of the 6 mg/mL to that of *in vivo* bone marrow, the viscosity sweep shown in **Figure 3.12** was compared to published mechanical analysis of intact porcine bone marrow by Metzger et al.[65]. By comparison of this data, which explored the same frequency range, it can be seen that the viscosity frequency sweep of fresh bone marrow lies almost directly between the viscosity trends of 6 mg/mL peptide gel as measured by microrheology and bulk rheology. This concentration of gel was therefore determined to be approaching physiological stiffness of the bone marrow microenvironment as required for future modelling of the leukaemic niche.

Microrheological data from 10 mg/mL gel was attempted to quantify the increase of stiffness produced by increasing the concentration of peptide powder. This was for further comparative analysis to the bulk rheology data collected which showed a difference of ≈ 1000 Pa between the 6 mg/mL and 10 mg/mL gels on the bulk scale[231]. This difference was not observed using microrheology, potentially due to the probes position variance is being damped beyond amplitudes the optical system was capable of measuring. To confirm this hypothesis, a further experiment should be performed of measuring the perceived position variance is a bead fixed to a surface. This process would show the minimum variance that can be measured, and thus see if this is what is being observed from the 10 mg/mL data.

To our knowledge, we believe we are the first team to show manipulation of live cells in a gelated hydrogel. Previous groups have used optical manipulation of live cells in gels prior to cross linking or by using photopolymerisable gels[17,271]. Using this technique, the cells can be manipulated while the hydrogel is in its less viscous phase, and if used in combination with multiple holographic optical traps, multiple cells can be held in desired 3D locations with submicron precision while gelation occurs. These systems have been developed over the last couple of decades to create living cell microarrays with increasing complexity to study the 3D microenvironment of cells. However, by being able to manipulate the cells at

this scale during culture (i.e. post gelation) as shown here, we open doors to examine the single-cell interactions and behaviour during proliferation. As mentioned in **chapter 3.6.1**, although optical trapping and manipulation of live U937 cells in 6 mg/mL peptide gels has been performed in this study, it was not able to be achieved consistently. This could imply inhomogeneities in the peptide gel at a scale smaller than what was observed using 2 µm beads.

In **Figure 3.15** the optical trapping system was used with the aim of manipulating and quantifying cell-cell and cell-matrix interactions. Theoretically, this could be done in liquid culture of known viscosity by optically manipulating a cell to contact another cell with accurate control of the contact area and contact time, then pull the cells apart. From the equations introduced above (**Eq. 5**) the known calibration of laser power to optical trap stiffness could be used to calculate the force required to separate the cells. This technique has been previously performed by Glass et al. to investigate the interaction forces between a dendritic cell and a specific T-cell[28]. However, in the study presented in **Figure 3.15b**, detachment of a single cell from a cluster formed within the hydrogel was not achieved, even when using increased laser power. This could be because despite using the same wavelength laser and higher power than Glass et al., they investigated controlled contact time of 120 s. These forces could predictably be weaker than the forces formed between two daughter cells formed by proliferation of a parent cell. Nonetheless, this highlights a key area for further optimisation and development of this system, as the capability to detach single cells would improve our ability to investigate adhesion forces present in cell clusters.

At this stage in the research, the cell-cell or cell-matrix interactions with cells in peptide gel could not be quantified as there are two ‘unknowns’ – the bio-physical/viscosity properties of the cells, and the 3D response of the peptide gels. This is because despite knowing the viscosity of the gel, it is not known how the gel reacts to microscale movement. For example, if a cell were trapped and moved in a linear path through the gel, would this leave a path within the gel or would the gel be able to ‘seal’ this path behind the movement? Does the gel

become denser after the cells have proliferated into clusters causing an increase in local stiffness around the cells as they continue to grow? As the gel comprises no proteins that could be stained for fluorescence imaging, one of the ways to study it this is the case would be to exploit the use of the method of gathering displacement scatterplots in hydrogels as seen in **Figure 3.11**. This would involve taking a scatterplot of a bead seeded within the hydrogel then moving the bead a known direction and distance in the x or y-axis. Another scatterplot would be taken in this new location, then the bead would be moved half the distance back along the same line and a final third scatterplot would be recorded (**Figure 3.19**). From the shape of the scatterplots this should show restriction of the scatterplots to indicate the response of the gel.

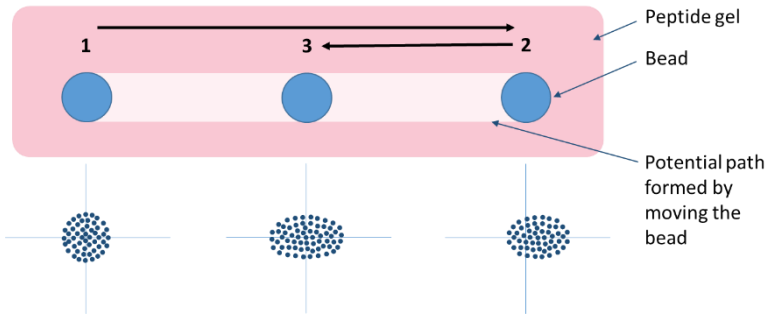


Figure 3.19: Example experiment for observing peptide gel response to bead manipulation. *Figure shows where scatterplots would be recorded with example corresponding plots should the movement of a bead through the peptide gel form a 'path'.*

Successful co-culture of beads and cells as shown in **Figure 3.15c** opens many doors for potential future experiments. This technique has been adopted in previous literature as using beads attached to cells prevents possible damage to the cells as the laser focus is no longer on the cell of interest, and also enables optical manipulation of larger objects[204,21]. This technique offers opportunities such as the use of functionalised beads for microscale observation and time control of cell response to selected stimuli. Having beads within the same gel as cells could also enable microrheology in cell-seeded peptide gels, enabling insight into the potential local effects the cells could have to the viscosity of the gel.

From personal experience of optical trapping polystyrene beads and live cells within peptide gel, anecdotally the manipulation of live cells was easier than beads. Although this should be interpreted with caution, through many experiments I found beads were largely unable to be moved using an optical trap within 6 mg/mL gel, whereas I would estimate I could move approximately 50 % of U937 cells over the same depth. This could be due to the reasons as mentioned above, that the cells could be excreting ECM and affecting local microenvironment. It is also worth noting that despite multiple attempts, optical trapping in higher concentration gels (10 mg/mL) was not possible. This concentration of gel was too stiff for our optical trapping system to move either a cell or a bead.

For the first time with leukaemic cells, this study repeatedly demonstrated cell viability during and after optical manipulation. **Figure 3.16** shows U937 cells to remain viable upon exposure to a laser of higher power and over a longer time period than has been used for any other results in this thesis. Several repeats (N=6) were also conducted over 30 min (the maximum time typically used for collecting results) at ≈ 100 mW laser power which consistently did not cause any damage to the cells as determined by Ethidium Homodimer-1. Although performed on a different cell type, this agrees with previous optical trapping viability analysis conducted by McAlinden et al. where they used the same wavelength of laser and T-cell hybridomas, and showed that after 65 min of trapping with ≈ 400 mW (at the sample) 33 % of trapped cells expressed propidium iodide (a marker of cell membrane permeation)[272].

A valuable future experiment would be to also confirm cell function after manipulation. This would involve seeding of cells within peptide gel then performing optical manipulation. The sample should then be incubated at 37˚C/5 % CO_2 in a humidified atmosphere and viewed over the following days. As the cells are supported by the peptide gel, the cells should not move around the gel; and if used in combination with a gridded coverslip, the same cells that were optically manipulated should be able to be tracked for proliferation. If the cells

continue to proliferate into a cluster following optical manipulation, it can be assumed the function of the cells not to be impaired.

Figure 3.17 shows the difference in thresholding the polystyrene beads compared to cells. Living cells are highly dynamic and possess inhomogeneous internal biological features which cause a non-uniform refractive index, therefore resulting in unreliable thresholding for positional analysis of the cells. As discussed in **chapter 3.6.3**, Glass et al. introduced a novel triple-spot optical trap for increased control of the cell movement[28]. This technique was replicated in **Figure 3.18** and should be exploited in future work for interrogating quantitative cell-cell and cell-matrix forces.

Chapter 4: Optimisation of peptide gel models for application to leukaemic and haematopoietic study

4.1. Introduction and aims

Mouse models are currently the gold standard for pre-clinical leukaemia research[167,168]. These models are integral and currently indispensable within biomedical research, providing complexity of structure that cannot currently be achieved synthetically. However, as they are highly complex in their structure and stimuli response these models can lead to misinterpretation of disease impact and treatment due to lack of comprehensive understanding[173].

This chapter explores the use of the FEFEFKFK peptide hydrogel and demonstrates the ability to modify the 3D models to relevant physiological properties by stiffness control and chemical functionalisation. These peptide gels are designed as a 'blank slate' system meaning matrix modifications e.g. proteins or growth factors can be supplemented to add specificity and functionalisation. This means that the unmodified gels provide a non-interacting 3D environment to directly study the biophysical influences of 3 dimensions on cell properties, behaviours, and interactions. These models therefore eliminate one of the primary factors limiting animal models, as the peptide gel allows for increasing complexity by defined modification of physical and biochemical properties. A property which is critical for understanding the impact of biochemical composition and tissue mechanics on disease and treatments.

Using human leukaemic cell lines, primary mouse cell line, mAF9, and iPSC-derived HSPCs, this chapter explores the ability of the peptide gel to culture the different cells types with the aim of establishing a mechanically-representative model that supports suitable cell proliferation for use in drug testing studies.

4.2. Culture of human cell lines in peptide hydrogels

For optimisation of culture methods within the peptide gels, several subtypes of human leukaemic cell lines were studied within the unmodified 3D model; these included U937, THP-1, MV411, HL60, and OCI-AML3 (subtypes and

further information given in **Table 2.2**). All human leukaemic cells survived and proliferated within the peptide gel with some variation in growth dynamics between cell lines (**Figure 4.1**). The proliferation of the cells varied in colony size and density; ranging from smaller, compact colonies as seen with THP-1 and HL60 cells, to larger, broader colonies as seen in the U937 and OCI-AML-3 cell cultures. Seeding density does not appear to affect colony size of any cell line investigated, with both cell concentrations studied producing similar sized colonies.

The experiments presented in this thesis predominately used THP-1 and U937 cells. THP-1 cells were selected due to their matching onco-fusion with the primary mouse cell line (mAF9) used later in this thesis (*MLL-AF9*), and, therefore, offer a more representative platform for optimisation of protocols prior to primary cell use[233,235]. U937 cells were selected as a comparator leukaemic cell line of a different translocation (t(10;11)(p13;q14))[233]. In addition, U937 cells are characterised as monocytic, and provide a highly uniform cell morphology. This cell uniformity was an important characteristic to consider as a steady parameter base for optimisation studies of single-cell analysis[233].

Figure 4.1: Phase-contrast images of human leukaemic cell lines seeded at 5 x 10^4/mL or 1 x 10^5/mL in unmodified 6 mg/mL peptide gels. *All cell lines proliferated within the peptide gels showing variation in colony size and density. Scale bars = 100 µm.*

4.3. Quantification of cell number within 2D and 3D cultures

The optical transparency of the peptide gels allows for quantitative read-outs of cell proliferation. Previous quantitative analysis in the peptide gel has been conducted using fluorescence readout of genetically modified cell lines with fluorescence reporters[231]. However, to assess the future application of these gels for high-throughput drug screening, it is critical that cells without genetic modification can be quantified within the gels.

Initially, fluorescence assays were approached which could be read by the plate reader, allowing for high-throughput analysis. The first assay investigated was Calcein AM, a viability stain that had previous success in the peptide gels (see **Figure 3.15a**). However, this gave highly fluctuating and unreliable results, greatly varying between biological repeats and not representing the visual analysis as performed by confocal microscopy. It was considered that this could be due to some background staining, however, as this stain should not react with the peptide gel, this was unexpected. The absorbance assay, CellTiter 96®, was also approached and produced very low, inaccurate results due to absorbance by the hydrogel.

Therefore, luminescence assays, CellTiter-Glo® (CTG) and RealTime-Glo™ (RTG) MT viability assays were approached. CTG determines the amount of adenosine triphosphate (ATP) present in the culture, a key biomarker of cell health expressed by metabolically active cells[273]. This assay was developed as an "add-mix-measure" format, eradicating multiple pipetting steps, and promises a high level of detection with a stable luminescent signal, therefore requiring fewer cells per assay. CTG is a lytic assay and produces a luminescence signal proportional to the number of viable cells in the culture by catalysation of luciferin by Ultra-Glo™ Recombinant Luciferase in the presence of Mg^{2+}, ATP and molecular oxygen. RTG is also a metabolic-based viability assay that offers minimal pipetting steps, therefore reducing the risk of compromising the structure of the gel. Contrary to CTG, RTG is a non-lytic NanoLuc Luciferase reaction. The MT cell viability substrate diffuses into the cells where metabolically active cells reduce it to form a NanoLuc substrate which diffuses into the surrounding culture

medium[274]. The Nanoluc luciferase then rapidly uses this to produce the luminescent signal. No reduction occurs within non-viable cells and thus luminescence production is proportional to the number of live cells in the culture. As the reduction is rapidly used by the luciferase, it does not accumulate and consequently expresses a luminescence representative of the number of live cells at a given moment; increasing and decreasing the signal and cells proliferate or die respectively[275]. Combined with the nontoxic reagents this method allows for monitoring of cell viability within the same well over a time period relevant for drug screening.

The same number of cells were seeded into the same volume of liquid media or peptide gel (1×10^5/mL). The assays were left to incubate with the liquid culture for the time recommended by the manufacturer before measuring the luminescent signal (30 min). Incubation time was doubled for peptide gel due to the preliminary results which showed that 1 h incubation time provided sufficient luminescence without unnecessary cell proliferation, thus affecting the calculated cell number. Also, as RTG is temperature sensitive, it ensured the samples had time to reach 37°C. Additionally, doubling the time for stain exposure complies with the previous optimisation of the peptide gels for ICC for confocal microscopy (performed by Stem Cell Glycobiology group at the University of Nottingham).

As can be seen from **Figure 4.2**, both luminescence assays displayed a linear relationship between the cell number and the luminescence in liquid culture and in peptide gel. The peptide gel showed lower luminescence values as compared to liquid culture with the same number of cells. However, both conditions demonstrated a positive gradient, showing the luminescence values to increase as the number of cells increases. According to previous literature, viability assays based on intracellular ATP content, such as CTG, are the most sensitive assays for 3D systems[276,277]. This agrees with the data below. Although both assays demonstrated a reliable measure of cell viability, RTG was able to assess viability in the same well for up to 72 h. This reduced costs by minimising peptide hydrogel

waste and increased throughput by reducing the number of samples required for analysis of multiple time points, which solidified its use for future experiments.

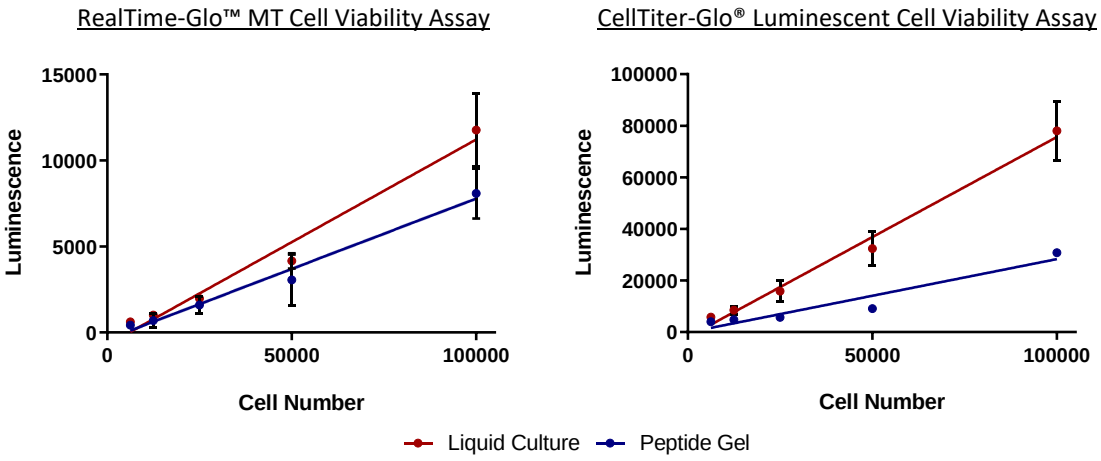


Figure 4.2: Quantification of U937 cell number in liquid culture and 6 mg/mL peptide gels*. Increasing number of cells quantified using luminescence assays read by plate reader demonstrates a linear relationship between cell number and luminescence in both liquid culture and peptide gel. Results are shown as an average of N=3, n=3, with ± standard deviation. Data collected 1 h following initial seeding.*

4.4. Effect of peptide gel concentration on U937 proliferation

In **chapter 3.7** it was shown that the stiffness of unmodified 6 mg/mL peptide gel approached the physiological stiffness of bone marrow. To explore how 3D matrix stiffness affects the cells growth dynamics, U937 cells were cultured within 3 concentrations of peptide gel (6 mg/mL, 10 mg/mL, and 15 mg/mL) and in '2D' liquid culture (note: '2D' refers to suspension liquid culture). As the novel peptide gels do not contain any matrix proteins or binding motifs, this increase in stiffness is independent to any biochemical functionalisation.

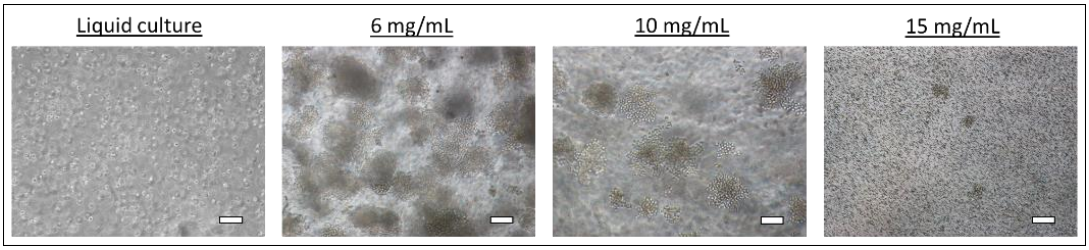
Cell proliferation was assessed by phase-contrast imaging and RealTime-Glo™ luminescence assay (**Figure 4.3)**. Phase contrast micrographs (**Figure 4.3a)** show the increase in peptide gel stiffness changes the number of cell colonies formed and the structure of the colonies (image of high-density liquid culture included for visual comparison of growth dynamics). As the stiffness of the peptide gel increased to 10 mg/mL the gel continued to show the ability to support cell

proliferation however, the colonies became fewer in number and appeared denser and more rounded.

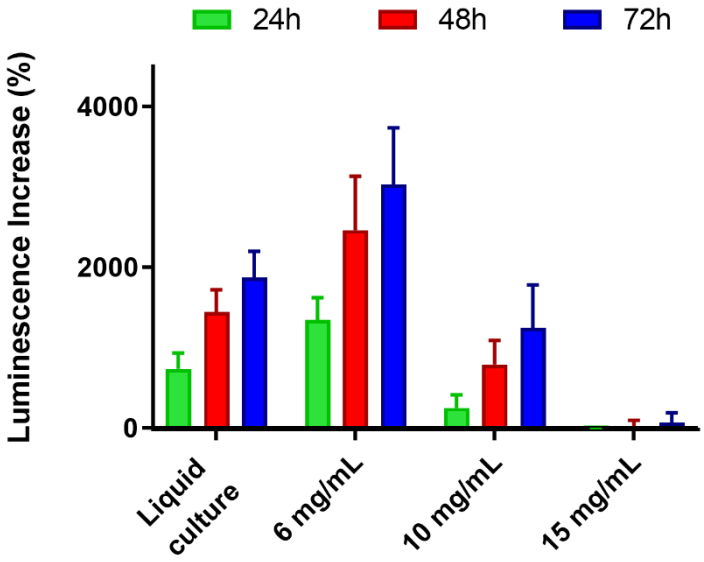
Within the maximum stiffness gel investigated (15 mg/mL) limited cell proliferation was observed by either microscopy or luminescence quantification. According to bulk rheology as performed by Dr Jennifer Ashworth, the 15 mg/mL yields a storage modulus of 5 kPa, a value significantly higher than 6 mg/mL gel which demonstrated a storage modulus of 600 ± 90 Pa ($P<0.05$) as measured by bulk rheology[231]. **Figure 4.3a** shows the 15 mg/mL gel to have produced much smaller colonies by day 7 of culture, but the only proliferation was seen to be at the very bottom of the transwell insert (as can be seen by the static-like background of the image viewing the mesh at the bottom of the transwell insert).

Both means of assessment showed maximum cell proliferation occurred in 6 mg/mL peptide gel as compared to higher concentrations of gel, and quantitative data showed significantly more proliferation occurred in 6 mg/mL gel compared to 2D liquid culture. By 48 h of culture, significantly more proliferation was observed in the 6 mg/mL gel compared to 2D liquid culture, 10 mg/mL, and 15 mg/mL gels, reinforcing the decision to use 6 mg/mL peptide gel for future experiments.

a.



b.



c.

Time point	Comparison	Significance
24h	Liquid culture vs. 6 mg/mL	ns
	Liquid culture vs. 10 mg/mL	ns
	Liquid culture vs. 15 mg/mL	ns
	6 mg/mL vs. 10 mg/mL	**
	6 mg/mL vs. 15 mg/mL	***
	10 mg/mL vs. 15 mg/mL	ns
48h	Liquid culture vs. 6 mg/mL	*
	Liquid culture vs. 10 mg/mL	ns
	Liquid culture vs. 15 mg/mL	***
	6 mg/mL vs. 10 mg/mL	****
	6 mg/mL vs. 15 mg/mL	****
	10 mg/mL vs. 15 mg/mL	ns
72h	Liquid culture vs. 6 mg/mL	**
	Liquid culture vs. 10 mg/mL	ns
	Liquid culture vs. 15 mg/mL	****
	6 mg/mL vs. 10 mg/mL	****
	6 mg/mL vs. 15 mg/mL	****
	10 mg/mL vs. 15 mg/mL	**

Figure 4.3: Comparative analysis of U937 proliferation in liquid culture and increasing concentration of peptide gels. a. *Phase contrast images taken 7 days after initial seeding,* ***b.*** *proliferation percentage measured by RealTime-Glo™ MT viability assay as compared to luminescence read 1 h after initial seeding (1×10^5/mL) g.* ***c.*** *Statistical significance (determined by two-way ANOVA in GraphPad Prism) of data shown in b. *P < 0.05 ,**P < 0.01, ***P < 0.001, ****P < 0.0001. N=3, n=3.*

4.5. Culture of primary mouse leukaemic MLL-AF9 cells in peptide gels

The human cell lines used so far in this study have been in culture for decades, which has been reported to cause the cells to differ genetically and phenotypically compared to the originally extracted cell type[274]. Although cell lines offer advantages such as high proliferation rates, ease of culture, and can be compared to previously literature, caution must be taken inferring physiological relevance.

For this reason, primary mouse leukaemic cells were investigated. Primary cells are often more difficult to work with due to their heterogenous nature and limited number, however, the data is of greater relevance as it is more representative to the *in vivo* environment[274]. These leukaemic cells (gifted by Dr Jasper de Boer, UCL) were generated by retroviral transfection of primary bone marrow cells (isolated from C57BI6.j mice) with *MLL-AF9.* The *MLL-AF9* fusion gene is one of the most common gene fusions associated with childhood AML and shared by the THP-1 cells[274].

Upon initially seeding mAF9 cells in gels at the lower of the two concentrations used for the cell lines (5×10^4/mL) seen in **Figure 4.1**, the mAF9 cells showed no proliferation in unmodified peptide gel as assessed visually with phase-contrast microscopy (data not shown). When seeded with the higher of the two concentrations (1×10^5/mL) a few cell clusters were formed by day 6 (**Figure 4.4,** condition 1). However, there were not enough cells to reliably count the number of cells using luminescence assays and the plate reader. This is especially important if these models are intended for drug screening, as the treatment would cause a decrease in cell number which would need to be monitored accurately.

Several methods for modifying the culture of mAF9 cells in peptide gels were therefore explored for the ability to increase proliferation. This included changing of seeding protocols, changing in media composition, and biochemically functionalising the gel (**Table 4.1**, **Figure 4.4**). The method used for adding matrix components to the precursor gel can be assumed to result in a homogeneous distribution in the final peptide gel as demonstrated in Ashworth et al[231].

Table 4.1: Conditions and modifications added to 6 mg/mL peptide gel for optimisation of mAF9 proliferation.

Condition #	Final cell concentration	Modifications or additions
1	$1 * 10^5$/mL	Cell suspension and media changes conducted with 0.5x media.
2	$2 * 10^5$/mL	Cell suspension and media changes conducted with 0.5x media.
3	$1 * 10^6$/mL	Cell suspension and media changes conducted with 0.5x media.
4	$1 * 10^5$/mL	Cell suspension and media changes conducted with 1x media.
5	$1 * 10^5$/mL	Addition of 20 % methylcellulose to peptide gel with 0.5x media.
6	$1 * 10^5$/mL	Addition of 10 µg/mL laminin with 0.5x media.
7	$1 * 10^5$/mL	Addition of 10 µg/mL fibronectin with 0.5x media.
8	$1 * 10^5$/mL	Addition of 50 µg/mL hyaluronan with 0.5x media.

To examine the effect of cell seeding concentrations on cell proliferation in peptide gels, 1×10^5/mL, 2×10^5/mL, and 1×10^6/mL were plated (conditions 1-3, respectively). To investigate the potential for reduced perfusion of growth factors through the gel, 1x media (condition 4) was used in replace of the 0.5x media used for all other conditions. Condition 5 explored the addition of methylcellulose, a semi-solid medium widely used for colony assays for haematopoietic cells. Conditions 6-8 examined the effect of additions of relevant matrix components, laminin, fibronectin, and hyaluronan on cell proliferation.

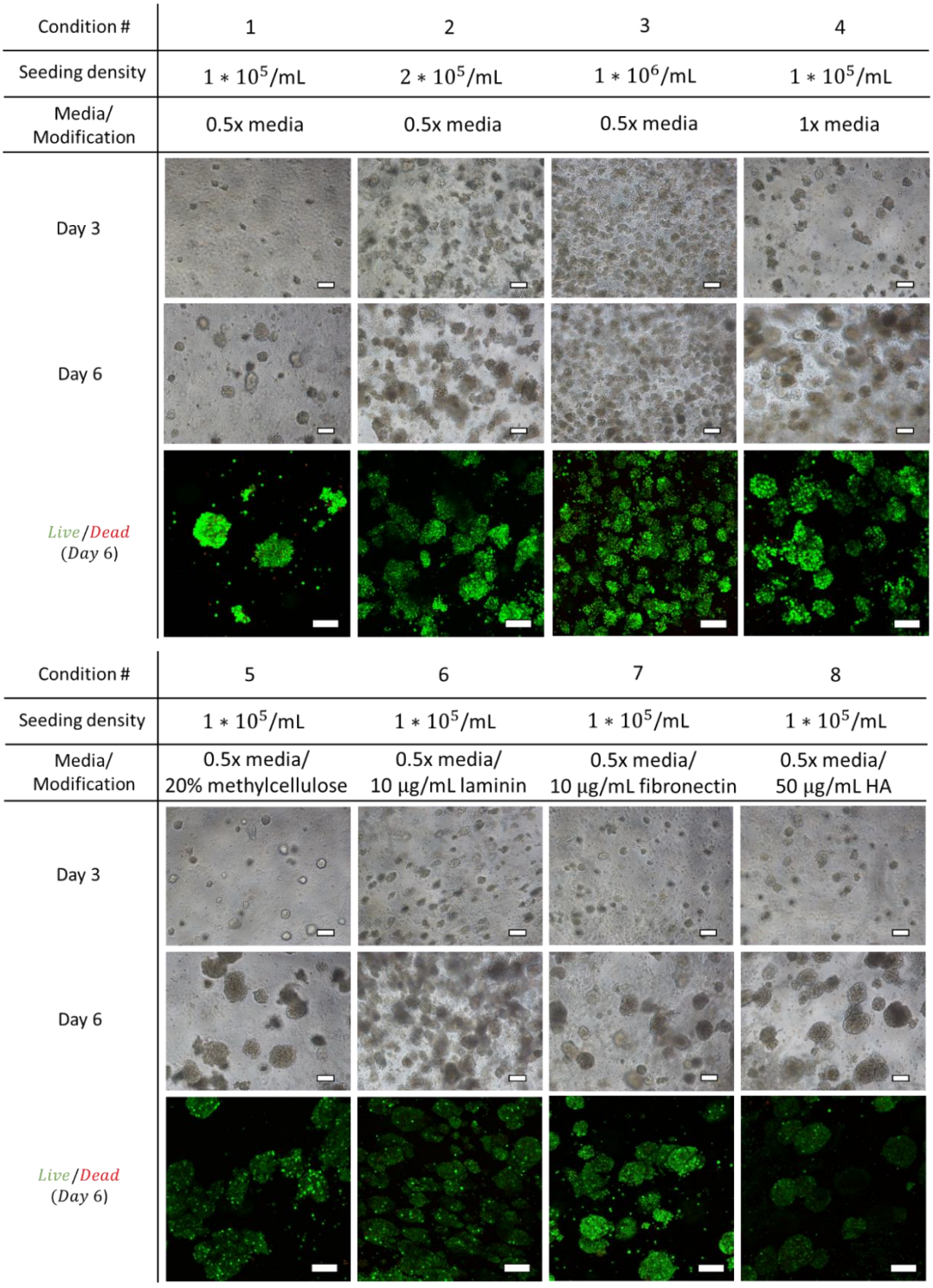


Figure 4.4: Phase contrast and confocal images of mAF9 cells in defined conditions of modified peptide hydrogels. *Confocal images were taken 6 days following initial seeding and stained with Calcein AM and Ethidium Homodimer-1 to indicate viability. N=2. Scale bars = 100 µm.*

4.6. iPSC derived HSPCs in peptide gels

An important function of the 3D models is not only to support leukaemic cell growth, but also healthy haematopoietic cells. This is required particularly for future assessment of drug screening on these models to quantify differential effects as well as crosstalk implications.

To investigate the ability to culture haematopoietic stem and progenitor cells with the peptide gels, iPSC derived hHSPCs were kindly donated by Emma Collins. HSPCs can form several types of colonies based upon the lineage of cell (erythroid, lymphoid, myeloid) and their maturity (e.g. myelocytes, promyelocytes, granulocytes, neutrophils and/or macrophages)[278]. Type I colonies are immature with dense centres, type II colonies are more mature and have dense centres surrounded by differentiating cells, and type III colonies are mature, diffuse colonies. These colony types are typically analysed using methylcellulose assays.

The hHSPCs were seeded into 6 mg/mL and 10 mg/mL peptide gels and cultured in the unmodified 3D environment for 7 days, producing several colonies in both 6 mg/mL and 10 mg/mL gels. These colonies varied in size and morphology, suggesting different colony types as produced by methylcellulose assays. **Figure 4.5** shows three examples of colonies formed in both concentrations of gel. **Figure 4.5bi. and iv.** could be suggestive of type I colony, showing a defined dense structure with no surrounding cells. **Figure 4.5bii. and v.** appear to have a dense centre with surrounding cells potentially differentiating suggestive of type II colonies. **Figure 4.5biii.** and potentially **vi**. appear much more diffuse, suggesting they could be the more mature type III colonies. It is worth noting that overall, the colonies are denser in the higher concentration gel as with the human cell lines.

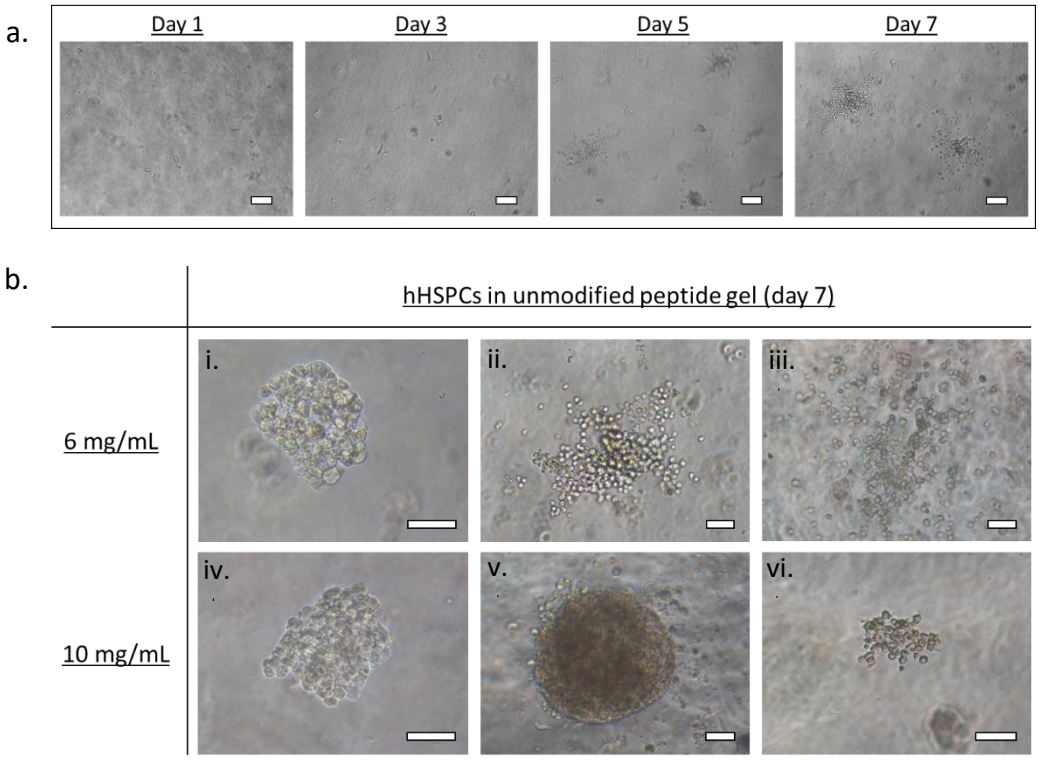


Figure 4.5: iPSC-derived hHSPCs in unmodified peptide gel. *iPSCs were differentiated to a haematopoietic lineage prior to seeding into peptide gels.* ***a****. Images were taken up to 7 days after initial seeding of the cells showing an approcimate doubling time of 24 h.* ***b****. Following 7 days of culture in the peptide gels the cells had proliferated in various colony types. Scale bars = 50 µm. N=1.*

Following 7 days of culture in gel, optical trapping was used to see if a single cell could be removed from a cluster. Although this result would not be quantitative for reasons discussed in (**chapter 3.7**), if it were possible, it could determine if the cell-cell interactions were weaker than for leukaemic cells. **Figure 4.6** shows that although a single cell could not be fully removed from the cluster, a few cells could be 'peeled' away from a large cluster of cells, suggesting the cell-cell interaction forces are weaker than for the leukaemic cells. As this proof-of-concept study of seeding hHSPCs into peptide gels was only an N=1, further repeats must be completed before concluding interaction force differences, especially as this is a heterogeneous cell population, many repeats should be analysed (N>50) and averaged.

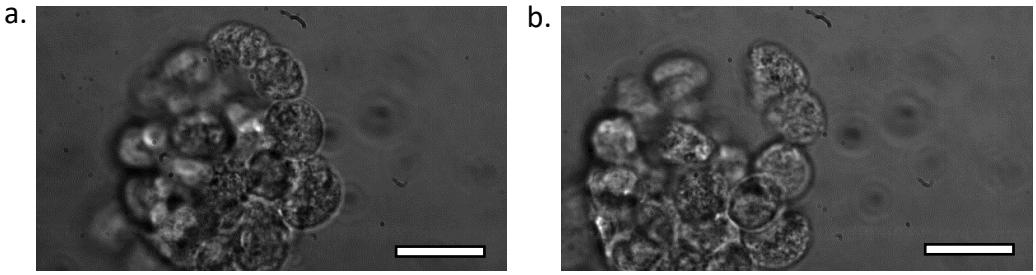


Figure 4.6: Optical manipulation of a cluster of iPSC-derived HPCSs in 6 mg/mL peptide gel a. *before and* ***b.*** *after movement with up to 250 mW laser power at sample. Scale bars = 100 µm*

4.7. Discussion

Several human leukaemic cell lines originating from varying lineages of AML were investigated for their ability to be cultured in the unmodified peptide gel. Two seeding densities of cells were explored, both forming clustered colonies of cells by day 6. From observation of the proliferation over the 6 days of culture, the cells formed colonies by division of a single cell, as opposed to migration of cells in the local microenvironment. It was found that if the cells were left to proliferate within the gel past day 7, the gel would lose mechanical stability, and thus made any following analysis impossible. This is believed to due to the cells rapidly colonising the peptide gel, physically forcing the peptide gel apart. We presented a higher seeding density of 5×10^5/mL with U937 cells in Ashworth et al[231]. Although this density was suitable for other cell types, such as mouse embryonic stem cells and human mammary fibroblasts, the U937 cells rapidly colonised the entire gel with separate colonies merging, limiting further proliferation by lack of space.

The ability to quantify the number of cells present in the peptide gel was imperative for future use of the models for drug testing. Although multiple methods were attempted, the use of luminescence assays gave accurate and repeatable results as determined by a plate reader (**Figure 4.2**). The values of luminescence were lower in peptide gels than in liquid culture, however, the assays showed linearly increasing trends with increasing cell number thus confirming the ability to quantify cell number by quantified luminescence. It is

important to note that these results were taken from a known number of individual cells (i.e. not colonies). As these cells form small loose clusters rather than overly large colonies (maximum 6 days of culture), the luminescence assays should reflect cell number through-out the experiments shown in this thesis. However, if using a different cell type that produces denser colonies, further experiments should be run to ensure accurate data readings as the cells proliferate.

Future work continuing from these results should also include quantification of perfusion of assays through the gel. Using transmitted light microscopy, it was observed that all of the leukaemic cell lines shown in **Figure 4.1** proliferated across the entire depth of the hydrogel. As this media contains molecules of a similar size to the luminescence viability assays explored in **Figure 4.2**, it is reasonable to assume the assays are able to penetrate throughout the depth of the gel. However, to quantify this molecular transport and explore how and if molecule size affects perfusion, future work could include a fluorescent assay (e.g. dextran or a protein size range) in combination with light-sheet microscopy for visualisation of permeation.

By increasing the amount of peptide powder during the initial stages of gel fabrication, the stiffness of the final gel was increased independently to chemical functionalisation. **Figure 4.3a** shows that the number and size of the colonies both decrease with increasing peptide gel stiffness. This could be due to compression of the surrounding gel by the colony expansion, causing too much mechanical pressure for the cells to continue proliferating. To explore this reasoning, a future experiment could include the investigation of the YAP/TAZ pathway. YAP and TAZ serve as co-transcription factors in mechanotransduction, and are an important signalling network connecting the mechanical signals from the ECM to intracellular signals[279]. Both the localisation (cytoplasmic or nucleus) and the level of expression of YAP/TAZ can be analysed for the impact of ECM stiffness on cell behaviour[280,281]. However, it is important to note that although the role of YAP/TAZ is relatively well-explored within 2D culture, much remains unknown of the role and regulation of the mechanotransduction pathways in 3D culture[282].

Quantitative analysis of cell number by RealTime-Glo™ MT viability assay agrees with images in **Figure 4.3a**, showing significantly more proliferation in 6 mg/mL gels than in higher concentrations of peptide gel (both 10 mg/mL and 15 mg/mL) 24 h following initial seeding. 6 mg/mL gels also produced significantly more proliferation than in 2D liquid culture. Confounded with the data in **chapter 2.2.2** which shows the 6 mg/mL peptide gel approaches physiological stiffness of bone marrow, these results justify 6 mg/mL gel use for future experiments investigating the haematopoietic and leukaemic niche.

In its unmodified form, the FEFEFKFK peptide gel allows cells to be encapsulated and cultured in a matrix-free environment. The unmodified peptide gel was successful for the culture of AML cell lines but upon using the same protocol (with relevant media) for mAF9s, colony proliferation was limited, with insufficient cell number for future drug screening analysis (**Figure 4.4**, condition 1). Protocol modifications used to increase mAF9 proliferation included varying cell number, media growth factors, and additions of methylcellulose, matrix proteins, and complex sugars (**Figure 4.4**).

To increase the proliferation observed in condition 1, conditions 2 and 3 explored the effect of altering the seeding density of the cells by 2x and 10x respectively. Increasing cell seeding number in the gels significantly improved cell growth. Doubling of the cell seeding density produces visibly more colony formation by day 6, showing a number of clusters similar to that seen by U937 cells at the same time point (see **Figure 4.1**). This option may be preferential for near-future work as it does not increase the matrix complexity of the peptide gel, and therefore does not form interactions with the cells which could affect their behaviour beyond the addition of the 3 dimensions. Further increased cell seeding density (10x) showed significant proliferation of cells up to day 3, however possibly due to space, proliferation does not appear to continue at the same rate up to day 6. At day 6 the cells are predominately viable; however, the growth did not exponentially increase as desired.

Condition 4 shows the effect of doubling the growth factor concentration in the media. This was investigated as upon adding the media on top of the gel we

have been assuming that the media fully perfuses through the gel and thus following media changes this results in an overall growth factor concentration of 0.5x. However, if we consider that the media may not be diffusing throughout the depth of the gel, the overall growth factor is halved by the dilution of the volume of the gel. For condition 4 the growth factor concentration of the media used for media changes on the gel was therefore doubled. This appeared to successfully promote more cell growth, producing a number of colonies visually similar to condition 2. Morphologically the colonies in condition 4 appear more rounded to previous conditions, suggesting the increase of growth factors has impacted how the cells responded to the 3D environment.

Condition 5 included the addition of 20 % methylcellulose to the peptide gel. Methylcellulose is a semi-solid medium widely used for colony assays for haematopoietic cells and contains growth factors to support leukaemic cell proliferation. Methylcellulose was selected as it is optimised for haematopoietic cell growth and as it is of a viscous nature, any alteration to the overall stiffness of the gel should be reduced. As can be seen in **Figure 4.4**, the addition of 20 % methylcellulose did alter the growth of the cells, showing less frequent but larger sized colonies than seen in the first 4 conditions. By day 6 of culture within this condition the cells appeared to be more towards the bottom of the gel, rather than distributed throughout the depth of the gel as seen for other conditions. This could be due to the size of the clusters acting under gravity.

Conditions 6, 7, and 8 show the additions of two relevant matrix proteins, laminin and fibronectin and the glycosaminoglycan (GAG) hyaluronan (HA). Laminin and fibronectin are two of the most prominent proteins in the bone marrow niche and have been shown to affect AML behaviours[283–286]. HA is expressed by the haematopoietic niche and has the potential to modify cell proliferation, migration, differentiation, and adhesion[287,288]. Concentrations of the additions were decided by previous dilutions explored by the Stem Cell Glycobiology group at the University of Nottingham. Future experiments should include a range of concentrations of these additions with the ideal concentration based off of proteomics or mass spectrometry data of intact bone marrow.

The additions of the matrix components seen in conditions 6, 7, and 8 in **Figure 4.4**, all increase cell proliferation as compared to condition 1, showing more cell clusters by day 6 of culture. Condition 8, in particular, produced more compacted and spherical clusters. It is important to note that by day 6 conditions 6, 7, and 8 showed gel contraction and lifting from the coverslip, as could be expected with the addition of cell-attachment motifs in contrast to the unmodified non-interactive gel[231]. The cells were still supported by the 3D peptide gel, however, as the cells were contracted within a smaller region as compared to the other conditions, it was difficult to take representative images of cell number within the cells. Despite this, it was apparent that the additions made in conditions 6-8 increase cell proliferation as compared to condition 1. Future work could include quantifying this proliferation using the luminescence assays introduced above.

It should be also noted that previous work published in Ashworth et al. showed changes in bulk rheology with additions of Matrigel and other matrix additions to the peptide gel[231]; which as shown in **Figure 4.3** can significantly affect leukaemic cell proliferation. For this reason, although collagen was initially considered as a matrix addition due to its abundance in the haematopoietic niche, it was not used in this study as it showed significant reduction of gel stiffness. Therefore, for future experiments, bulk rheology or microrheology should be completed on the peptide gel with matrix additions to explore any potential impact caused by gel stiffness changes.

Future modifications to increase the complexity of this model should include the addition of relevant cell types (see **Table 1.1**). Use of the peptide gels with transwells enables the inclusion of different cell types in direct co-culture or in-direct co-culture; where the first is defined as two cell types within the peptide gel in physical contact, and the latter is defined as in-direct contact, meaning although the two cell types are not occupying the same physical space, the cells can communicate by excreted factors through the mesh panel at the bottom of the transwell (**Figure 4.7**). An example of a relevant cell type for co-culture would be stromal cells. Stromal cells are present in the bone marrow and have been

shown to chemically signal leukaemic and haematopoietic cells affect their behaviours[168,289]. In this coupling, the in-direct co-culture may be more representative of *in vivo* mechanics as the stromal cells and HSPCs are not in direct contact *in vivo*.

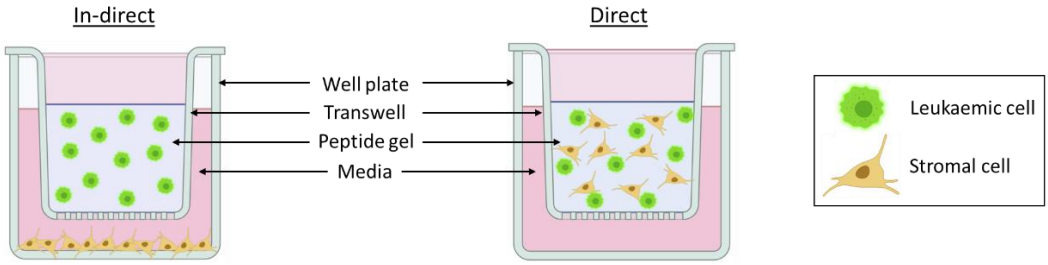


Figure 4.7: Schematic of direct and in-direct cell co-culture of leukaemic and stromal cells in peptide gel using transwells. *Figure created with BioRender.com.*

Due to the non-cancerous and less proliferative nature of the hHSPC cells derived from iPSCs, it was expected that these cells would require functionalisation of the peptide gel for cell growth. However, hHSPC proliferation was observed in both 6 mg/mL and 10 mg/mL unmodified peptide gels. As can be seen in **Figure 4.5a**, there were fewer colonies formed than previously observed from leukaemic cell growth, however, this was expected as HSPCs cannot be assumed to have the same ability to self-renew as a leukaemic cell. On the other hand, exceptionally, the cells capable of proliferation did so at a rate comparable to the leukaemic cells, producing colonies of ≈ 64 cells by day 7 of peptide gel culture. This means the cells followed a doubling time of ≈ 24 h, as supported by **Figure 4.5a** which shows clusters of 2 cells after 24 within peptide gels. This figure also shows that the colonies of hHSPCs within the peptide gel are formed by proliferation of a single cell rather than migration of cells to form a cluster. Upon future repeats of this experiment, the analysis should be performed on individual cell phenotypes to conclusively determine colony types. One method for this could be to harvest the colonies as conducted with colony-forming unit assays and perform phenotyping analysis using PCR or flow cytometry.

Optical trapping was performed on the hHSPC culture in 6 mg/mL peptide gel with the aim of manipulating the cell-cell interaction forces to determine any similarities or differences between haematopoietic and leukaemic cells. Although no statistical data can be taken from this study, we have successfully shown the ability to manipulate haematopoietic cells in 6 mg/mL peptide gels.

Overall, these results show that the octapeptide gel provides a versatile, easy-to-use 3D cell culture scaffold that can be incorporated into standard high-throughput screening operations for therapeutic analysis. We have shown the ability to individually modify the matrix stiffness and composition in a manner relevant to AML niche physiology, demonstrating the potential for future production of customised, bespoke, *in vitro* models. Future work following from these results should include increasing model complexity to improve recapitulation of *in vivo* AML, and investigation into FBS alternatives such as KnockOut Serum Replacement^{TM} (KSR) or other serum-free mediums for future translation as a fully defined AML/haematopoietic platform.

Chapter 5: Assessing the viability of leukaemic cells in response to FDA-approved drug treatments in 2D and 3D peptide gel models

5.1. Introduction and background

In the previous chapter, it was determined that unmodified peptide gels can support the culture of human leukaemic cell lines and primary mouse leukaemic cell line, mAF9. It was also shown that luminescence assays can enable high-throughput screening of cell viability within the peptide gels by use of a plate reader. This chapter exploits these findings to explore the capability of using the peptide gel as *in vitro* models for drug screening.

Previous literature has shown that the differences between the structure of 2D liquid culture models and 3D hydrogels can result in differential drug sensitivity, with 3D models more closely predicting the efficacy of the drugs *in vivo*[290–293]. By use of the novel peptide gels without matrix modifications, this chapter presents the impact of introducing a non-interactive structural support similar to the mechanical properties the cells are exposed to *in vivo*, while directly comparing the drug sensitivity to 2D liquid culture; enabling unique insight into the impact of mechanical cues independently to matrix interactions.

As previously explained in **chapter 1.2.3**, repurposed drugs are being increasingly investigated for cancer treatment to reduce the time, cost, and risks associated with getting a new treatment into clinical use[140]. The overall aim of this chapter was to therefore determine the ability of 4 FDA-approved drugs to eradicate AML cells in both liquid culture and in 3D peptide gel models. Due to the novel, matrix-free nature of the peptide gel, any changes in drug efficacy observed in comparison to liquid culture was solely due to the addition of 3D structure.

Figure 5.1 shows the schematic followed for this study. The five-point concentration drug screens (‘preliminary’ screens) within liquid culture were completed over a wide range of concentrations within a cohort of human AML cell lines and a primary mouse leukaemia cell line model to determine drug sensitivity. The initial screen was followed by nine-point concentration studies (‘extended’

screens) over a focussed range to more accurately determine the EC50 value. These EC50 drug concentrations were then used in the peptide gel models to compare how the cells react to the same drug concentration in 2D and within the non-interacting 3D models. Unfortunately, due to lack of time, the deformation analysis and combination treatment could not be completed within this thesis, however, these experiments are discussed in **chapter 6** for future consideration.

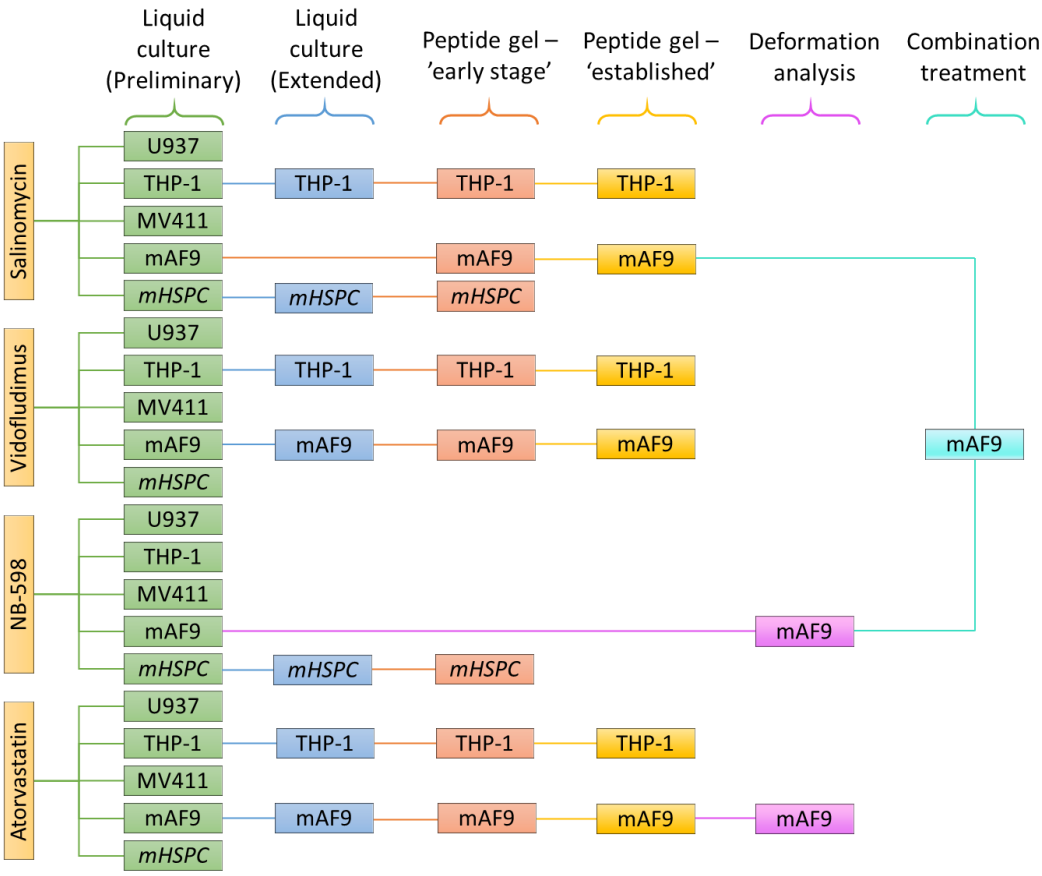


Figure 5.1: Schematic showing the process of drug screening from 2D liquid culture to 3D peptide gel models. *The decision of which drugs and cell types to continue into the next stage of experimentation was determined by the results collected in the previous experiment.*

5.2. EC50 of repurposed drug treated cells within liquid culture

5.2.1. Preliminary screens

Screening over a broad range of drug dosages was completed within liquid culture for human leukaemic cell lines (THP-1, U937, and MV411) and primary mouse leukaemic cell line (mAF9), introduced in **chapter 4.5**. Using RealTime-Glo™

MT metabolic assays, the cells were assessed for viability at 24 h, 48 h and 72 h after treatment with the drug of interest. Viability at these time points was recorded as percentage survival compared to cell viability of a vehicle control (DMSO) of the same concentration as within the highest drug concentration.

5.2.1.1. **Salinomycin**

Salinomycin (introduced in **chapter 1.2.3.1**) was chosen due to its previous success in the treatment of AML in Roulston et al.[142], and was therefore treated as a positive control for the liquid culture drug screening. However, the Roulston study did not include the THP-1 cells which share the *MLL-AF9* translocation of the mAF9 cells.

Figure 5.2a shows salinomycin to have a dose and time dependant effect on all cell types investigated, with all graphs demonstrating the 'S-shape' curve expected from positive drug screens. The mAF9 cells demonstrated the highest sensitivity to the drug, exhibiting an EC50 value of approximately 300 nM after 48 h of treatment. The EC50 values were at least doubled for the human cell lines, with EC50 values of approximately 3 µM, 1 µM, and 900 nM for THP-1, U937 and MV411 cells, respectively. Roulston et al. found EC50 values of 75 nM, 0.5 µM, and 1 µM for mAF9, U937 and MV411 cells, which approximately correlate to the values demonstrated in this study[142]. However, a more extensive screen using more drug concentrations over a smaller range was completed based on these results in order to gain a higher accuracy of EC50 value.

To confirm the accuracy of this method to determine cell viability, the U937 cells treated with salinomycin were visually analysed for viability using CellTox™ Green Cytotoxicity Assay and confocal microscopy **(Figure 5.2b)**. CellTox™ Green fluorescently stains dead cells and was representative of the quantitative analysis collected using RealTime-Glo™, displaying increasing cell death with increasing dosage.

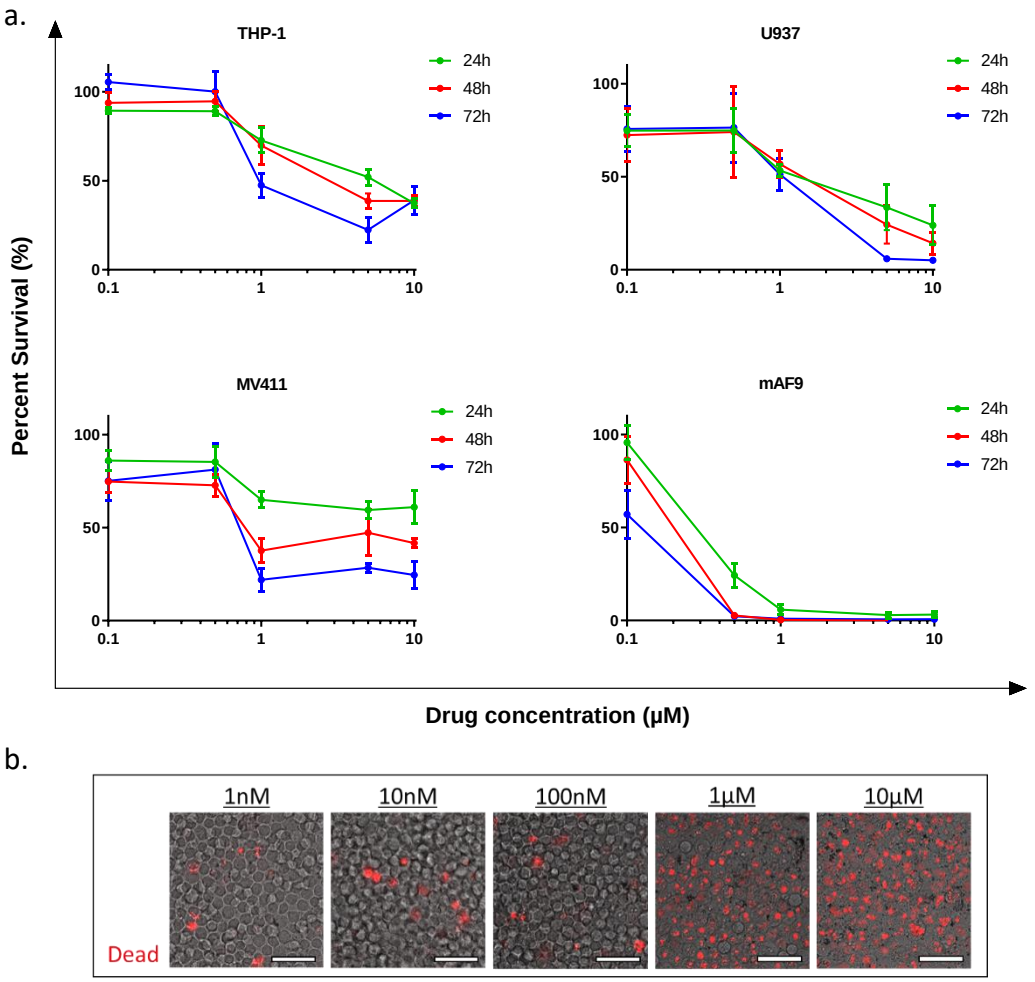


Figure 5.2: Salinomycin - Preliminary screens in liquid culture*. *a. *Line graphs showing viability of AML cells over time following treatment with salinomycin at the indicated dosage as compared to 0.2 % DMSO vehicle control. Mean values ± standard deviation of biological replicates (N=3, n=3) are plotted throughout.* ***b.*** *Confocal images of U937 cells 72 h treatment with salinomycin. CellTox™ Green was used to highlight dead cells. Scale bars = 50 µm.*

5.2.1.2. **Vidofludimus**

Vidofludimus (introduced in **chapter 1.2.3.1**) was selected due to current interest in DHODH inhibitors in clinical trials for other cancer types, however, to our knowledge, this is the first investigation of vidofludimus on leukaemic cells. Treatment of the AML cells with vidofludimus displayed a varied effect across the cell types.

U937 cells did not exhibit dose or time dependent viability, instead showing a consistent viability decrease to approximately 60 % of the DMSO control across all dosages and time points (**Figure 5.3**). This unusual response could not

be explained as a toxicity effect from the DMSO as a vehicle control was used. For this reason, U937 cells treated with vidofludimus continued into an extended screen to confirm this unconventional finding.

MV411 and THP-1 cells showed a decrease in viability with increasing dosage, however, the latter did not achieve EC50 values within the range of concentrations investigated. Vidofludimus had the greatest effect on the mAF9 cells, demonstrating an approximate EC50 value of 5 µM at 48 h.

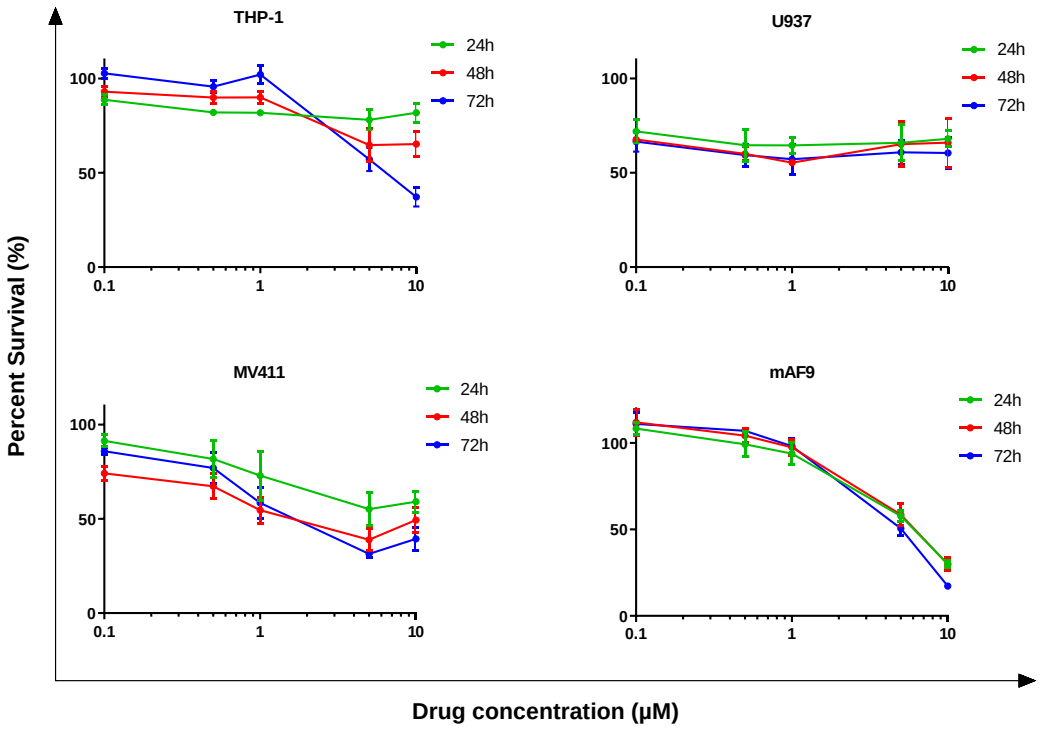


Figure 5.3: Vidofludimus - Preliminary screens in liquid culture. a. *Line graphs showing viability of AML cells over time following treatment with vidofludimus at the indicated dosage as compared to 0.2 % DMSO vehicle control. Mean values ± standard deviation of biological replicates (N=3, n=3) are plotted throughout.*

5.2.1.3. **NB598**

NB598 (introduced in **chapter 1.2.3.1**) is an anti-cholesterol drug selected due to its success in a preliminary study investigating the effects of cell membrane stiffness with drug treatment (performed by Aishah Mustapha and discussed further in **chapter 6.2**). However, despite the prediction that the stiffness of the cell could correlate with cell viability, **Figure 5.4** shows that NB598 did not affect

the viability of any cell type investigated in the dose and time-dependant manner expected of a potential therapeutic treatment.

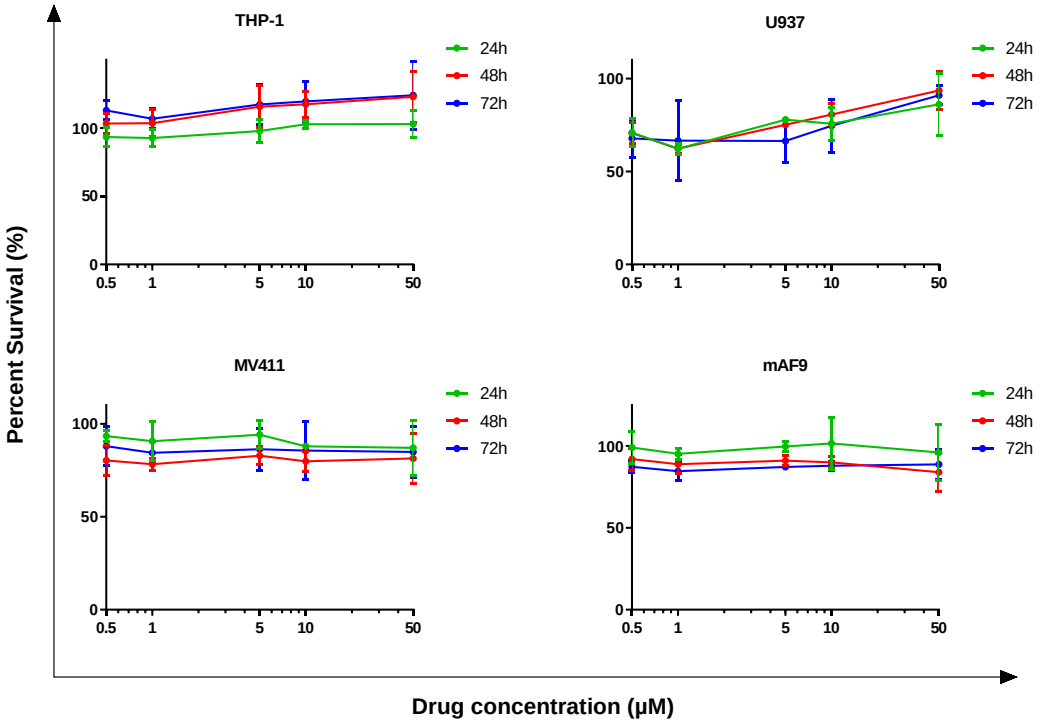


***Figure 5.4: NB598 - Preliminary screens in liquid culture**. **a.** Line graphs showing viability of AML cells over time following treatment with NB598 at the indicated dosage as compared to 0.2 % DMSO vehicle control. Mean values ± standard deviation of biological replicates (N=3, n=3) are plotted throughout.*

5.2.1.4. **Atorvastatin**

Atorvastatin (introduced in **chapter 1.2.3.1**) was the second anti-cholesterol drug explored in this study, providing a comparative statin to NB598. Although NB598 and atorvastatin act via different pathways (as described in **chapter 1.2.3.1**), the drugs both act to reduce the amount of cholesterol within the cell membrane potentially leading the biophysical change in membrane stiffness as seen in preliminary results.

In contrast to NB598, atorvastatin treatment resulted in a time and dose dependant reduction in viability across all cell types investigated (**Figure 5.5**). Based on these graphs the mAF9 cells displayed the highest sensitivity to the drug with an EC50 value of ≈ 2 µM after 48 h of treatment. The human leukaemic cell

lines THP-1, U937, and MV411 presented with EC50 values of approximately 2.5 µM, 6 µM, and 3 µM respectively at 48 h. With treatment of 50 µM of atorvastatin for 72 h all AML cell types were effectively eradicated, including the heterogeneous mAF9 population.

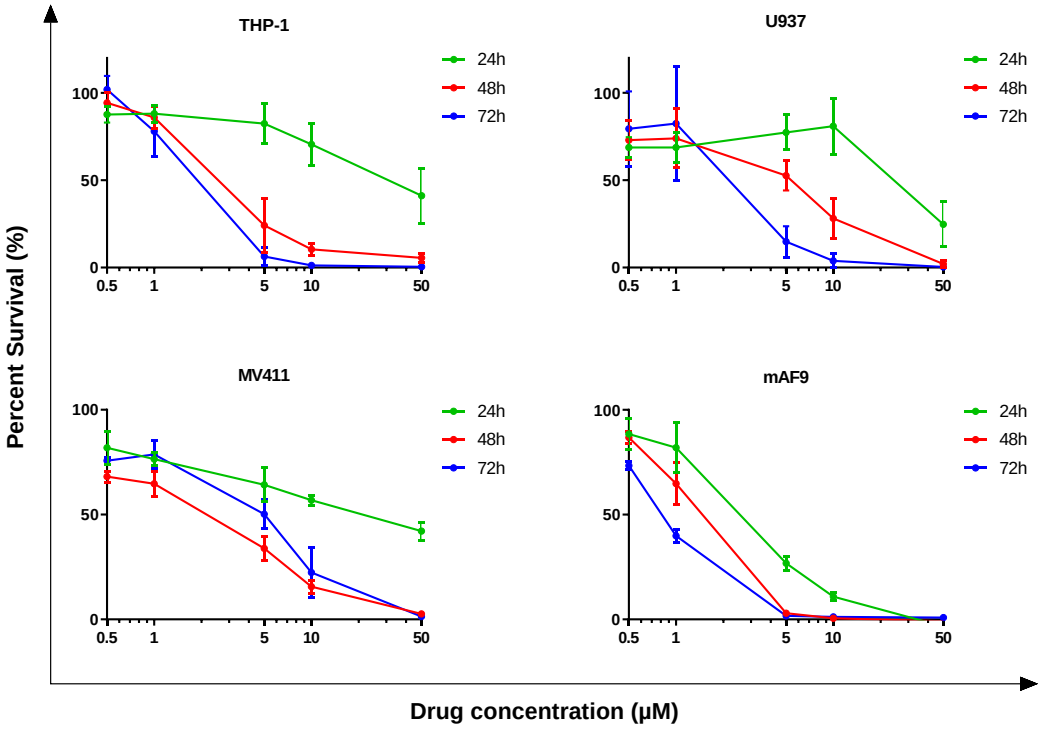


Figure 5.5: Atorvastatin – Preliminary screens in liquid culture. a. *Line graphs showing viability of AML cells over time following treatment with atorvastatin at the indicated dosage as compared to 0.2 % DMSO vehicle control. Mean values ± standard deviation of biological replicates (N=3, n=3) are plotted throughout.*

5.2.2. Extended drug screens

5.2.2.1. Selection criteria for extended EC50 analysis

To obtain more precise EC50 values for application into the peptide gel models, a subset of the drugs shown have an anti-leukaemic response in the preliminary screens were investigated within an extended screen over a 9-concentration range. Anti-leukaemic drug responses were defined as; i. Reduction of percentage survival at or below 50 % at least at 72 h, ii. Demonstration of survival decrease with increasing dosage, iii. Demonstration of increasing sensitivity over time. From this definition, anti-leukaemic drugs as determined by the preliminary screens were selected as summarised below (**Table**

5.1). Based on these criteria, the NB598 did not continue into the extended screen. Extended EC50 assays were thus completed for salinomycin, vidofludimus, and atorvastatin using the THP-1 and mAF9 cells.

Table 5.1: Efficacy of repurposed drugs on leukaemic cells based upon preliminary drug screens. *Where one, two, or three ticks represents a loss of 50 % cell viability after 24 h, 48 h, and 72 h respectively. A cross represents no visible cell death occurred as compared to DMSO control.*

	Salinomycin	Vidofludimus	NB598	Atorvastatin
U937	✓✓✓	×	×	✓✓✓
THP-1	✓✓✓	✓	×	✓✓✓
MV411	✓✓	✓✓	×	✓✓✓
mAF9	✓✓✓	✓✓✓	×	✓✓✓

5.2.2.2. **THP-1 cells**

As indicated within the preliminary screen, **Figure 5.6** confirms all three drugs in the extended screen provide a time and dose dependant response on the THP-1 cells.

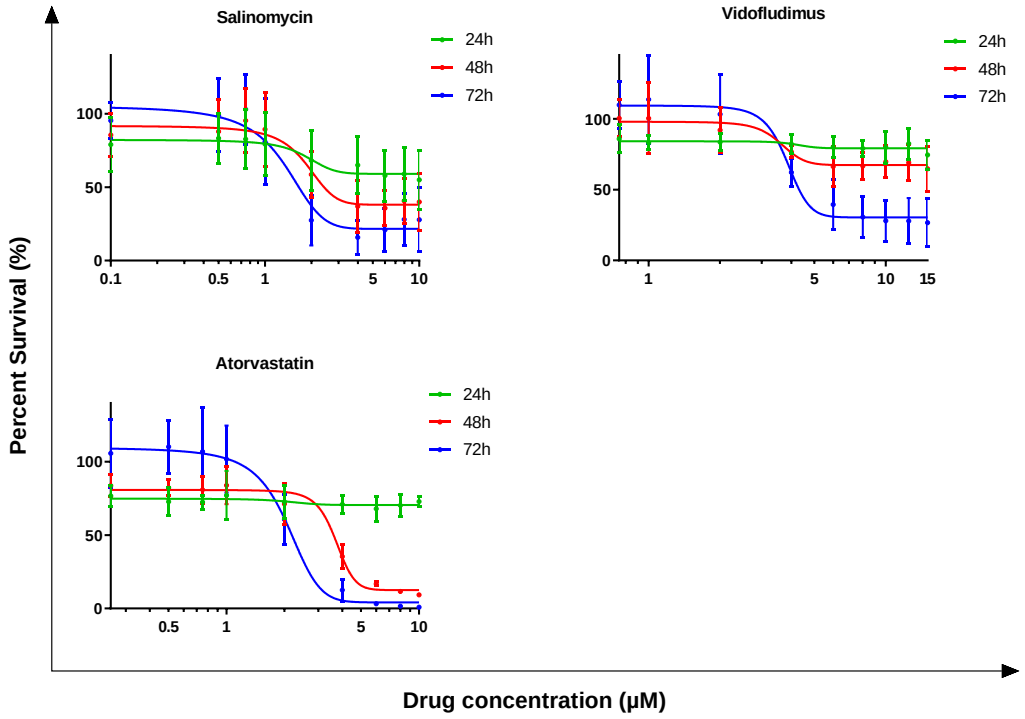
Salinomycin demonstrated EC50 values at the lowest drug concentrations, producing an EC50 value of 1.865 (± 0.319) µM at 48 h. Although THP-1 cells were not reported by Roulston et al.[142], this value is similar to the EC50 value of the MOLM-13 cells which carry the same translocation as the THP-1 cells (≈ 1 µM at 48 h). As Roulston et al. showed no haemotoxicity at these effective concentrations, this result supports the need for further investigation of salinomycin as a targeted AML therapy.

In agreement with the preliminary screen, vidofludimus did not achieve an EC50 value at 48 h in the extended analysis. However, at 72 h an EC50 value of 3.829 (± 0.222) µM, was achieved, a value reflective of the preliminary EC50 collected from **Figure 5.3**.

In contrast to the preliminary screen with atorvastatin, **Figure 5.6** shows atorvastatin not to have a dose-dependent effect on THP-1 cell viability until 48 h

after drug addition. Nonetheless, the EC50 value of 3.686 (± 0.132) µM at 48 h was very similar to the value predicted by the preliminary screen, exhibiting minimal error between biological repeats as shown by small standard deviation on the data points. Also, similarly to the results above, at the highest concentration (10 µM) atorvastatin reduces the viability of the THP-1 cells to 0.83 (± 0.23) % following 72 h of treatment.

a.



b.

EC50 values (µM)	Salinomycin	Vidofludimus	Atorvastatin
24 h	-	-	-
48 h	1.87 (± 0.32)	-	3.69 (± 0.13)
72 h	1.34 (± 0.27)	3.83 (± 0.22)	2.07 (± 0.15)

Figure 5.6: Extended screens in liquid culture with THP-1 cells. ***a.*** *Graphs showing viability of AML cells over time following drug treatment at the indicated dosage as compared to 0.2 % DMSO vehicle control. Mean values ± standard deviation of biological replicates (N=4, n=3) are plotted throughout.* ***b.*** *EC50 values and uncertainty determined using GraphPad Prism nonlin fit agonist vs. response – variable slope (four parameters).*

5.2.2.3. **mAF9 cells**

From the preliminary drug screen, it was expected that the mAF9s would demonstrate lower EC50 values as compared to the THP-1 cells. As can be seen in **Figure 5.7**, salinomycin demonstrated markedly lower EC50 values in mAF9 cells of 138.0 (± 6.0) nM at 48 h. From Roulston et al., a value of 75 nM was required to achieve 50 % mAF9 cell death at 48 h with salinomycin[142]. This is a relatively small

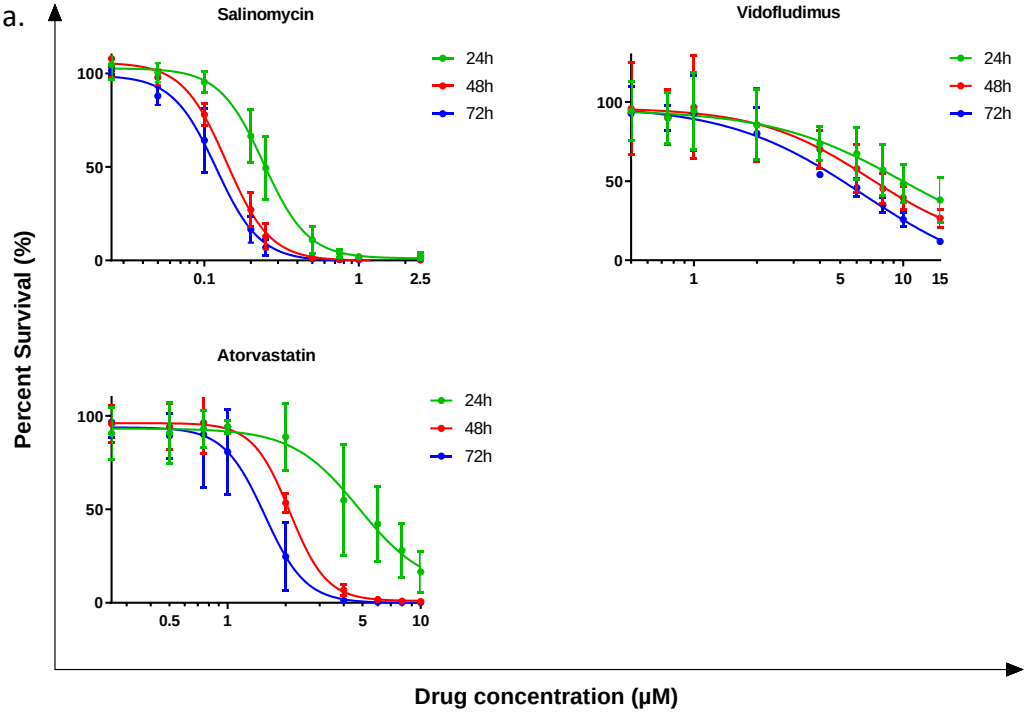
difference that could have occurred from the batch of the drug or, most likely, due to the different strain of mAF9 cells.

When treated with 2.5 µM salinomycin over 24 h or above the mAF9 cells were effectively eliminated, further confirming the potential of salinomycin as a targeted AML treatment.

By 48 h of vidofludimus treatment, mAF9 cells achieved 50 % viability loss with an EC50 value of 6.888 (± 5.201) µM. Due to the non-standard shape of the curves produced by the vidofludimus treatment (as opposed to the typical 'S-shaped' curves observed with the other two drugs) the standard deviation of the EC50 values as determined by the GraphPad software were unusually large. Nonetheless, from the vidofludimus graph in **Figure 5.7** the EC50 values recorded are representative of the data collected.

As suggested by **Figure 5.5** at 10 µM, the anti-cholesterol drug atorvastatin reduced cell viability to 0.65 (± 0.18) % by 48 h of treatment with 10 µM. As also observed with the salinomycin treatment, this shows the ability of atorvastatin to eliminate all cells within the primary mAF9 cell line population. The EC50 at 48 h was 2.099 (± 0.091) µM, a value significantly lower than that observed for the THP-1 cells.

a.



b.

EC50 values (μM)	Salinomycin	Vidofludimus	Atorvastatin
24 h	0.24 (± 0.01)	9.96 (± 18.2)	4.79 (± 1.52)
48 h	0.14 (± 0.01)	6.89 (± 5.20)	2.10 (± 0.09)
72 h	0.12 (± 0.01)	6.43 (± 3.49)	1.56 (± 0.16)

Figure 5.7: Extended screens in liquid culture with mAF9 cells. a. *Graphs showing viability of mAF9 cells over time following drug treatment at the indicated dosage as compared to 0.2 % DMSO vehicle control. Mean values ± standard deviation of biological replicates (N=4, n=3) are plotted throughout.* ***b.*** *EC50 values and uncertainty determined using GraphPad Prism nonlin fit agonist vs. response – variable slope (four parameters).*

5.2.2.4. **U937 cells**

Due to the unusual response of the U937 cells to vidofludimus treatment shown in **Figure 5.3**, an extended dose response assay was completed in order to confirm the efficacy. Mirroring the previous result, the extended study demonstrated a consistent loss of viability to approximately 60 %, independently of dosage or time of treatment (**Figure 5.8**). This could suggest a very wide

therapeutic margin, and therefore the dosage range observed is within the plateau region of the drug response. This is supported by the finding that vidofludimus required a higher dosage to achieved 50 % viability as compared to the other drugs investigated. As this affect was only observed with the U937 cells which were selected for this study as a comparator cell line of a different translocation, this unusual result can be considered to be a cell line specific response to this drug.

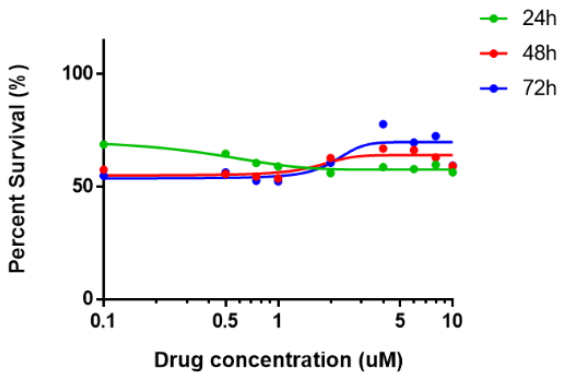


Figure 5.8: Extended screen of vidofludimus in liquid culture with U937 cells. a. *Graph showing viability in mAF9 cells over time following treatment with vidofludimus at the indicated dosage as compared to 0.2 % DMSO vehicle control. Mean values of biological replicates (N=1, n=3) are plotted.*

5.3. Comparison of EC50 values in 2D and 3D models

To compare the sensitivity of the drugs in 2D liquid culture to 3D peptide hydrogel models, the EC50 values found in **chapter 5.2.2** were applied to 6 mg/mL peptide gels. This was investigated using two methods to recapitulate 'early-stage' AML and 'established' AML (**Figure 5.9**). The 'early-stage' model was achieved by treating the cells with the repurposed drugs on the same day after initial seeding (leaving 1 h for the gel to reach temperature equilibrium). This meant that the cells were in an individual state, mimicking the morphology of AML that has yet to proliferate and establish itself within the bone marrow. The 'established' AML model was achieved by seeding the cells within the peptide gels and allowing them to proliferate within the gels for 72 h prior to the addition of drug treatment. This meant that the cells had formed clusters of ≈ 8 cells before exposure to drugs. These two models were used under the hypothesis that the proliferation of the

cells in the 'established' model would recapitulate cell colonies present in a more established AML. This is supported by Duarte et al. and Hérault et al., who showed that as AML progresses, it colonises the bone marrow niche as defined clusters[99,294].

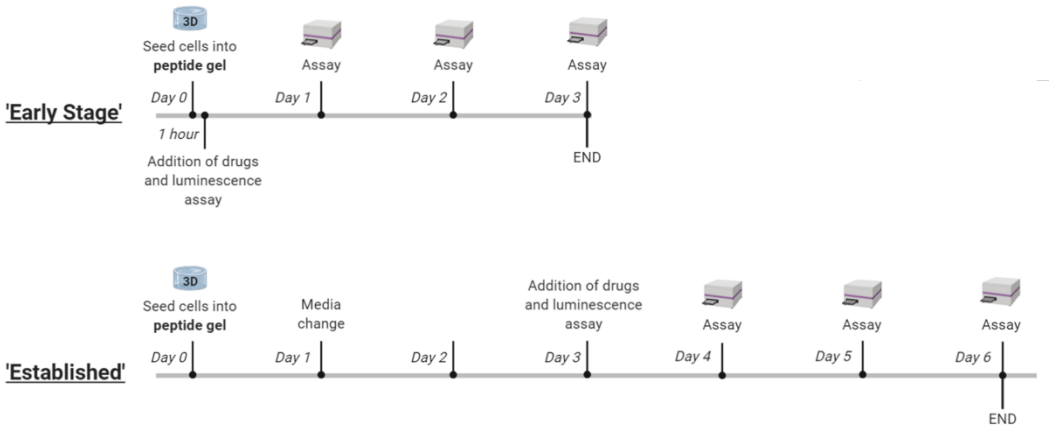


Figure 5.9: Schematic showing methods and timings of drug treatments and analysis in 'early-stage' and 'established' AML 3D peptide gel models. *Created with BioRender.com.*

For application into the peptide gel models, the EC50 values of THP-1 cells treated with repurposed drugs were gathered from **Figure 5.6b** (48 h for salinomycin and atorvastatin, 72 h for vidofludimus) and cell viability in the peptide gels were collected using the RealTime-Glo™ assay. Due to the matrix-free, non-interactive nature of the peptide gel, it could be concluded that any differences between the drug efficacy measured in liquid culture and peptide gels was purely the result of the addition of the 3D structure.

5.3.1. 'Early-stage' AML model

Drug testing in 3D peptide gel models was performed by using the EC50 values of the drug as informed by the extended screens. Salinomycin demonstrated an EC50 value of 51.2 (± 5.88) µM at 48 h in peptide gels, suggesting the drug to have a very similar effect on the cells in 3D peptide gels and liquid culture (**Figure 5.10a**). However, upon observation of the efficacy of salinomycin at different time points as shown in **Figure 5.10d**, it can be seen that unlike liquid culture which showed an increase in cell death over treatment time, in the peptide

gels, the cell population reduced to 50 % viability by 24 h and remained at this percentage for up to 72 h of treatment. This lack of time dependency suggests that although the EC50 values are similar in the different mediums, the process of cell death may vary.

Treatment of vidofludimus in liquid culture as compared to peptide gel revealed a large, statistically significant difference (**Figure 5.10b**). Within peptide gels, vidofludimus demonstrated very low sensitivity, with a cell viability of 98.7 (± 5.08) % after 72 h of treatment as compared to vehicle control.

Atorvastatin also showed a significant difference in sensitivity between the liquid culture and peptide gel, demonstrating a lower sensitivity in the latter with a cell viability of 78.0 (± 7.54) % following 48 h of treatment (**Figure 5.10c**). However, in contrast to vidofludimus, **Figure 5.10d** revealed atorvastatin to produce a time-dependant response, decreasing the cell viability over treatment duration.

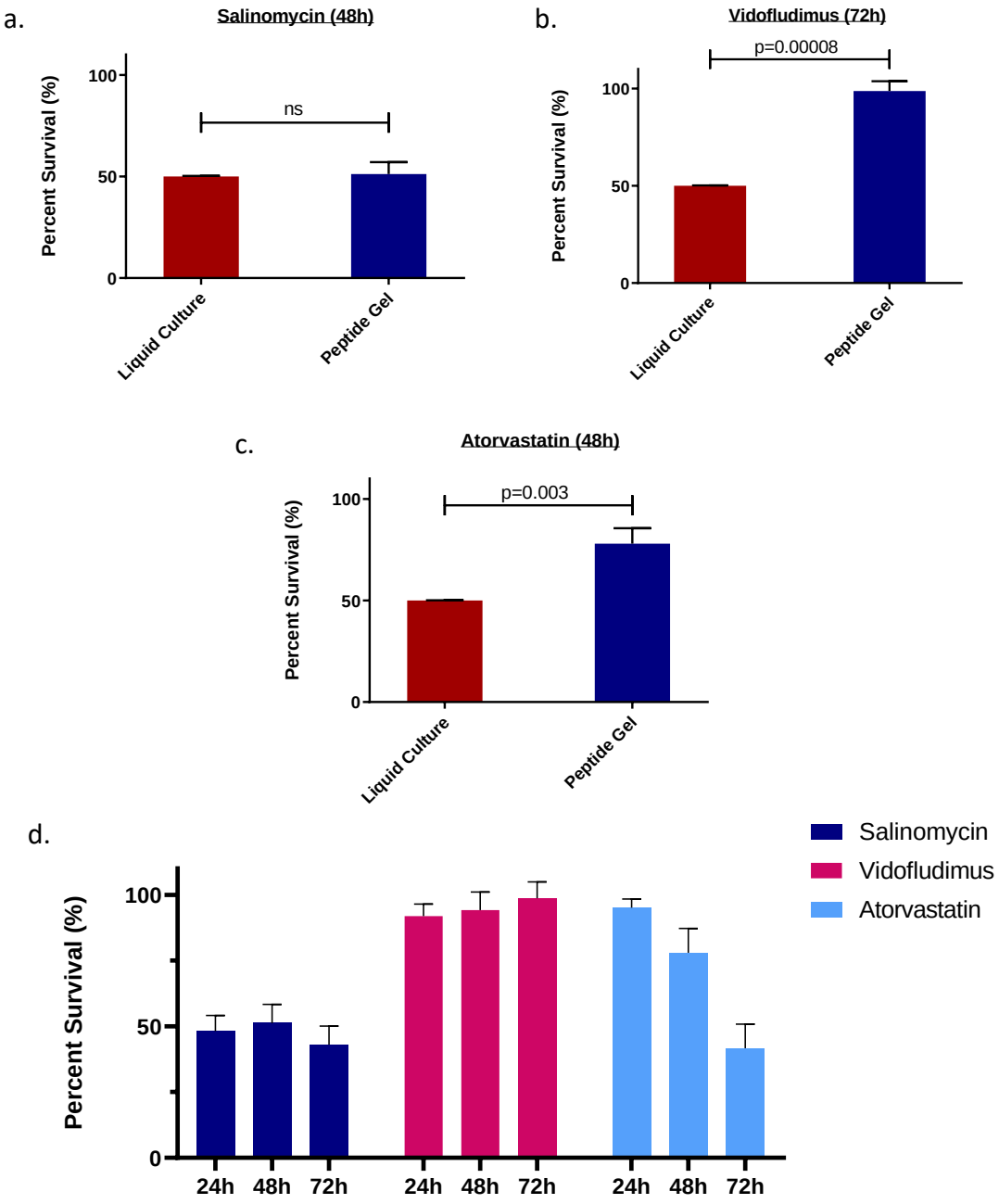


Figure 5.10: THP-1 cells treated with salinomycin, vidofludimus, and atorvastatin in 3D 'early-stage' 6 mg/mL peptide gel models. a-c. *EC50 values as determined by the extended screens in liquid culture compared to efficacy of the same dosage with 3D 'early-stage' peptide gel models.* ***d.*** *Bar graphs displaying time dependency of treated THP-1 cells over 72 h after drug addition to 'early-stage' peptide gel models. For all results, mean values ± standard deviation of biological replicates (N=3, n=3) are plotted with values and uncertainty determined using GraphPad Prism nonlin fit agonist vs. response – variable slope (four parameters). All results presented as percentages compared to vehicle (DMSO) control of 0.02 %.*

5.3.2. 'Established' AML model

Within the 'established' peptide gel model, salinomycin and vidofludimus demonstrated cell viability values within a similar range of those produced by the 'early-stage' model (**Figure 5.11a, Figure 5.11b**). Also, in agreement to the 'early-stage' models, **Figure 5.11d** revealed no significant decrease in cell viability over increasing treatment time of either salinomycin or vidofludimus.

In contrast, the 'established' AML models produced a significantly differing response to atorvastatin as compared to the 'early-stage' models. The 'early-stage' model investigated in **Figure 5.10** demonstrated the EC50 value of THP-1 cells with atorvastatin in peptide gels to be higher than in liquid culture, whereas the 'established' 3D model **Figure 5.11c** shows the EC50 value to be lower than in liquid culture. This indicates a significant difference in drug response due to colony formation. In **Figure 5.11d** it can also be seen that atorvastatin produced a time-dependent response, reducing cell viability to ≈ 14.6 % by 72 h of treatment; a value comparable to liquid culture over the same time period (≈ 20 % at 72 h).

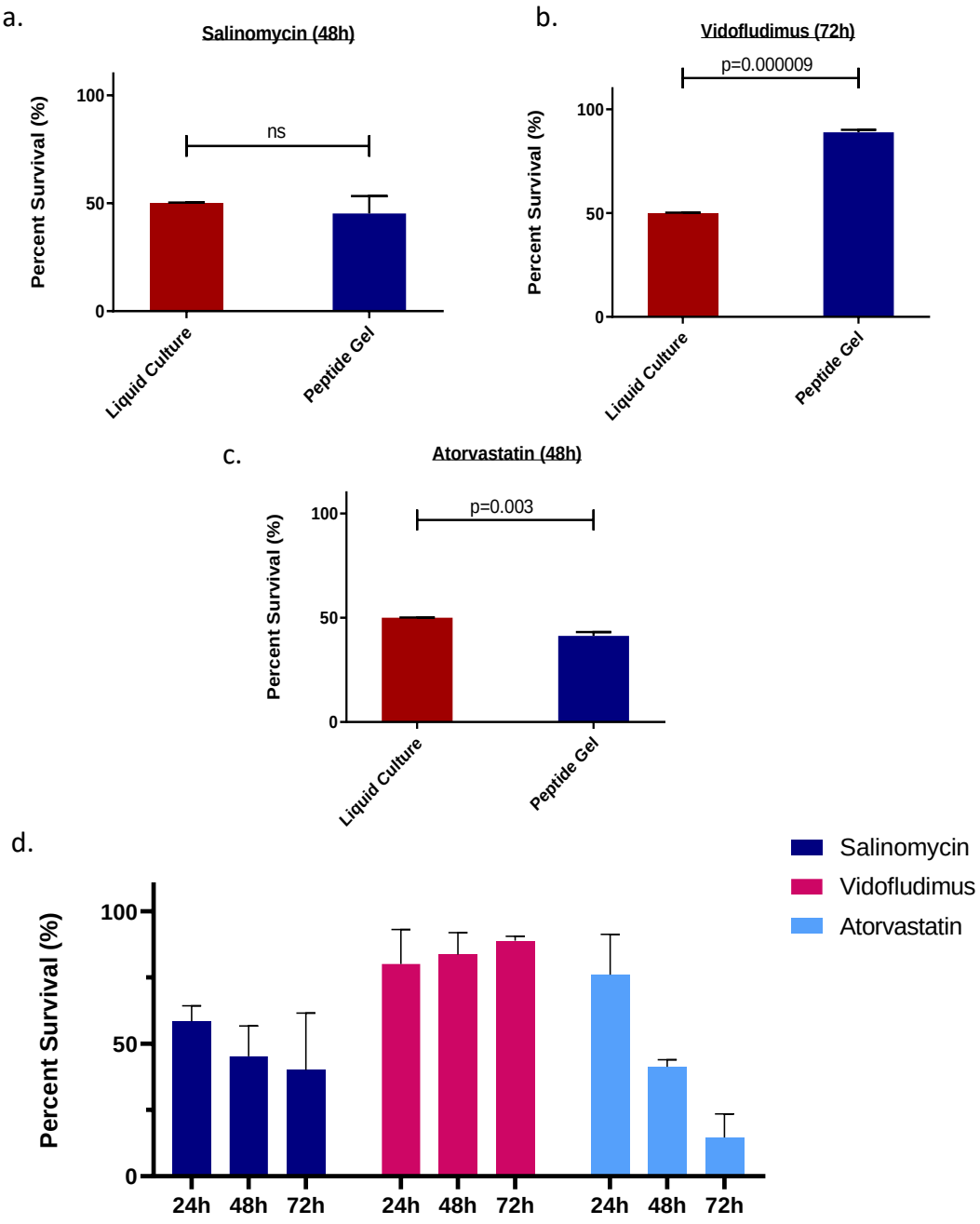


Figure 5.11: THP-1 cells treated with salinomycin, vidofludimus, and atorvastatin in 3D 'established' 6 mg/mL peptide gel models. a-c. *EC50 values as determined by the extended screens in liquid culture compared to efficacy of the same dosage with 3D 'established' peptide gel models.* ***d.*** *Bar graphs displaying time dependency of treated THP-1 cells over 72 h after drug addition to 'established' peptide gel models. For all results, mean values ± standard deviation of biological replicates (N=3, n=3) are plotted with values and uncertainty determined using GraphPad Prism nonlin fit agonist vs. response – variable slope (four parameters). All results presented as percentages compared to vehicle (DMSO) control of 0.02 %.*

5.4. Discussion

Development of pathophysiologically relevant *in vitro* cancer models for drug discovery is one of the major challenges facing researchers in the desire to improve the low translation of therapies into clinic[2,3]. This study presented for the first time a defined peptide gel model free of matrix motifs to examine the impact of 3D structure on AML cell sensitivity to drug treatments. This novel approach enabled direct comparison of AML treatment response of repurposed drugs in liquid culture and non-interactive 3D peptide gel, providing unique insight into the importance of mechanical cues within AML models.

All of the drugs investigated, with the exception of NB598, caused cell death in all AML cell types examined. Direct comparison of liquid culture and 3D peptide gel models showed varied drug sensitivities related to drug type, cell line, dosage, time of treatment and between the 'early-stage' and 'established' models.

Overall, there are four main reasons to consider as to why the cells may respond different in the peptide gels as compared to liquid culture. This first is that of drug permeation through the peptide gel. Impediment of drug permeation through the full depth of the gel could arise due to the molecular weight physically affecting the drugs ability to travel through the structure. However, as all of the drugs used in this study were of a significantly lower molecular weight than molecules previously used in the peptide gels (e.g. IGG antibodies for ICC ≈ 50 kDa is significantly greater than salinomycin (751 Da), vidofludimus (355 Da), and atorvastatin (559 Da)), this was determined not to be applicable. A further impediment to permeation of the drugs could be due to electrical charge. If the peptide gel and the drug hold electrical charge this could cause resistance in diffusion. Although, as the net change of the peptide gel is 0 at neutral pH (calculated using Innovagen peptide property calculator[295]) this can also be dismissed as a factor.

The second is that due to the gel-like nature of the peptide gel, unlike liquid culture there is no free flow, meaning that if the cells produce any matrix or waste products will remain within the local area of the cells creating an enriched environment which could affect their behaviours. In support of this consideration,

Dias et al. showed that leukaemia cells secrete a number of cytokines that can serve as autocrine signals[296]. Autocrine signalling induces different cell behaviours depending on the concentrations of factors present and thus could change the cells' drug response[297].

Similarly, a further factor could be due to the formation of cell colonies. This hypothesis is supported by a recent finding from Monteiro et al[298] who show that in hydrogel-based 3D models, randomly distributed osteosarcoma cells display inherent physiological and drug response variances as compared to aggregated cells. In this study the aggregated cells are of much greater number and density than used in the 'established' models presented here. However, it does support importance of evaluating different cellular aggregation states. The final reason for observing any differences in drug efficacy between liquid culture and peptide gel is that the peptide gel could be affecting intracellular signalling pathways. This will most likely be via integrin-based signalling or mechanically gated ion channels[299–303].

The data presented regarding the application of salinomycin as an AML treatment correlated with and expands upon the work in Roulston et al[142]. This chapter demonstrated the capacity of salinomycin to induce AML cell death in both liquid culture (showing a similar EC50 to that presented in Roulston et al.), and in 3D peptide gels. Within this study, salinomycin was the only drug to exhibit a similar EC50 value in all 3 models investigated (liquid culture (2D), 'early-stage' gel, and 'established' gel) (**Figure 5.10**, **Figure 5.11**). From these results, two conclusions could be considered; i. the 3D structure of the gel did not significantly influence the drug perfusion or have a biological impact on the cells, or ii. the 3D structure affected both the delivery of the drug and had a biological impact on the cells, but the effects were balanced which resulted in a similar EC50 value. Without further testing a definitive conclusion cannot be determined, however the ability to observe a similar amount of cell death in the two environments is a promising first step towards establishing the peptide gels as an *in vitro* model for drug testing. Coupled with the data presented by Roulston et al.[142], in particular the

lack of toxicity of normal haematopoietic cells at relevant drug concentrations, demonstrates salinomycin to be an attractive candidate for targeting AML.

The extended drug screens showed vidofludimus to produce an EC50 value of 3.83 (± 0.22) µM in THP-1 cells in liquid culture at 72 h. Upon applying this value into peptide gel culture, a significant reduction in cell death was observed as compared to the liquid culture at the same timepoint ('early stage' p=0.0008, 'established' p=0.000009). This agrees with previous literature using different hydrogel models which have shown the 3D environment to influence biological behaviours[16,46,174,175], however, this would be the first time this influence has been able to be observed for AML cells within a matrix motif-free model.

In contrast to the application of vidofludimus in liquid culture, in peptide gel vidofludimus did not show any reduction of cell viability over time (**Figure 5.10, Figure 5.11**). With respect as to why a difference in vidofludimus efficacy may have been observed between the liquid culture and peptide gel models, we must consider the potential reasons stated above; the cells creating an enriched environment, the impact of colony formation, or due to impacted integrin or mechanical ion gated based signals. From previous literature it suggests that the formation of ECM (enriched environment) and increased colony size creates a protective environment[304–306]. This correlates with the vidofludimus results which show a decreased efficacy within the peptide gel models. However, if these were the sole reasons for this difference, we may expect a greater difference in drug efficacy between the 'established' and 'early stage' peptide gel models due to the time given for proliferation and ECM formation prior to addition of the drugs. Furthermore, as the reasons stated above are not mutually exclusive, there could also be intracellular signalling involvement. To explore this hypothesis, inhibitors could be used on mechanotransduction pathways (e.g. blebbistatin[307]) and the experiment could be repeated to see if the difference in drug efficacy still occurs. If the variation in drug efficacy still occurs, it can be concluded that intracellular signalling pathways are affected by mechanical cues, and could be a step towards finding an ECM target for future AML treatments.

In contrast to vidofludimus, atorvastatin demonstrated time and dose dependency across both 3D models (**Figure 5.10d, Figure 5.11d**). Upon applying the EC50 value of 3.69 (± 0.13) µM from the THP-1 cells in liquid culture into the 'early-stage' peptide gel model, significantly less cell death was observed. However, the opposite was seen within the 'established' peptide gel models with significantly more cell death as compared to liquid culture. These results therefore show that the relatively short time period over which the cells were culture prior to addition of drug treatment (72 h), significantly changes their response to drug treatment in a manner reflective of previous literature which suggests the ECM/colony formation creates a protective environment for the cells. This finding supporting the conclusion of Monteiro et al. regarding the importance of the investigation of different cellular aggregation states[298], and suggests that the production of ECM (enriched environment) and/or the formation of cell colonies, plays a significant role in atorvastatin efficacy. However, as this magnitude of variation was not observed for vidofludimus it is unlikely to be the sole explanation. Therefore, as described above for vidofludimus, in order to confirm this future work should explore the potential involvement of intracellular pathways.

Overall, this study showed the efficacy each drug to vary in a different manner in the 'early stage' and the 'established' peptide gel models as well as compared to liquid culture. These significant differences suggest the variation observed to be due to mechanism of action of the drugs and how this changes in response to the addition of the 3D architecture. As each drug acts through a different pathway, the impact of the 3D architecture will be different for each drug, therefore explaining the variation in liquid culture vs peptide gel response observed in this study; an observation and conclusion made possible by the novel, non-interacting peptide gel. Imminent future work should, therefore, include analysis on each model to determine the method by which each drug is acting between liquid culture and peptide gel model. Ideally, these results should also be repeated *in vivo* and compared to see if the peptide gel models are more representative to *in vivo* data than liquid culture. This would provide evidence of

the representative capabilities of the peptide gel model and provide further insight into the necessity of including tissue-relevant mechanical cues in AML models.

Of closest relevance to the drug testing completed in this thesis is a study published by Shin and Mooney in 2016, where they used an alginate gel crosslinked with calcium sulphate[111]. Using these gels, they explored the effect of Arg-Gly-Asp (RGD) integrin ligand density, showing the increase of RDG to significantly increase the proliferation of MOLM-14 cells. Upon drug treatment of MOLM-14 cells in their 3D models they found the sensitivity of the cells to depend on the presence of RGD, revealing an absence of RGD to abolish the differences in drug sensitivity as compared to 2D standard culture. This contrasts with the results we have provided which show a non-interacting 3D model to significantly impact drug sensitivity as compared to 2D liquid culture. However, this could be because although Shin and Mooney produced a hydrogel without RDG, the alginate gels were formed using calcium meaning they cannot be considered matrix motif-free and could have influenced cell behaviour. Despite this, they did successfully demonstrate the increase of binding motifs to affect AML cell dynamics, therefore highlighting the importance of the peptide gel used in this thesis.

As a result of lab closures due to SARS-CoV-2, drug response of mAF9 cells in peptide gels was not investigated, however, this should be highly considered for a future experiment as a more representative platform towards primary cell application.

Overall, this study provides the first step towards using the peptide gels for *in vitro* drug discovery and development in AML; coupled with the data presented in **chapter 4**, we show the future ability to increase the complexity of the composition of the peptide gel to better represent the *in vivo* environment. Results presented in this chapter suggest salinomycin, vidofludimus and atorvastatin to be promising future therapeutics for the treatment of AML.

Chapter 6: Future Work

From the highly multi-disciplinary work presented in this thesis, there are many branches from which future studies could be continued.

In **chapter 3** we presented the novel application of microrheology within unmodified peptide gels. This technique opens many doors for examining the microenvironment in real time, which could be of interest for a wide range of tissues to examine cell behaviour and disease progression. In particular, as inert polystyrene beads and cells can be seeded as a co-culture within the peptide gel (**Figure 3.15c**), this technique could explore the changes in the microenvironment of cells during proliferation. This would provide valuable information on how the cells physically alter the properties of their local environment, a characteristic that has not yet been able to be explored at this scale. Additionally, as this technique is non-contact, a future aim could also be to perform microrheology *in vivo*. This would be a valuable experiment as it would enable observation and quantification of any heterogeneities of the *in vivo* microenvironment, for informing future production of a physiologically accurate *in vitro* model.

Chapter 4 demonstrated the ability to increase complexity of the peptide gel models by the addition of relevant matrix components. The next generation of AML peptide gel models should address the complexity of the bone marrow ECM, including matrix proteins, GAGs, and multicellularity. As discussed in **chapter 4.7**, the stromal cells within the bone marrow have been shown to greatly affect the behaviour of haematopoiesis and leukemogenesis and could be included in direct or indirect co-culture. However, in order to produce models recapitulating tissue-realistic cell behaviour *in vitro*, future modifications should include bone marrow niche constituents such as multiple cell types, ECM components, soluble factors, and physio-chemical factors such as hypoxia and pH regulation (**Table 1.2**). Ideally, these additions and their concentrations should be guided by proteomic or mass spectrometry data of in leukaemic bone marrow to best mimic the *in vivo* niche. Furthermore, to address the vascularisation of the bone marrow niche, the peptide gel models could be used with microfluidic systems to recapitulate shear flow.

Chapter 5 introduced a schematic of plans for investigating the use of re-purposed drugs to eliminate AML cells in peptide gel models (**Figure 5.1**). As mentioned, not all the experiments presented in the schematic were able to be completed due to lab closures. Below are two of the experiments that would be beneficial to conduct following the work in this thesis.

6.1. Extraction and application of mHSPCs

The testing of drugs on healthy cells is a requirement for any treatment aiming for clinical application, especially cancer. As discussed in **chapter 1.2.3**, currently used treatments such as chemotherapy and radiotherapy are unable to selectively target the cancerous cells, causing damage to the patients haematopoietic and immune system by loss of healthy cell types in the bone marrow. For repurposed drug treatments researchers, therefore, aim for targeted application towards cancer stem cells and progenitors.

For direct comparative analysis, the non-malignant comparator following this work should be haematopoietic cells from the same source. For this reason, a future experiment should include the extraction of bone marrow cells from the same mouse type as used for the production of the mAF9 cells (C57BI6.j mice) followed by selection for mouse HSPCs (mHSPCs) using a lineage depletion kit (**Figure 6.1**). Once the mHSPCs are collected they would be expanded using methylcellulose followed by liquid culture and taken through the same experimental process of drug screening as used for the leukaemic cells in **chapter 5**. The drugs' efficacy would be directly compared between the cell types with the aim that the dosages of drugs that causes leukaemic cell death would not significantly affect the mHSPCs, creating a therapeutic window.

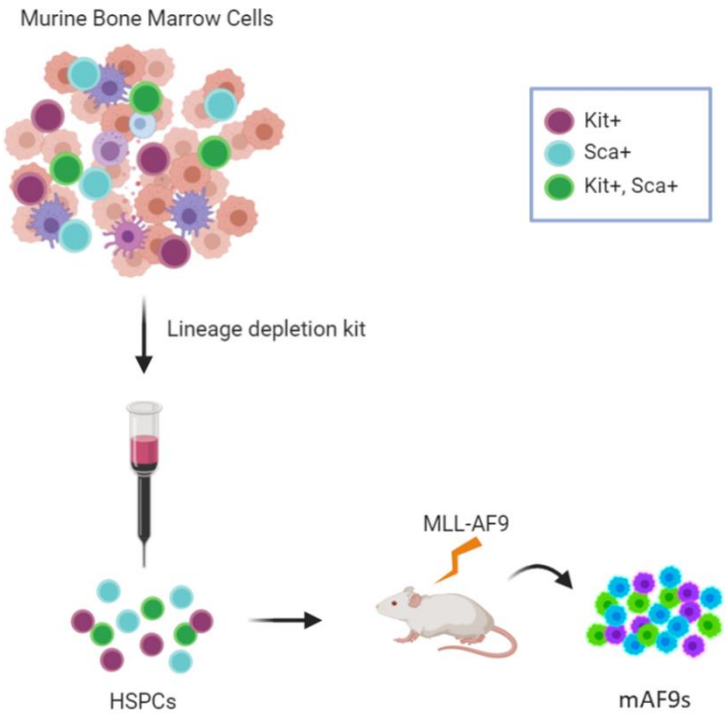


Figure 6.1: Schematic summarising the extraction of HSPCs from murine bone marrow and how they enable direct comparative analysis to the mAF9 cells used in this thesis. *Figure created with BioRender.com.*

One potential complication of this process could be that due to the non-malignant nature of the HSPCs, proliferation within the peptide gels may require optimisation of the culture conditions prior to conducting drug testing. This would be of heightened concern as compared to the leukaemic cells due to their limited number. However, in **Figure 4.5**, we showed the proliferation and maintenance up to 7 days of iPSC-derived HSPCs without requirement of matrix additions. This shows promise for the future of non-cancerous cell expansion in the unmodified peptide gels and provides a template for short/mid-term toxicity-based studies.

6.2. Cell deformation with optical tweezers

Continuing from the experimental process summarised in **Figure 5.1**, a further valuable future experiment to perform would be to quantify and compare the deformation, or mechanical properties of leukaemic and haematopoietic cells before and after drug treatment. The physical property of cell stiffness has been

shown to greatly affect the biological activity of cells in terms of general function and disease progression[308–310]. However, despite the suggestion that chemotherapy exposure increases leukaemic cell stiffness[311], the relationship between AML cell stiffness and cancer treatment efficacy has yet to be fully explored.

This study would build on this finding and would be separated into two main aims: 1. To create an automated method of using the optical tweezers to perform live cell deformation measurements on the microscale, and 2. To measure AML cell stiffness before and after treatment with NB-598 (a drug found to not cause AML cell death (**chapter 5.2**) but preliminary experiments have shown it to affect cell stiffness (**Figure 6.4**)). The cells would then be treated with a drug known to cause AML cell death (e.g. salinomycin) and cell viability would be monitored. The hypothesis of this would be that the decrease in cell stiffness would increase the efficacy of the salinomycin, with the future aim of exploiting any correlation that could exist between cell stiffness and drug efficacy for future drug treatments.

Cell stiffness can be measured using optical tweezers by the deformation of a cell under flow. In this technique the cell of interest is held stationary using an optical trap and the sample stage is moved at a constant velocity. This motion results a drag force acting upon the cell due to the relative flow to the surrounding medium, causing the cell to deform (**Figure 6.2**).

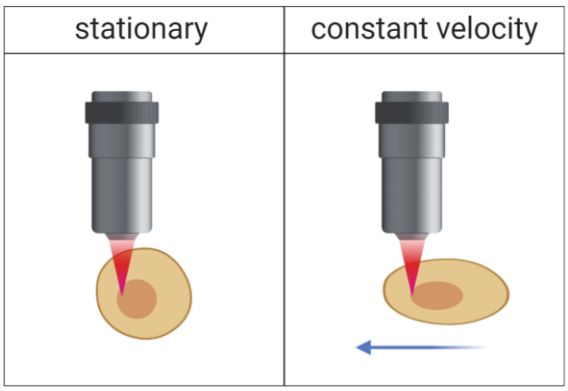


Figure 6.2: Schematic showing how optical tweezers can be used to deform cells. *Blue arrow indicates the direction of movement of the cell with respect to the fluid flow of the surrounding medium. Created with BioRender.com.*

This technique is currently being developed by the Optics and Photonics Group at the University of Nottingham, with the aim of creating an automated analysis program based in MATLAB for the detection and measurement of cell deformation. This software will function by thresholding the individual frames and recording of the deformation by identifying the outline of the cell (**Figure 6.3a**.) The deformation is then quantified using the Taylor deformation parameter. The Taylor deformation parameter, D, is the ratio between the difference and the sum of the major and minor axes and is calculated using[312],

$$D = \frac{x - y}{x + y} \qquad \text{Eq. 15}$$

where x is the major axis of deformation, and y is the minor axis of deformation (**Figure 6.3b**).

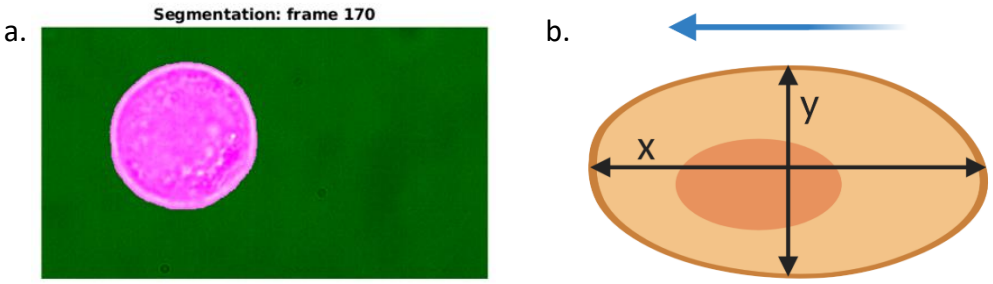


Figure 6.3: Figures displaying how the automated analysis software identifies and quantifies cell deformation. a. *Example image of an optically trapped mAF9 cell with fitted overlay by the MATLAB program. The overlay (shown in pink) is fitted to each frame of the recording and the software automatically calculates the deformation parameters, highlighting the frames of maximum and minimum deformation. Data collected with the help of William Hardiman.* ***b.*** *Schematic of optically deformed cell showing the major and minor axes of deformation, x and y respectively, as measured for calculation of the Taylor deformation parameter. Blue arrow indicates the movement of the cell with respect to the surrounding material.*

A further parameter that will be observed during deformation is cell area. The cell area should be stable through-out deformation and will act as a control to ensure the results are accurate and reliable.

Experimental parameters to consider upon approaching this technique include: the acceleration of the sample stage, the speed of sample stage relative to the trapped cell, and the time over which the movement occurs. If the acceleration of flow relative to the trap exceeds the trapping strength, the cell will

disassociate from the optical trap before constant speed is achieved. In a similar manner, the final speed of the movement must be sufficient as to cause deformation but not too high as to discard the cell from the trap. This value should therefore be determined by increasing the speed until the cell is discarded; the value used should then be the speed just below this to ensure maximum deformation. Finally, the time over which the motion occurs must be long enough for the cell to achieve maximum deformation.

A further important experimental consideration is the number of cells of which data is collected. Although minimal within cell lines, when considering using this technique with primary cell types it is critical to recognise the heterogeneity of the cell population. Primary cell types vary in biological and physical characteristics which will greatly affect single-cell analysis techniques. It is therefore necessary to average the deformation properties over a large number of cells within the same population to ensure reliable comparison between cell types.

Preliminary work was conducted by Aishah Mustapha using MV411 and HL60 AML cell lines and revealed the successful application of the optical tweezers to perform and quantify cell deformation (**Figure 6.4**). The cells were treated with anti-cholesterol drug, NB598 and the deformation analysis was performed before and after treatment. The post-processing was conducted manually through MATLAB software and revealed a reduction in cell stiffness of both cell lines following exposure to NB598.

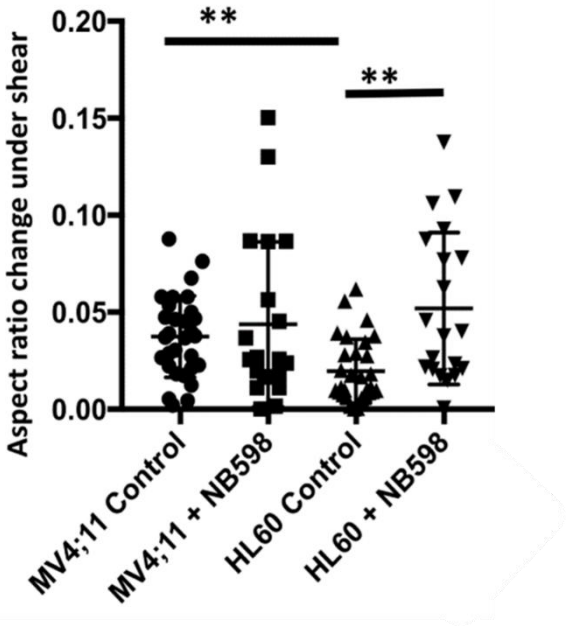


Figure 6.4: Deformation of AML cell lines using optical tweezers (performed and analysed by Aishah Mustapha). *N=20. **P < 0.01.*

Overall, this technique of using optical trapping of live cells would not only quantify previously unknown biophysical properties of leukaemic cells in response to FDA-approved drugs, but also potentially initiate a novel data library of how these biophysical properties relate to drug efficacy. This methodology would require significantly fewer cells compared to biological phenotyping assays and may provide an increased understanding of how current therapies act against cancer.

Chapter 7: Conclusions

It is widely recognised that improvement of treatment efficacy for cancer is dependent upon an increased understanding of underlying biological mechanisms. As the field of cancer research continues to acknowledge the overwhelming limitations of 2D cell culture and current gold standard animal models, research requires mechanically and biochemically defined and adjustable synthetic models in which to improve drug acceptance into the clinic.

Using a wide range of techniques, this thesis has explored the use of a synthetic self-assembling peptide hydrogel (FEFEFKFK) of modifiable composition and viscosity to model the bone marrow niche for investigation of the impact of dimensionality on leukaemia proliferation and response to drug treatment. This novel approach enabled direct comparison of AML treatment response to repurposed drugs in liquid culture and in 3D *in vitro* models free from matrix motifs, providing unique insight into the importance of mechanical cues within AML models. Future work continuing from these results aims to develop an improved mechanistic understanding of 3D models in drug repurposing and resistance, with the target to develop 3D peptide gels for patient-derived tissue.

References

1. Cancer Research UK. https://www.cancerresearchuk.org/health-professional/cancer-statistics/worldwide-cancer (2020).
2. Lacombe, D. & Liu, Y. The future of clinical research in oncology: where are we heading to? *Chinese Clin. Oncol.* **2**, 10 (2013).
3. Das, V. *et al.* Pathophysiologically relevant in vitro tumor models for drug screening. *Drug Discov. Today* **20**, 848–855 (2015).
4. Wong, S. W., Lenzini, S. & Shin, J. W. Perspective: Biophysical regulation of cancerous and normal blood cell lineages in hematopoietic malignancies. *APL Bioeng.* **2**, (2018).
5. Kiel, M. J. & Morrison, S. J. Uncertainty in the niches that maintain haematopoietic stem cells. *Nat. Rev. Immunol.* **8**, 290–301 (2008).
6. Seita, J. & Weissman, I. L. Hematopoietic stem cell: self-renewal versus differentiation. *Wiley Interdiscip. Rev. Syst. Biol. Med.* **2**, 640–53 (2010).
7. Mendelson, A. & Frenette, P. S. Hematopoietic stem cell niche maintenance during homeostasis and regeneration. *Nat. Med.* **20**, 833–46 (2014).
8. Boulais, P. E. & Frenette, P. S. Making sense of hematopoietic stem cell niches. *Blood* **125**, 2621–9 (2015).
9. Pelham, R. J. & Wang, Y. L. Cell locomotion and focal adhesions are regulated by substrate flexibility. *Proc. Natl. Acad. Sci. U. S. A.* **94**, 13661–13665 (1997).
10. Jordan, C. T. The leukemic stem cell. *Best Pract. Res. Clin. Haematol.* **20**, 13–8 (2007).
11. Yu, Z., Pestell, T. G., Lisanti, M. P. & Pestell, R. G. Cancer stem cells. *Int. J. Biochem. Cell Biol.* **44**, 2144–2151 (2012).
12. Lane, S. W., Scadden, D. T. & Gilliland, D. G. The leukemic stem cell niche: current concepts and therapeutic opportunities. *Blood* **114**, 1150–7 (2009).
13. Ye, H. *et al.* Leukemic Stem Cells Evade Chemotherapy by Metabolic Adaptation to an Adipose Tissue Niche. *Cell Stem Cell* **19**, 23–37 (2016).
14. Chaudhuri, O. *et al.* Extracellular matrix stiffness and composition jointly

regulate the induction of malignant phenotypes in mammary epithelium. *Nat. Mater.* **13**, 970–978 (2014).

15. Zanetti, C. & Krause, D. S. “Caught in the net”: the extracellular matrix of the bone marrow in normal hematopoiesis and leukemia. *Exp. Hematol.* **89**, 13–25 (2020).
16. Chaudhuri, O., Cooper-White, J., Janmey, P. A., Mooney, D. J. & Shenoy, V. B. Effects of extracellular matrix viscoelasticity on cellular behaviour. *Nature* **584**, 535 (2020).
17. Kirkham, G. R. *et al.* Precision Assembly of Complex Cellular Microenvironments using Holographic Optical Tweezers. *Sci. Rep.* **5**, 8577 (2015).
18. Andersson, M. *et al.* Using optical tweezers for measuring the interaction forces between human bone cells and implant surfaces: System design and force calibration. *Rev. Sci. Instrum.* **78**, 074302 (2007).
19. Foo, J. J., Liu, K. K. & Chan, V. Viscous drag of deformed vesicles in optical trap: Experiments and simulations. *AIChE J.* **50**, 249–254 (2004).
20. McAlinden, N., Glass, D. G., Millington, O. R. & Wright, A. J. Accurate position tracking of optically trapped live cells. *Biomed. Opt. Express* **5**, 1026–37 (2014).
21. Neuman, K. C. & Block, S. M. Optical trapping. *Rev. Sci. Instrum.* **75**, 2787–809 (2004).
22. Falleroni, F., Torre, V. & Cojoc, D. Cell Mechanotransduction With Piconewton Forces Applied by Optical Tweezers. *Front. Cell. Neurosci.* **12**, 130 (2018).
23. Ericsson, M., Hanstorp, D., Hagberg, P., Enger, J. & Nyström, T. Sorting out bacterial viability with optical tweezers. *J. Bacteriol.* **182**, 5551–5 (2000).
24. Zhong, M.-C., Wei, X.-B., Zhou, J.-H., Wang, Z.-Q. & Li, Y.-M. Trapping red blood cells in living animals using optical tweezers. *Nat. Commun.* **4**, 1768 (2013).
25. Barak, P., Rai, A., Rai, P. & Mallik, R. Quantitative optical trapping on single organelles in cell extract. *Nat. Methods* **10**, 68–70 (2013).

26. Wang, M. D., Yin, H., Landick, R., Gelles, J. & Block, S. M. Stretching DNA with optical tweezers. *Biophys. J.* **72**, 1335–46 (1997).

27. Khalili, A. A. & Ahmad, M. R. A Review of Cell Adhesion Studies for Biomedical and Biological Applications. *Int. J. Mol. Sci.* **16**, 18149–84 (2015).

28. Glass, D. G., McAlinden, N., Millington, O. R. & Wright, A. J. A minimally invasive optical trapping system to understand cellular interactions at onset of an immune response. *PLoS One* **12**, e0188581 (2017).

29. Crick, A. J. *et al.* Quantitation of malaria parasite-erythrocyte cell-cell interactions using optical tweezers. *Biophys. J.* **107**, 846–53 (2014).

30. Birbrair, A. & Frenette, P. S. Niche heterogeneity in the bone marrow. *Ann. N. Y. Acad. Sci.* **1370**, 82–96 (2016).

31. Ng, A. P. & Alexander, W. S. Haematopoietic stem cells: past, present and future. *Cell Death Discov.* **3**, (2017).

32. Boisset, J.-C. & Robin, C. On the origin of hematopoietic stem cells: Progress and controversy. *Stem Cell Res.* **8**, 1–13 (2012).

33. Ogawa, M. Differentiation and Proliferation of Hematopoietic Stem Cells. *Blood J.* **81**, 2844–2853 (1993).

34. Pietras, E. M., Warr, M. R. & Passegué, E. Cell cycle regulation in hematopoietic stem cells. *J. Cell Biol.* **195**, 709–20 (2011).

35. Till, J. E. & McCulloch, E. A. A Direct Measurement of the Radiation Sensitivity of Normal Mouse Bone Marrow Cells. *Radiat. Res.* **14**, 213 (1961).

36. Szilvassy, S. J., Humphries, R. K., Lansdorp, P. M., Eaves, A. C. & Eaves, C. J. Quantitative assay for totipotent reconstituting hematopoietic stem cells by a competitive repopulation strategy. *Proc. Natl. Acad. Sci. U. S. A.* **87**, 8736–40 (1990).

37. Goodell, M. A., Brose, K., Paradis, G., Conner, A. S. & Mulligan, R. C. Isolation and functional properties of murine hematopoietic stem cells that are replicating in vivo. *J. Exp. Med.* **183**, 1797–806 (1996).

38. Spangrude, G. J., Heimfeld, S. & Weissman, I. L. Purification and characterization of mouse hematopoietic stem cells. *Science* **241**, 58–62 (1988).

39. Granick, J. L., Simon, S. I. & Borjesson, D. L. Hematopoietic Stem and Progenitor Cells as Effectors in Innate Immunity. *Bone Marrow Res.* **2012**, 1–8 (2012).

40. Ema, H., Morita, Y. & Suda, T. Heterogeneity and hierarchy of hematopoietic stem cells. *Exp. Hematol.* **42**, 74-82.e2 (2014).

41. Molawi, K. & Sieweke, M. H. Transcriptional Control of Macrophage Identity, Self-Renewal, and Function. *Adv. Immunol.* **120**, 269–300 (2013).

42. Epstein, R. S. *et al.* Patient Burden and Real-World Management of Chemotherapy-Induced Myelosuppression: Results from an Online Survey of Patients with Solid Tumors. *Adv. Ther.* **37**, 3606–3618 (2020).

43. Laurenti, E. & Göttgens, B. From haematopoietic stem cells to complex differentiation landscapes. *Nature* **553**, 418–426 (2018).

44. Chaddah, M. R., Wu, D. D. & Phillips, R. A. Variable self-renewal of reconstituting stem cells in long-term bone marrow cultures. *Exp. Hematol.* **24**, 497–508 (1996).

45. Park, B., Yoo, K. H. & Kim, C. Hematopoietic stem cell expansion and generation: the ways to make a breakthrough. *Blood Res.* **50**, 194–203 (2015).

46. Gvaramia, D. *et al.* Combined influence of biophysical and biochemical cues on maintenance and proliferation of hematopoietic stem cells. *Biomaterials* **138**, 108–117 (2017).

47. Crane, G. M., Jeffery, E. & Morrison, S. J. Adult haematopoietic stem cell niches. *Nat. Rev. Immunol.* **17**, 573–590 (2017).

48. Schofield, R. The relationship between the spleen colony-forming cell and the haemopoietic stem cell. *Blood Cells* **4**, 7–25 (1978).

49. Kiel, M. J. & Morrison, S. J. Maintaining Hematopoietic Stem Cells in the Vascular Niche. *Immunity* **25**, 862–864 (2006).

50. Suárez-Álvarez, B., López-Vázquez, A. & López-Larrea, C. Mobilization and Homing of Hematopoietic Stem Cells. *Adv Exp Med Biol* **741**, 152–170 (2012).

51. Zhang, C. C. & Lodish, H. F. Cytokines regulating hematopoietic stem cell

function. *Curr. Opin. Hematol.* **15**, 307–11 (2008).

52. Rödling, L. *et al.* 3D models of the hematopoietic stem cell niche under steady-state and active conditions. *Sci. Rep.* **7**, 4625 (2017).

53. Coskun, S. & Hirschi, K. K. Establishment and regulation of the HSC niche: Roles of osteoblastic and vascular compartments. *Birth Defects Res. C. Embryo Today* **90**, 229–42 (2010).

54. Morrison, S. J. & Scadden, D. T. The bone marrow niche for haematopoietic stem cells. *Nature* **505**, 327–34 (2014).

55. Klamer, S. & Voermans, C. The role of novel and known extracellular matrix and adhesion molecules in the homeostatic and regenerative bone marrow microenvironment. *Cell Adh. Migr.* **8**, 563–77 (2014).

56. Rodgers, K. D., San Antonio, J. D. & Jacenko, O. Heparan sulfate proteoglycans: A GAGgle of skeletal-hematopoietic regulators. *Dev. Dyn.* **237**, 2622–2642 (2008).

57. Yoshihara, H. *et al.* Thrombopoietin/MPL Signaling Regulates Hematopoietic Stem Cell Quiescence and Interaction with the Osteoblastic Niche. *Cell Stem Cell* **1**, 685–697 (2007).

58. Qian, H. *et al.* Critical Role of Thrombopoietin in Maintaining Adult Quiescent Hematopoietic Stem Cells. *Cell Stem Cell* **1**, 671–684 (2007).

59. Stier, S. *et al.* Osteopontin is a hematopoietic stem cell niche component that negatively regulates stem cell pool size. *J. Exp. Med.* **201**, 1781–1791 (2005).

60. Arai, F. *et al.* Tie2/Angiopoietin-1 Signaling Regulates Hematopoietic Stem Cell Quiescence in the Bone Marrow Niche. *Cell* **118**, 149–161 (2004).

61. Wang, L. D. & Wagers, A. J. Dynamic niches in the origination and differentiation of haematopoietic stem cells. *Nat. Rev. Mol. Cell Biol.* **12**, 643–55 (2011).

62. Gattazzo, F., Urciuolo, A. & Bonaldo, P. Extracellular matrix: a dynamic microenvironment for stem cell niche. *Biochim. Biophys. Acta* **1840**, 2506–19 (2014).

63. Tamma, R. & Ribatti, D. Bone Niches, Hematopoietic Stem Cells, and Vessel

Formation. *Int. J. Mol. Sci.* **18**, (2017).

64. Gurkan, U. A. & Akkus, O. The Mechanical Environment of Bone Marrow: A Review. *Ann. Biomed. Eng.* **36**, 1978–1991 (2008).

65. Metzger, T. A., Shudick, J. M., Seekell, R., Zhu, Y. & Niebur, G. L. Rheological behavior of fresh bone marrow and the effects of storage. *J. Mech. Behav. Biomed. Mater.* **40**, 307–313 (2014).

66. MacLean, A. L., Lo Celso, C. & Stumpf, M. P. H. Population dynamics of normal and leukaemia stem cells in the haematopoietic stem cell niche show distinct regimes where leukaemia will be controlled. *J. R. Soc. Interface* **10**, (2013).

67. Passaro, D. *et al.* Increased Vascular Permeability in the Bone Marrow Microenvironment Contributes to Disease Progression and Drug Response in Acute Myeloid Leukemia. *Cancer Cell* **32**, 324–341 (2017).

68. Sant, M. *et al.* Incidence of hematologic malignancies in Europe by morphologic subtype: Results of the HAEMACARE project. *Blood* **116**, 3724–3734 (2010).

69. Acute myeloid leukaemia - Causes - NHS. https://www.nhs.uk/conditions/acute-myeloid-leukaemia/causes/.

70. Cancer Research UK - Acute myeloid leukaemia (AML) statistics. https://www.cancerresearchuk.org/health-professional/cancer-statistics/statistics-by-cancer-type/leukaemia-aml (2020).

71. NHS - Acute myeloid leukaemia. https://www.nhs.uk/conditions/acute-myeloid-leukaemia/ (2020).

72. Almeida, A. M. & Ramos, F. Acute myeloid leukemia in the older adults. *Leuk. Res. Reports* **6**, 1–7 (2016).

73. Döhner, H., Weisdorf, D. J. & Bloomfield, C. D. Acute myeloid leukemia. *N. Engl. J. Med.* **373**, 1136–1152 (2015).

74. Risk Factors for Acute Myeloid Leukemia (AML). *American Cancer Society* https://www.cancer.org/cancer/acute-myeloid-leukemia/causes-risks-prevention/risk-factors.html (2018).

75. Shackleton, M., Quintana, E., Fearon, E. R. & Morrison, S. J. Heterogeneity

in Cancer: Cancer Stem Cells versus Clonal Evolution. *Cell* **138**, 822–829 (2009).

76. Wang, J. C. Y. & Dick, J. E. Cancer stem cells: lessons from leukemia. *Trends Cell Biol.* **15**, 494–501 (2005).

77. Greaves, M. Cancer stem cells: Back to Darwin? *Semin. Cancer Biol.* **20**, 65–70 (2010).

78. Huntly, B. J. P. & Gilliland, D. G. Leukaemia stem cells and the evolution of cancer-stem-cell research. *Nat. Rev. Cancer* **5**, 311–321 (2005).

79. Barabé, F., Kennedy, J. A., Hope, K. J. & Dick, J. E. Modeling the initiation and progression of human acute leukemia in mice. *Science (80-.).* **316**, 600–604 (2007).

80. Fearon, E. R., Burke, P. J., Schiffer, C. A., Zehnbauer, B. A. & Vogelstein, B. Differentiation of Leukemia Cells to Polymorphonuclear Leukocytes in Patients with Acute Nonlymphocytic Leukemia. *N. Engl. J. Med.* **315**, 15–24 (1986).

81. Lapidot, T. *et al.* A cell initiating human acute myeloid leukaemia after transplantation into SCID mice. *Nature* **367**, 645–648 (1994).

82. Bonnet, D. & Dick, J. E. Human acute myeloid leukemia is organized as a hierarchy that originates from a primitive hematopoietic cell. *Nat. Med.* **3**, 730–737 (1997).

83. Singh, S. K. *et al.* Identification of human brain tumour initiating cells. *Nature* **432**, 396–401 (2004).

84. O'Brien, C. A., Pollett, A., Gallinger, S. & Dick, J. E. A human colon cancer cell capable of initiating tumour growth in immunodeficient mice. *Nature* **445**, 106–110 (2007).

85. Al-Hajj, M., Wicha, M. S., Benito-Hernandez, A., Morrison, S. J. & Clarke, M. F. Prospective identification of tumorigenic breast cancer cells. *Proc. Natl. Acad. Sci.* **100**, 3983–3988 (2003).

86. Clarke, M. F. *et al.* Cancer stem cells - Perspectives on current status and future directions: AACR workshop on cancer stem cells. *Cancer Res.* **66**, 9339–9344 (2006).

87. Weissman, I. Stem Cell Research: paths to cancer therapies and regenerative medicine. *JAMA* **294**, 1359 (2005).

88. Reya, T., Morrison, S. J., Clarke, M. F. & Weissman, I. L. Stem cells, cancer, and cancer stem cells. *Nature* **414**, 105–111 (2001).

89. Lane, S. W. & Gilliland, D. G. Leukemia stem cells. *Semin. Cancer Biol.* **20**, 71–76 (2010).

90. Blume, R. *et al.* The molecular signature of AML with increased ALDH activity suggests a stem cell origin. *Leuk. Lymphoma* **59**, 2201–2210 (2018).

91. Chávez-González, A. *et al.* Expression of CD90, CD96, CD117, and CD123 on different hematopoietic cell populations from pediatric patients with acute myeloid leukemia. *Arch. Med. Res.* **45**, 343–350 (2014).

92. Hosen, N. *et al.* CD96 is a leukemic stem cell-specific marker in human acute myeloid leukemia. *Proc. Natl. Acad. Sci. U. S. A.* **104**, 11008–11013 (2007).

93. Lane, A. A. Targeting CD123 in AML. *Clin. Lymphoma, Myeloma Leuk.* **20**, S67–S68 (2020).

94. Almohsen, F. & Al-Mudallal, S. S. Impact of Leukemia Stem Cells Phenotype Expression on Response to Induction Therapy in Acute Myeloid Leukemia Patients. *Cardiovasc. Hematol. Disord. Targets* **20**, 145–151 (2019).

95. Riberdy, J. M. *et al.* The Art and Science of Selecting a CD123-Specific Chimeric Antigen Receptor for Clinical Testing. *Mol. Ther. - Methods Clin. Dev.* **18**, 571–581 (2020).

96. Hutmacher, C. *et al.* Development of a novel fully-human anti-CD123 antibody to target acute myeloid leukemia. *Leuk. Res.* **84**, 106178 (2019).

97. Villatoro, A., Konieczny, J., Cuminetti, V. & Arranz, L. Leukemia Stem Cell Release From the Stem Cell Niche to Treat Acute Myeloid Leukemia. *Front. Cell Dev. Biol.* **8**, (2020).

98. Kumar, B. *et al.* Acute myeloid leukemia transforms the bone marrow niche into a leukemia-permissive microenvironment through exosome secretion. *Leukemia* **32**, 575–587 (2018).

99. Duarte, D. *et al.* Inhibition of Endosteal Vascular Niche Remodeling Rescues Hematopoietic Stem Cell Loss in AML. *Cell Stem Cell* **22**, 64-77.e6 (2018).

100. Schepers, K., Campbell, T. B. & Passegué, E. Normal and leukemic stem cell niches: Insights and therapeutic opportunities. *Cell Stem Cell* **16**, 254–267 (2015).

101. Kokkaliaris, K. D. & Scadden, D. T. Cell interactions in the bone marrow microenvironment affecting myeloid malignancies. *Blood Adv.* **4**, 3795–3803 (2020).

102. Schepers, K., Campbell, T. B. & Passegué, E. Normal and leukemic stem cell niches: Insights and therapeutic opportunities. *Cell Stem Cell* vol. 16 254–267 (2015).

103. Walkley, C. R., Shea, J. M., Sims, N. A., Purton, L. E. & Orkin, S. H. Rb Regulates Interactions between Hematopoietic Stem Cells and Their Bone Marrow Microenvironment. *Cell* **129**, 1081–1095 (2007).

104. Walkley, C. R. *et al.* A Microenvironment-Induced Myeloproliferative Syndrome Caused by Retinoic Acid Receptor γ Deficiency. *Cell* **129**, 1097–1110 (2007).

105. Behrmann, L., Wellbrock, J. & Fiedler, W. Acute myeloid leukemia and the bone marrow niche - Take a closer look. *Front. Oncol.* **8**, 444 (2018).

106. Allan, D. S. & De Lisio, M. Reversing pathological remodelling of the bone marrow microenvironment in acute myeloid leukemia. *Stem Cell Investig.* **5**, (2018).

107. Ladikou, E. E., Sivaloganathan, H., Pepper, A. & Chevassut, T. Acute Myeloid Leukaemia in Its Niche: the Bone Marrow Microenvironment in Acute Myeloid Leukaemia. *Curr. Oncol. Rep.* **22**, 1–9 (2020).

108. Chen, Y. *et al.* Acute Myeloid Leukemia Induced Remodelling of the Human Bone Marrow Niche Predicts Clinical Outcome. *Blood* **132**, 3851–3851 (2018).

109. Yoshii, Y. *et al.* High-throughput screening with nanoimprinting 3D culture for efficient drug development by mimicking the tumor environment. *Biomaterials* **51**, 278–289 (2015).

110. Kenny, H. A. *et al.* Quantitative high throughput screening using a primary human three-dimensional organotypic culture predicts in vivo efficacy. *Nat.*

Commun. **6**, 1–11 (2015).

111. Shin, J. W. & Mooney, D. J. Extracellular matrix stiffness causes systematic variations in proliferation and chemosensitivity in myeloid leukemias. *Proc. Natl. Acad. Sci. U. S. A.* **113**, 12126–12131 (2016).

112. How chemotherapy is given Macmillan Cancer Support. https://www.macmillan.org.uk/cancer-information-and-support/treatment/types-of-treatment/chemotherapy/how-chemotherapy-is-given (2020).

113. UK, C. R. Chemotherapy for acute myeloid leukaemia (AML) | Acute myeloid leukaemia |. https://www.cancerresearchuk.org/about-cancer/acute-myeloid-leukaemia-aml/treating-aml/chemotherapy/chemotherapy-for-aml (2020).

114. Treatment Response Rates for Acute Myeloid Leukemia (AML). *American Cancer Society* https://www.cancer.org/cancer/acute-myeloid-leukemia/treating/response-rates.html (2020).

115. Koreth, J., Antin, J. H. & Cutler, C. Allogeneic Hematopoietic Stem Cell Transplantation for Acute Myeloid Leukemia and Myelodysplastic Syndrome in Adults. in *Hematology: Basic Principles and Practice* 970–980 (Elsevier Inc., 2018). doi:10.1016/B978-0-323-35762-3.00061-5.

116. Yu, J. *et al.* Advances in targeted therapy for acute myeloid leukemia. *Biomark. Res.* **8**, 1–11 (2020).

117. Wojcicki, A. V. *et al.* Repurposing drugs for acute myeloid leukemia: A worthy cause or a futile pursuit? *Cancers (Basel).* **12**, (2020).

118. Wong, C. H., Siah, K. W. & Lo, A. W. Estimation of clinical trial success rates and related parameters. *Biostatistics* **20**, 273–286 (2019).

119. Lai, C., Doucette, K. & Norsworthy, K. Recent drug approvals for acute myeloid leukemia. *J. Hematol. Oncol.* **12**, 100 (2019).

120. FDA. *Prescribing information for RYDAPT (midostaurin)*. www.fda.gov/medwatch. (2017).

121. Stone, R. M. *et al.* Midostaurin plus Chemotherapy for Acute Myeloid Leukemia with a *FLT3* Mutation. *N. Engl. J. Med.* **377**, 454–464 (2017).

122. FDA. *Prescribing information for XOSPATA (gilteritinib)*. www.fda.gov/medwatch. (2019).

123. Perl, A. E., Martinelli, G. & Cortes, J. E. Gilteritinib significantly prolongs overall survival in patients with FLT3-mutated (FLT3mut+) relapsed/refractory (R/R) acute myeloid leukemia (AML): Results from the Phase III ADMIRAL trial. in *American association for cancer research* (2019).

124. Stein, E. M. *et al.* Molecular remission and response patterns in patients with mutant-IDH2 acute myeloid leukemia treated with enasidenib. *Blood* **133**, 676–687 (2019).

125. Stein, E. M. *et al.* Enasidenib in mutant IDH2 relapsed or refractory acute myeloid leukemia. *Blood* **130**, 722–731 (2017).

126. FDA. *Prescribing information for IDHIFA (enasidenib)*. www.fda.gov/medwatch. (2017).

127. Norsworthy, K. J. *et al.* FDA approval summary: Ivosidenib for relapsed or refractory acute myeloid leukemia with an isocitrate dehydrogenase-1 mutation. *Clin. Cancer Res.* **25**, 3205–3209 (2019).

128. FDA. *Prescribing information of TIBSOVO (ivosidenib)*. www.fda.gov/medwatch. (2018).

129. DiNardo, C. D. *et al.* Venetoclax combined with decitabine or azacitidine in treatment-naive, elderly patients with acute myeloid leukemia. *Blood* **133**, 7–17 (2019).

130. FDA. *Prescribing information for VENCLEXTA (venetoclax)*. www.fda.gov/medwatch. (2019).

131. Lancet, J. E. *et al.* Cpx-351 (cytarabine and daunorubicin) liposome for injection versus conventional cytarabine plus daunorubicin in older patients with newly diagnosed secondary acute myeloid leukemia. *J. Clin. Oncol.* **36**, 2684–2692 (2018).

132. FDA. *Prescribing information for VYXEOS (daunorubicin and cytarabine liposome for injection)*. www.fda.gov/medwatch. (2017).

133. FDA. *Prescribing information for DAURISMO (glasdegib)*. www.fda.gov/medwatch. (2018).

134. Cortes, J. E. *et al.* Randomized comparison of low dose cytarabine with or without glasdegib in patients with newly diagnosed acute myeloid leukemia or high-risk myelodysplastic syndrome. *Leukemia* **33**, 379–389 (2019).

135. Jen, E. Y. *et al.* Fda approval: Gemtuzumab ozogamicin for the treatment of adults with newly diagnosed cd33-positive acute myeloid leukemia. *Clin. Cancer Res.* **24**, 3242–3246 (2018).

136. FDA. *Prescribing information for MYLOTARG (gemtuzumab ozogamicin for injection)*. www.fda.gov/medwatch. (2017).

137. Horby, P. *et al.* Dexamethasone in Hospitalized Patients with Covid-19 — Preliminary Report. *N. Engl. J. Med.* (2020) doi:10.1056/nejmoa2021436.

138. Ashburn, T. T. & Thor, K. B. Drug repositioning: Identifying and developing new uses for existing drugs. *Nat. Rev. Drug Discov.* **3**, 673–683 (2004).

139. Pushpakom, S. *et al.* Drug repurposing: Progress, challenges and recommendations. *Nat. Rev. Drug Discov.* **18**, 41–58 (2018).

140. Zhang, Z. *et al.* Overcoming cancer therapeutic bottleneck by drug repurposing. *Signal Transduct. Target. Ther.* **5**, 1–25 (2020).

141. Ramsey, J. M. *et al.* Entinostat Prevents Leukemia Maintenance in a Collaborating Oncogene-Dependent Model of Cytogenetically Normal Acute Myeloid Leukemia. *Stem Cells* **31**, 1434–1445 (2013).

142. Roulston, G. D. R. *et al.* Low-dose salinomycin induces anti-leukemic responses in AML and MLL. *Oncotarget* **7**, 73448–73461 (2016).

143. Gupta, P. B. *et al.* Identification of Selective Inhibitors of Cancer Stem Cells by High-Throughput Screening. *Cell* **138**, 645–659 (2009).

144. Naujokat, C. & Steinhart, R. Salinomycin as a drug for targeting human cancer stem cells. *J. Biomed. Biotechnol.* **2012**, 17 (2012).

145. Mai, T. T. *et al.* Salinomycin kills cancer stem cells by sequestering iron in lysosomes. *Nat. Chem.* **9**, 1025–1033 (2017).

146. Asano, T. *et al.* Distinct Mechanisms of Ferritin Delivery to Lysosomes in Iron-Depleted and Iron-Replete Cells. *Mol. Cell. Biol.* **31**, 2040–2052 (2011).

147. Recalcati, S., Gammella, E. & Cairo, G. Dysregulation of iron metabolism in cancer stem cells. *Free Radic. Biol. Med.* **133**, 216–220 (2019).

148. Herrlinger, K. R. R. *et al.* Efficacy, safety and tolerability of vidofludimus in patients with inflammatory bowel disease: The ENTRANCE study. *J. Crohn's Colitis* **7**, 636–643 (2013).

149. Muehler, A., Kohlhof, H., Groeppel, M. & Vitt, D. The Selective Oral Immunomodulator Vidofludimus in Patients with Active Rheumatoid Arthritis: Safety Results from the COMPONENT Study. *Drugs R D* **19**, 351–366 (2019).

150. Cao, L. *et al.* Targeting of hematologic malignancies with PTC299, a novel potent inhibitor of dihydroorotate dehydrogenase with favorable pharmaceutical properties. *Mol. Cancer Ther.* **18**, 3–16 (2019).

151. Sykes, D. B. The emergence of dihydroorotate dehydrogenase (DHODH) as a therapeutic target in acute myeloid leukemia. *Expert Opin. Ther. Targets* **22**, 893–898 (2018).

152. Wu, D. *et al.* Pharmacological inhibition of dihydroorotate dehydrogenase induces apoptosis and differentiation in acute myeloid leukemia cells. *Haematologica* **103**, 1472–1483 (2018).

153. Jackevicius, C. A. *et al.* Comparative effectiveness of generic atorvastatin and lipitor® in patients hospitalized with an acute coronary syndrome. *J. Am. Heart Assoc.* **5**, (2016).

154. Hassanabad, A. F. Current perspectives on statins as potential anti-cancer therapeutics: Clinical outcomes and underlying molecular mechanisms. *Transl. Lung Cancer Res.* **8**, 692–699 (2019).

155. Zhang, L. *et al.* Atorvastatin Exerts Antileukemia Activity via Inhibiting Mevalonate-YAP Axis in K562 and HL60 Cells. *Front. Oncol.* **9**, 1032 (2019).

156. University of Kansas Medical Center. A Pilot Trial of Atorvastatin in Tumor Protein 53 (p53) -Mutant and p53 Wild-Type Malignancies. https://clinicaltrials.gov/ct2/show/NCT03560882?term=atorvastatin&cond=Acute+Myeloid+Leukemia&draw=2&rank=2 (2018).

157. Mahoney, C. E. *et al.* A chemical biology screen identifies a vulnerability of neuroendocrine cancer cells to SQLE inhibition. *Nat. Commun.* **10**, 1–14 (2019).

158. Longo, J., van Leeuwen, J. E., Elbaz, M., Branchard, E. & Penn, L. Z. Statins as Anticancer Agents in the Era of Precision Medicine. *Clin. Cancer Res.* **26**, 5791–5800 (2020).

159. Pickl, M. & Ries, C. H. Comparison of 3D and 2D tumor models reveals enhanced HER2 activation in 3D associated with an increased response to trastuzumab. *Oncogene* **28**, 461–468 (2009).

160. Imamura, Y. *et al.* Comparison of 2D- and 3D-culture models as drug-testing platforms in breast cancer. *Oncol. Rep.* **33**, 1837–1843 (2015).

161. Fischbach, C. *et al.* Engineering tumors with 3D scaffolds. *Nat. Methods* **4**, 855–860 (2007).

162. Hoarau-Véchot, J., Rafii, A., Touboul, C. & Pasquier, J. Halfway between 2D and animal models: Are 3D cultures the ideal tool to study cancer-microenvironment interactions? *Int. J. Mol. Sci.* **19**, (2018).

163. Kapałczyńska, M. *et al.* 2D and 3D cell cultures – a comparison of different types of cancer cell cultures. *Arch. Med. Sci.* **14**, 910–919 (2018).

164. Walasek, M. A., van Os, R. & de Haan, G. Hematopoietic stem cell expansion: challenges and opportunities. *Ann. N. Y. Acad. Sci.* **1266**, 138–150 (2012).

165. Bai, T. *et al.* Expansion of primitive human hematopoietic stem cells by culture in a zwitterionic hydrogel. *Nat. Med.* **25**, 1566–1575 (2019).

166. Cuchiara, M. L. *et al.* Bioactive poly(ethylene glycol) hydrogels to recapitulate the HSC niche and facilitate HSC expansion in culture. *Biotechnol. Bioeng.* **113**, 870–881 (2016).

167. Griessinger, E. & Andreeff, M. NSG-S mice for acute myeloid leukemia, yes. For myelodysplastic syndrome, no. *Haematologica* **103**, 921–923 (2018).

168. Mupo, A. *et al.* A powerful molecular synergy between mutant Nucleophosmin and Flt3-ITD drives acute myeloid leukemia in mice. *Leukemia* **27**, 1917–1920 (2013).

169. Almosailleakh, M. & Schwaller, J. Murine models of acute Myeloid Leukaemia. *International Journal of Molecular Sciences* vol. 20 (2019).

170. Abarrategi, A. *et al.* Modeling the human bone marrow niche in mice: From host bone marrow engraftment to bioengineering approaches. *Journal of*

Experimental Medicine vol. 215 729–743 (2018).

171. Majeti, R. Monoclonal antibody therapy directed against human acute myeloid leukemia stem cells. *Oncogene* vol. 30 1009–1019 (2011).

172. Gerber, J. M. *et al.* A clinically relevant population of leukemic CD34 -CD38 - cells in acute myeloid leukemia. *Blood* **119**, 3571–3577 (2012).

173. Xing, D. *et al.* Perspectives on Animal Models Utilized for the Research and Development of Regenerative Therapies for Articular Cartilage. *Curr. Mol. Biol. Reports* **2**, 90–100 (2016).

174. Khalil, A. S., Jaenisch, R. & Mooney, D. J. Engineered tissues and strategies to overcome challenges in drug development. *Adv. Drug Deliv. Rev.* **158**, 116–139 (2020).

175. Lee-Thedieck, C. & Spatz, J. P. Artificial Niches: Biomimetic Materials for Hematopoietic Stem Cell Culture. *Macromol. Rapid Commun.* **33**, 1432–1438 (2012).

176. Lutolf, M. P., Gilbert, P. M. & Blau, H. M. Designing materials to direct stem-cell fate. *Nature* **462**, 433–441 (2009).

177. Clara-Trujillo, S., Ferrer, G. G. & Ribelles, J. L. G. In vitro modeling of non-solid tumors: How far can tissue engineering go? *Int. J. Mol. Sci.* **21**, 1–31 (2020).

178. Legant, W. R. *et al.* Measurement of mechanical tractions exerted by cells in three-dimensional matrices. *Nat. Methods* **7**, 969–71 (2010).

179. El-Sherbiny, I. M. & Yacoub, M. H. Hydrogel scaffolds for tissue engineering: Progress and challenges. *Glob. Cardiol. Sci. Pract.* **2013**, 316–42 (2013).

180. Bray, L. J. *et al.* A three-dimensional ex vivo tri-culture model mimics cell-cell interactions between acute myeloid leukemia and the vascular niche. *Haematologica* **102**, 1215–1226 (2017).

181. Blanco, T. M., Mantalaris, A., Bismarck, A. & Panoskaltsis, N. The development of a three-dimensional scaffold for ex vivo biomimicry of human acute myeloid leukaemia. *Biomaterials* **31**, 2243–2251 (2010).

182. Li, D. *et al.* A novel extracellular matrix-based leukemia model supports leukemia cells with stem cell-like characteristics. *Leuk. Res.* **72**, 105–112

(2018).

183. Aljitawi, O. S. *et al.* A novel three-dimensional stromal-based model for in vitro chemotherapy sensitivity testing of leukemia cells. *Leuk. Lymphoma* **55**, 378–391 (2014).

184. Harada, T., Tsuboi, I., Utsunomiya, M., Yasuda, M. & Aizawa, S. Kinetics of leukemic cells in 3D culture with stromal cells and with arginine deprivation stress. *J. Biosci. Bioeng.* **130**, 650–658 (2020).

185. Harada, T. *et al.* Kinetics of hematopoietic stem cells and supportive activities of stromal cells in a three-dimensional bone marrow culture system. *Growth Factors* **33**, 347–355 (2015).

186. Choi, J. S. & Harley, B. A. C. Marrow-inspired matrix cues rapidly affect early fate decisions of hematopoietic stem and progenitor cells. *Sci. Adv.* **3**, (2017).

187. Houshmand, M. *et al.* Mimicking the Acute Myeloid Leukemia Niche for Molecular Study and Drug Screening. *Tissue Eng. - Part C Methods* **23**, 72–85 (2017).

188. Zhou, H. S., Carter, B. Z. & Andreeff, M. Bone marrow niche-mediated survival of leukemia stem cells in acute myeloid leukemia: Yin and Yang. *Cancer Biol. Med.* **13**, 248–259 (2016).

189. Kitaeva, K. V., Rutland, C. S., Rizvanov, A. A. & Solovyeva, V. V. Cell Culture Based in vitro Test Systems for Anticancer Drug Screening. *Front. Bioeng. Biotechnol.* **8**, 322 (2020).

190. Kamoun, E. A., Kenawy, E.-R. S. & Chen, X. A review on polymeric hydrogel membranes for wound dressing applications: PVA-based hydrogel dressings. *J. Adv. Res.* **8**, 217–233 (2017).

191. Hubbell, J. A. Synthetic biodegradable polymers for tissue engineering and drug delivery. *Curr. Opin. Solid State Mater. Sci.* **3**, 246–251 (1998).

192. Hoffman, A. S. Hydrogels for Biomedical Applications. *Ann. N. Y. Acad. Sci.* **944**, 62–73 (2006).

193. Sokol, E. S. *et al.* Growth of human breast tissues from patient cells in 3D hydrogel scaffolds. *Breast Cancer Res.* **18**, 19 (2016).

194. Aurand, E. R., Lampe, K. J. & Bjugstad, K. B. Defining and designing polymers and hydrogels for neural tissue engineering. *Neurosci. Res.* **72**, 199–213 (2012).

195. Hansen, K. C. *et al.* An in-solution ultrasonication-assisted digestion method for improved extracellular matrix proteome coverage. *Mol. Cell. Proteomics* **8**, 1648–1657 (2009).

196. Orkin, R. W. *et al.* A murine tumor producing a matrix of basement membrane. *J. Exp. Med.* **145**, 204–220 (1977).

197. Kleinman, H. K. & Martin, G. R. Matrigel: Basement membrane matrix with biological activity. *Semin. Cancer Biol.* **15**, 378–386 (2005).

198. Mujeeb, A. Self-assembled octapeptide gels for cartilage repair. *[Thesis]. Manchester, UK: The University of Manchester; 2013.* (The University of Manchester, Manchester, UK, 2013).

199. Koutsopoulos, S. Self-assembling peptide nanofiber hydrogels in tissue engineering and regenerative medicine: Progress, design guidelines, and applications. *J. Biomed. Mater. Res. Part A* **104**, 1002–1016 (2016).

200. Bradshaw, M. *et al.* Designer self-assembling hydrogel scaffolds can impact skin cell proliferation and migration. *Sci. Rep.* **4**, 6903 (2015).

201. Ashkin, A. Acceleration and Trapping of Particles by Radiation Pressure. *Phys. Rev. Lett.* **24**, 156–159 (1970).

202. Ashkin, A. Optical trapping and manipulation of neutral particles using lasers. *Proc. Natl. Acad. Sci. U. S. A.* **94**, 4853–4860 (1997).

203. Ashkin, A. The Pressure of Laser Light. *Sci. Am. Inc.* **226**, 62–71 (1972).

204. Zhang, H. & Liu, K.-K. Optical tweezers for single cells. *J. R. Soc. Interface* **5**, 671–90 (2008).

205. Wang, M. M. *et al.* Microfluidic sorting of mammalian cells by optical force switching. *Nat. Biotechnol.* **23**, 83–87 (2005).

206. Allemand, J.-F., Bensimon, D. & Croquette, V. Stretching DNA and RNA to probe their interactions with proteins. *Curr. Opin. Struct. Biol.* **13**, 266–274 (2003).

207. Jagannathan, B. & Marqusee, S. Protein folding and unfolding under force.

Biopolymers **99**, 860–9 (2013).

208. Huisstede, J. H. G., Subramaniam, V. & Bennink, M. L. Combining optical tweezers and scanning probe microscopy to study DNA–protein interactions. *Microsc. Res. Tech.* **70**, 26–33 (2007).

209. Johansen, P. L., Fenaroli, F., Evensen, L., Griffiths, G. & Koster, G. Optical micromanipulation of nanoparticles and cells inside living zebrafish. *Nat. Commun.* **7**, 10974 (2016).

210. Li, Q., Rycaj, K., Chen, X. & Tang, D. G. Cancer stem cells and cell size: A causal link? *Semin. Cancer Biol.* **35**, 191–199 (2015).

211. Diez-Silva, M., Dao, M., Han, J., Lim, C.-T. & Suresh, S. Shape and Biomechanical Characteristics of Human Red Blood Cells in Health and Disease. *MRS Bull.* **35**, 382–388 (2010).

212. Molloy, J. E. & Padgett, M. J. Lights, action: optical tweezers. *Contemp. Phys.* **43**, 241–258 (2002).

213. Huff, A., Melton, C. N., Hirst, L. S. & Sharping, J. E. Stability and instability for low refractive-index-contrast particle trapping in a dual-beam optical trap. *Biomed. Opt. Express* **6**, 3812–9 (2015).

214. Yao, A., Tassieri, M., Padgett, M. & Cooper, J. Microrheology with optical tweezers. *Lab Chip* **9**, 2568–2575 (2009).

215. Tassieri, M. Microrheology with optical tweezers: peaks & troughs. *Curr. Opin. Colloid Interface Sci.* **43**, 39–51 (2019).

216. Tassieri, M., Evans, M. L., Warren, R. L., Bailey, N. J. & Cooper, J. M. Microrheology with optical tweezers: data analysis. *New J. Phys.* **14**, 115032 (2012).

217. Watts, F. *et al.* Investigating the micro-rheology of the vitreous humor using an optically trapped local probe. *J. Opt. J. Opt* **16**, 15301–15308 (2014).

218. Ciccone, G. *et al.* What Caging Force Cells Feel in 3D Hydrogels: A Rheological Perspective. *Adv. Healthc. Mater.* **9**, (2020).

219. Peterman, E. J. G. G., Gittes, F. & Schmidt, C. F. Laser-Induced Heating in Optical Traps. *Biophys. J.* **84**, 1308–1316 (2003).

220. Martin Chaplin. Water absorption spectrum.

http://www1.lsbu.ac.uk/water/water_vibrational_spectrum.html#d (2020).

221. Liu, Y. *et al.* Evidence for Localized Cell Heating Induced by Infrared Optical Tweezers. *Biophys. J.* **68**, 2137–2144 (1995).

222. Hoffmann, A. *et al.* Optical tweezers for confocal microscopy. *Appl. Phys. B* **71**, 747–753 (2000).

223. Kotlarchyk, M. A., Botvinick, E. L. & Putnam, A. J. Characterization of hydrogel microstructure using laser tweezers particle tracking and confocal reflection imaging. *J. Phys. Condens. Matter* **22**, 121–194 (2010).

224. Gou, X. *et al.* Cell adhesion manipulation through single cell assembly for characterization of initial cell-to-cell interaction. *Biomed. Eng. Online* **14**, 114 (2015).

225. Peled, A. *et al.* The chemokine SDF-1 activates the integrins LFA-1, VLA-4, and VLA-5 on immature human CD34(+) cells: role in transendothelial/stromal migration and engraftment of NOD/SCID mice. *Blood* **95**, 3289–96 (2000).

226. Hu, S., Gou, X., Han, H., Leung, A. Y. H. & Sun, D. Manipulating cell adhesions with optical tweezers for study of cell-to-cell interactions. *J. Biomed. Nanotechnol.* **9**, 281–5 (2013).

227. Zhu, R., Avsievich, T., Popov, A. & Meglinski, I. Optical Tweezers in Studies of Red Blood Cells. *Cells* **9**, 545 (2020).

228. Choudhary, D., Mossa, A., Jadhav, M. & Cecconi, C. Bio-molecular applications of recent developments in optical tweezers. *Biomolecules* **9**, (2019).

229. Zhou, M., Haifeng, Y., Jianke, D. & Enlan, Z. Manipulation on human red blood cells with femtosecond optical tweezers. *Chinese Opt. Lett.* **6**, 919–921 (2008).

230. Mao, F. L. *et al.* Optical trapping of red blood cells and two-photon excitation-based photodynamic study using a femtosecond laser. *Opt. Commun.* **256**, 358–363 (2005).

231. Ashworth, J. C. C. *et al.* Peptide gels of fully-defined composition and

mechanics for probing cell-cell and cell-matrix interactions in vitro. *Matrix Biol.* **85**–**86**, 15–33 (2019).

232. Bosshart, H. & Heinzelmann, M. THP-1 cells as a model for human monocytes. *Ann. Transl. Med.* **4**, 438 (2016).

233. Chanput, W., Peters, V. & Wichers, H. THP-1 and U937 cells. in *The Impact of Food Bioactives on Health: In Vitro and Ex Vivo Models* 147–159 (Springer International Publishing, 2015). doi:10.1007/978-3-319-16104-4_14.

234. Tsuchiya, S. *et al.* Establishment and characterization of a human acute monocytic leukemia cell line (THP-1). *Int. J. Cancer* **26**, 171–176 (1980).

235. Odero, M. D., Zeleznik-Le, N. J., Chinwalla, V. & Rowley, J. D. Cytogenetic and molecular analysis of the acute monocytic leukemia cell line THP-1 with an MLL-AF9 translocation. *Genes, Chromosom. Cancer* **29**, 333–338 (2000).

236. THP-1 ATCC® TIB-202™. *ATCC* https://www.lgcstandards-atcc.org/products/all/TIB-202.aspx?geo_country=gb (2020).

237. Jensen, H. A., Yourish, H. B., Bunaciu, R. P., Varner, J. D. & Yen, A. Induced myelomonocytic differentiation in leukemia cells is accompanied by noncanonical transcription factor expression. *FEBS Open Bio* **5**, 789–800 (2015).

238. U-937 ATCC ® CRL-1593.2™ Homo sapiens Pleura/pleural effusio. *ATCC* https://www.lgcstandards-atcc.org/products/all/CRL-1593.2.aspx?geo_country=gb (2020).

239. Santoli, D. *et al.* Synergistic and antagonistic effects of recombinant human interleukin (IL) 3, IL-1 alpha, granulocyte and macrophage colony-stimulating factors (G-CSF and M-CSF) on the growth of GM-CSF-dependent leukemic cell lines. *J. Immunol.* **139**, 3348–54 (1987).

240. MV-4-11 ATCC ® CRL-9591™ Homo sapiens peripheral blood biph. *ATCC* https://www.lgcstandards-atcc.org/Products/All/CRL-9591.aspx?geo_country=gb (2020).

241. HL-60 ATCC ® CCL-240™ Homo sapiens peripheral blood acute p. *ATCC* https://www.lgcstandards-atcc.org/products/all/CCL-240.aspx?geo_country=gb (2020).

242. Fleck, R. A., Romero-Steiner, S. & Nahm, M. H. Use of HL-60 cell line to measure opsonic capacity of pneumococcal antibodies. *Clin. Diagn. Lab. Immunol.* **12**, 19–27 (2005).

243. OCI-AML3 (ACC 582). *DSMZ, Leibniz Institute* https://www.dsmz.de/collection/catalogue/details/culture/ACC-582 (2020).

244. STEMdiff™ Hematopoietic Kit | STEMCELL Technologies. https://www.stemcell.com/stemdiff-hematopoietic-kit.html (2020).

245. Merry, C. *et al.* Method of making a hydrogel. (2013).

246. Schindelin, J. *et al.* Fiji: An open-source platform for biological-image analysis. *Nat. Methods* **9**, 676–682 (2012).

247. Fedus, K. & Boudebs, G. Experimental techniques using 4f coherent imaging system for measuring nonlinear refraction. *Opt. Commun.* **292**, 140–148 (2013).

248. Goodman, J. W. *Introduction to Fourier Optics*. (Roberts & Co. Publishers, 2005).

249. Nikon. Nikon | Healthcare Products & Solutions (Microscope Solutions) | CFI Plan Apochromat Lambda Series. https://www.nikon.com/products/microscope-solutions/lineup/objectives/cfi_plan_apochromat_lambda/index.htm (2020).

250. Bowman, R. W. *et al.* Adaptive optics in an optical trapping system for enhanced lateral trap stiffness at depth. *J. Opt* **15**, 75305–75313 (2013).

251. Tassieri, M. *et al.* Microrheology with optical tweezers: Measuring the relative viscosity of solutions 'at a glance'. *Sci. Rep.* **5**, 1–6 (2015).

252. Zia, R. N. Active and Passive Microrheology: Theory and Simulation. *Annu. Rev. Fluid Mech* **50**, 371–405 (2018).

253. Del Giudice, F., Tassieri, M., Oelschlaeger, C. & Shen, A. Q. When Microrheology, Bulk Rheology, and Microfluidics Meet: Broadband Rheology of Hydroxyethyl Cellulose Water Solutions. *Macromolecules* **50**, 2951–2963 (2017).

254. Mason, T. G. & Weitz, D. A. Optical measurements of frequency-dependent linear viscoelastic moduli of complex fluids. *Phys. Rev. Lett.* **74**, 1250–1253 (1995).

255. Bennett, J. S. *et al.* Spatially-resolved rotational microrheology with an optically-trapped sphere. *Sci. Rep.* **3**, 1–5 (2013).

256. Mansel, B. W. *et al.* A Practical Review of Microrheological Techniques. *Rheol. - New Concepts, Appl. Methods* (2013) doi:10.5772/53639.

257. Berg-Sørensen, K. & Flyvbjerg, H. Power spectrum analysis for optical tweezers. *Rev. Sci. Instrum.* **75**, (2004).

258. Van Der Horst, A. & Forde, N. R. Power spectral analysis for optical trap stiffness calibration from high-speed camera position detection with limited bandwidth. *Opt. Trapp. Appl.* **16**, 3 (2008).

259. Chu, K. K. *et al.* Particle-Tracking Microrheology Using Micro-Optical Coherence Tomography. *Biophys. J.* **111**, 1053–1063 (2016).

260. Michalet, X. Mean square displacement analysis of single-particle trajectories with localization error: Brownian motion in an isotropic medium. *Phys. Rev. E - Stat. Nonlinear, Soft Matter Phys.* **82**, 041914 (2010).

261. Czerwinski, F., Richardson, A. C. & Oddershede, L. B. Quantifying Noise in Optical Tweezers by Allan Variance. *Opt. Express* **17**, 13255 (2009).

262. Lee, M. P., Gibson, G. M., Phillips, D., Padgett, M. J. & Tassieri, M. Dynamic stereo microscopy for studying particle sedimentation. *Opt. Express* **22**, 4671 (2014).

263. Korson, L. *et al.* Viscosity of Water at Various Temperatures. *J. Phys. Chem.* **1**, 34–39 (1969).

264. Wu, J. *et al.* Measurement of the membrane elasticity of red blood cell with osmotic pressure by optical tweezers. *Cryo-Letters* **30**, 89–95 (2009).

265. Belloni, F., Monneret, S., Monduc, F. & Scordia, M. Multiple holographic optical tweezers parallel calibration with optical potential well characterization. *Opt. Express* **16**, 9011 (2008).

266. Sarshar, M., Wong, W. T. & Anvari, B. Comparative study of methods to calibrate the stiffness of a single-beam gradient-force optical tweezers over

various laser trapping powers. *J. Biomed. Opt.* **19**, 115001 (2014).

267. Gao, J. *et al.* Controlling Self-Assembling Peptide Hydrogel Properties through Network Topology. *Biomacromolecules* **18**, 826–834 (2017).

268. Issman, L. & Talmon, Y. Cryo-SEM specimen preparation under controlled temperature and concentration conditions. *J. Microsc.* **246**, 60–69 (2012).

269. Marmorat, C. *et al.* Cryo-Imaging of Hydrogels Supermolecular Structure. *Sci. Rep.* **6**, 1–6 (2016).

270. Newcomb, C. J., Moyer, T. J., Lee, S. S. & Stupp, S. I. Advances in cryogenic transmission electron microscopy for the characterization of dynamic self-assembling nanostructures. *Curr. Opin. Colloid Interface Sci.* **17**, 350–359 (2012).

271. Akselrod, G. M. *et al.* Laser-guided assembly of heterotypic three-dimensional living cell microarrays. *Biophys. J.* **91**, 3465–3473 (2006).

272. McAlinden, N., Glass, D. G., Millington, O. & Wright, A. J. Viability studies of optically trapped T-cells. *Opt. Trapp. Opt. Micromanipulation VIII* **8097**, (2011).

273. Promega. CellTiter-Glo® Luminescent Cell Viability Assay. https://www.promega.co.uk/products/cell-health-assays/cell-viability-and-cytotoxicity-assays/celltiter_glo-luminescent-cell-viability-assay/?catNum=G7570 (2020).

274. Li, Z. In Vitro Micro-Tissue and -Organ Models for Toxicity Testing. *Compr. Biotechnol. Second Ed.* **5**, 551–563 (2011).

275. Duellman, S. J. *et al.* Bioluminescent, Nonlytic, Real-Time Cell Viability Assay and Use in Inhibitor Screening. *Assay Drug Dev. Technol.* **13**, 456–465 (2015).

276. Kijanska, M. & Kelm, J. In vitro 3D Spheroids and Microtissues: ATP-based Cell Viability and Toxicity Assays. *Assay Guid. Man.* (2004).

277. Idrees, A. *et al.* Validation of in vitro assays in threedimensional human dermal constructs. *Int. J. Artif. Organs* **41**, 779–788 (2018).

278. Kaufman, D. S., Hanson, E. T., Lewis, R. L., Auerbach, R. & Thomson, J. A. Hematopoietic colony-forming cells derived from human embryonic stem

cells. *Proc. Natl. Acad. Sci. U. S. A.* **98**, 10716–10721 (2001).

279. Panciera, T., Azzolin, L., Cordenonsi, M. & Piccolo, S. Mechanobiology of YAP and TAZ in physiology and disease. *Nat. Rev. Mol. Cell Biol.* **18**, 758–770 (2017).

280. Sun, M., Spill, F. & Zaman, M. H. A Computational Model of YAP/TAZ Mechanosensing. *Biophys. J.* **110**, 2540–2550 (2016).

281. Dupont, S. *et al.* Role of YAP/TAZ in mechanotransduction. *Nature* **474**, 179–184 (2011).

282. Zonderland, J. & Moroni, L. Steering cell behavior through mechanobiology in 3D: a regenerative medicine perspective. *Biomaterials* **268**, (2020).

283. Chen, X. D., Dusevich, V., Feng, J. Q., Manolagas, S. C. & Jilka, R. L. Extracellular matrix made by bone marrow cells facilitates expansion of marrow-derived mesenchymal progenitor cells and prevents their differentiation into osteoblasts. *J. Bone Miner. Res.* **22**, 1943–1956 (2007).

284. Malara, A. *et al.* Megakaryocytes contribute to the bone marrow-matrix environment by expressing fibronectin, type IV collagen, and laminin. *Stem Cells* **32**, 926–937 (2014).

285. Bendall, L. J. *et al.* Stem cell factor enhances the adhesion of AML cells to fibronectin and augments fibronectin-mediated anti-apoptotic and proliferative signals. *Leukemia* **12**, 1375–1382 (1998).

286. An, Y. *et al.* Selection of a novel DNA aptamer against OFA/iLRP for targeted delivery of doxorubicin to AML cells. *Sci. Rep.* **9**, (2019).

287. Jha, A. K., Xu, X., Duncan, R. L. & Jia, X. Controlling the adhesion and differentiation of mesenchymal stem cells using hyaluronic acid-based, doubly crosslinked networks. *Biomaterials* **32**, 2466–2478 (2011).

288. Goncharova, V. *et al.* Hyaluronan expressed by the hematopoietic microenvironment is required for bone marrow hematopoiesis. *J. Biol. Chem.* **287**, 25419–25433 (2012).

289. Azadniv, M. *et al.* Bone marrow mesenchymal stromal cells from acute myelogenous leukemia patients demonstrate adipogenic differentiation propensity with implications for leukemia cell support. *Leukemia* **34**, 391–

403 (2020).

290. Yip, D. & Cho, C. H. A multicellular 3D heterospheroid model of liver tumor and stromal cells in collagen gel for anti-cancer drug testing. *Biochem. Biophys. Res. Commun.* **433**, 327–332 (2013).

291. Song, H. H. G., Park, K. M. & Gerecht, S. Hydrogels to model 3D in vitro microenvironment of tumor vascularization. *Adv. Drug Deliv. Rev.* **79**, 19–29 (2014).

292. Infanger, D. W., Lynch, M. E. & Fischbach, C. Engineered Culture Models for Studies of Tumor-Microenvironment Interactions. *Annu. Rev. Biomed. Eng.* **15**, 29–53 (2013).

293. Gill, B. J. & West, J. L. Modeling the tumor extracellular matrix: Tissue engineering tools repurposed towards new frontiers in cancer biology. *J. Biomech.* **47**, 1969–1978 (2014).

294. Hérault, A. *et al.* Myeloid progenitor cluster formation drives emergency and leukaemic myelopoiesis. *Nature* **544**, 53–58 (2017).

295. PepCalc.com - Peptide calculator. https://pepcalc.com/ (2015).

296. Dias, S. *et al.* Autocrine stimulation of VEGFR-2 activates human leukemic cell growth and migration. *J. Clin. Invest.* **106**, 511–521 (2000).

297. Wong, J. F., Simmons, C. A. & Young, E. W. K. Modeling and Measurement of Biomolecular Transport and Sensing in Microfluidic Cell Culture and Analysis Systems. in *Modeling of Microscale Transport in Biological Processes* 41–75 (Elsevier Inc., 2017). doi:10.1016/B978-0-12-804595-4.00003-1.

298. Monteiro, M. V., Gaspar, V. M., Ferreira, L. P. & Mano, J. F. Hydrogel 3D: In vitro tumor models for screening cell aggregation mediated drug response. *Biomater. Sci.* **8**, 1855–1864 (2020).

299. Nourse, J. L. & Pathak, M. M. How cells channel their stress: Interplay between Piezo1 and the cytoskeleton. *Seminars in Cell and Developmental Biology* vol. 71 3–12 (2017).

300. Cooper, J. & Giancotti, F. G. Integrin Signaling in Cancer: Mechanotransduction, Stemness, Epithelial Plasticity, and Therapeutic

Resistance. *Cancer Cell* vol. 35 347–367 (2019).

301. Kräter, M. *et al.* Bone marrow niche-mimetics modulate HSPC function via integrin signaling. *Sci. Rep.* **7**, 1–15 (2017).
302. Arcangeli, A., Pillozzi, S. & Becchetti, A. Targeting Ion Channels in Leukemias: A New Challenge for Treatment. *Curr. Med. Chem.* **19**, 683–696 (2012).
303. Horton, P. D., Dumbali, S. & Wenzel, P. L. Mechanoregulation in Hematopoiesis and Hematologic Disorders. *Current Stem Cell Reports* vol. 6 86–95 (2020).
304. Li, Y. & Kumacheva, E. Hydrogel microenvironments for cancer spheroid growth and drug screening. *Sci. Adv.* **4**, (2018).
305. Clark, A. M. *et al.* A microphysiological system model of therapy for liver micrometastases. *Exp. Biol. Med.* **239**, 1170–1179 (2014).
306. Gu, L. & Mooney, D. J. Biomaterials and emerging anticancer therapeutics: Engineering the microenvironment. *Nat. Rev. Cancer* **16**, 56–66 (2016).
307. Jansen, K. A., Atherton, P. & Ballestrem, C. Mechanotransduction at the cell-matrix interface. *Seminars in Cell and Developmental Biology* vol. 71 75–83 (2017).
308. Han, Y. L. *et al.* Cell swelling, softening and invasion in a three-dimensional breast cancer model. *Nat. Phys.* **16**, 101–108 (2020).
309. Raudenska, M. *et al.* Cisplatin enhances cell stiffness and decreases invasiveness rate in prostate cancer cells by actin accumulation. *Sci. Rep.* **9**, (2019).
310. Hu, L. *et al.* Decreased cell stiffness enhances leukemia development and progression. *Leukemia* **34**, 2493–2497 (2020).
311. Lam, W. A., Rosenbluth, M. J. & Fletcher, D. A. Chemotherapy exposure increases leukemia cell stiffness. *Blood* **109**, 3505–3508 (2007).
312. Soligo, G., Roccon, A. & Soldati, A. Deformation of clean and surfactant-laden droplets in shear flow. *Meccanica* **55**, 371–386 (2020).
313. Adjei, I. & Blanka, S. Modulation of the Tumor Microenvironment for Cancer Treatment: A Biomaterials Approach. *J. Funct. Biomater.* **6**, 81–103 (2015).

314. Kim, J., Koo, B. K. & Knoblich, J. A. Human organoids: model systems for human biology and medicine. *Nature Reviews Molecular Cell Biology* vol. 21 571–584 (2020).

315. Alzeeb, G., Metges, J. P., Corcos, L. & Le Jossic-Corcos, C. Three-dimensional culture systems in gastric cancer research. *Cancers* vol. 12 1–20 (2020).

316. Pearl, R. VII. On certain points concerning the probable error of the standard deviation. *Biometrika* **6**, 112–116 (1908).

Chapter 8: Appendix

8.1. ICC of U937 cells in peptide gels

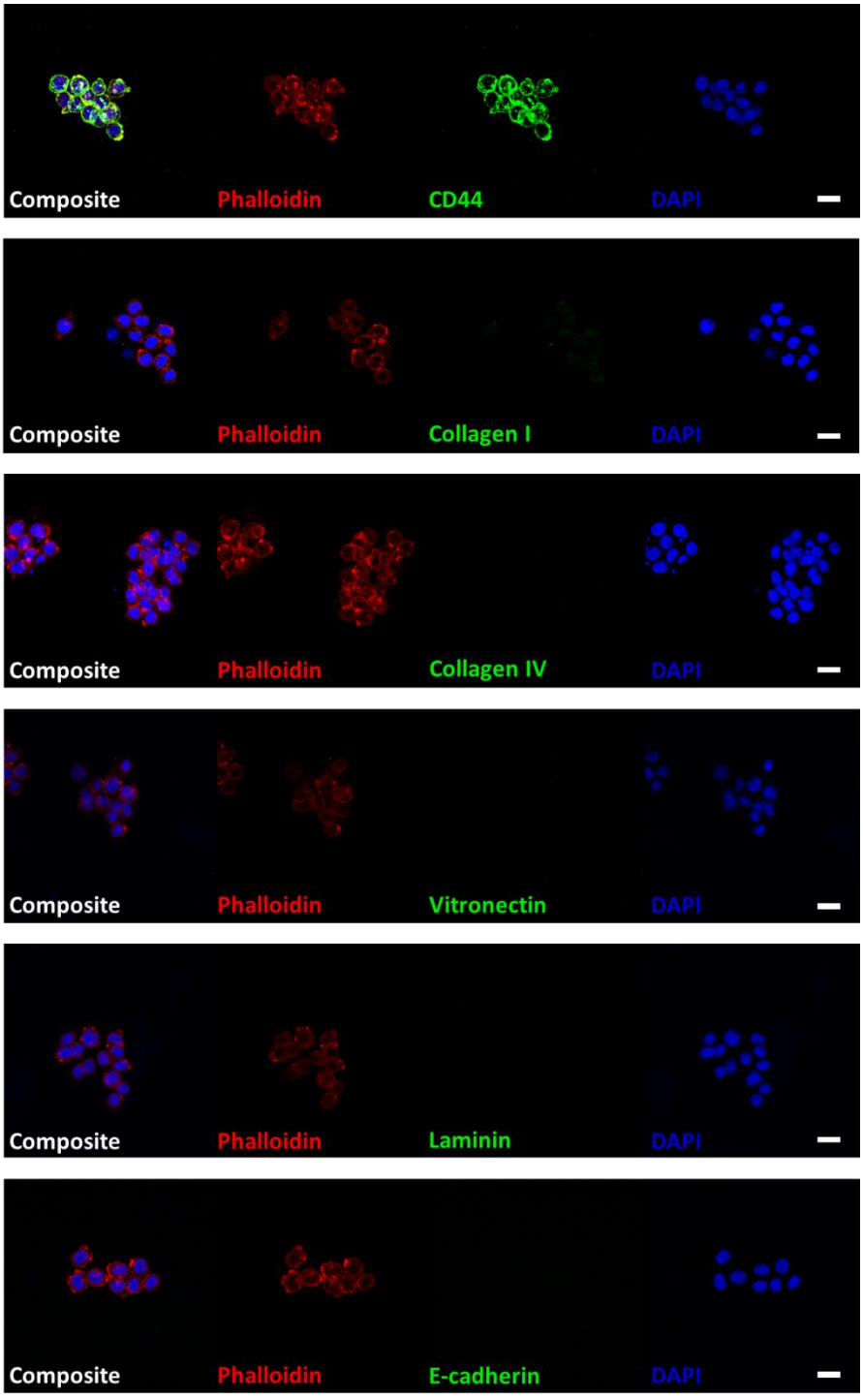


Figure 8.1: Fluorescence images of U937 cells in 6 mg/mL peptide gels*. Cells were cultured for 72 h prior to staining for matrix proteins. Scale bars = 20 μm.*